General Disclaimer

One or more of the Following Statements may affect this Document

- This document has been reproduced from the best copy furnished by the organizational source. It is being released in the interest of making available as much information as possible.

- This document may contain data, which exceeds the sheet parameters. It was furnished in this condition by the organizational source and is the best copy available.

- This document may contain tone-on-tone or color graphs, charts and/or pictures, which have been reproduced in black and white.

- This document is paginated as submitted by the original source.

- Portions of this document are not fully legible due to the historical nature of some of the material. However, it is the best reproduction available from the original submission.

by

Donald C. D. Chang

May 1978

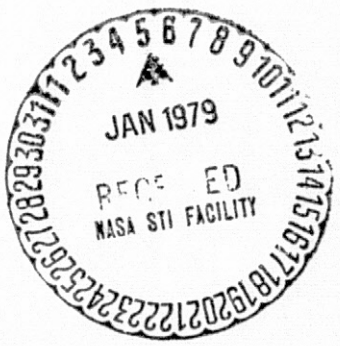

Technical Report No. 3458-1

Prepared under

Division of Polar Programs of the National Science Foundation
Grant NSF-DPP76-82646
Atmospheric Sciences Section of the National Science Foundation
Grant NSF-ATM75-07707
National Aeronautics and Space Administration
Grant NGL-05-020-008

SEL-78-017

VLF WAVE-WAVE INTERACTION EXPERIMENTS IN THE MAGNETOSPHERE

by

Donald C. D. Chang

May 1978

Technical Report No. 3458-1

Prepared under

Division of Polar Programs of
the National Science Foundation
Grant NSF-DPP76-82646
Atmospheric Sciences Section of
the National Science Foundation
Grant NSF-ATM75-07707
National Aeronautics and Space Administration
Grant NGL-05-020-008

Radioscience Laboratory
Stanford Electronics Laboratories
Stanford University Stanford, California

ABSTRACT

VLF wave-wave interaction experiments have been carried out by injecting various forms of VLF pulses into the magnetosphere from a 21.2 Km dipole antenna at Siple, Antarctica. The data are collected at the Siple conjugate, near Roberval, Quebec. The injected signals propagate along a geomagnetic field line and often interact strongly with energetic electrons trapped in the radiation belts near the equator. Signals may be amplified and trigger emissions. These signals may then interact with one another through these energetic electrons. Suppression of signal growth and energy coupling among the signals are commonly observed.

This report is divided into three parts. In the first part, simulations of VLF pulses propagating in the magnetosphere are carried out. The results show that the leading edge of a VLF pulse is distorted sufficiently when it arrives at the interaction region to alter the details of the wave-particle interaction process in the magnetosphere. It is also found that the calculated group delay at the carrier frequency agrees closely with the travel time of the center of a VLF pulse. The center is defined as the center of the interval within which the signal exceeds 30 percent of the peak value. In addition, a digital equalizer is designed to compensate for the distortions developed in a VLF pulse that propagates through the magnetosphere. Computer simulations show that this device can completely compensate for the distortions.

In the second part, it is found for the first time that a 10 ms gap in a triggering wave can induce emission, which may then interact with the post-gap signals. Suppression and entrainment between the

gap-induced emissions and the post-gap signals are often observed. The phenomenon of gap-induced emission is explained by the hypothesis that an emission can develop within 10 msec at the end of a triggering wave. Experimental data show that, as the gap is opened up in time, we can "scan" the development of emissions. One of the results confirms an earlier observation that emissions always start with a small rise in frequency. It is also found that a 70 ms gap in a trigger wave is long enough to allow falling emission fully developed. During these studies, a new feature of wave-wave interaction was observed. The post-gap signals can "capture" a falling emission that is 90 Hz below the transmitter signals, causing the emission to overshoot toward the positive frequency side. The frequency difference between these two signals appears to be an important factor in determining whether or not the interaction can occur.

In the third part, sideband triggering is reported for the first time. Sidebands are generated by frequency-shift-key (FSK) modulation techniques. Sidebands generated by short modulation periods can trigger emissions, indicating that the average electron "memory" time in the magnetosphere is at least as long as twice the modulation period. The corresponding length of the electron interaction region is estimated to lie between 2000 and 4000 km. Furthermore, it is found that two sidebands with a frequency difference of 50 Hz or less mutually interact. The interaction is attributed to the overlap of the two $V_{\parallel}$ ranges in which the electrons can be organized by the corresponding sidebands. It is believed that the $V_{\parallel}$ range is related to the wave intensity in the interaction region. Using a homogeneous model, we have found the wave intensity in the interaction region to be $2.5 \sim 10$ mγ, in reasonable agreement with satellite measurements.

ACKNOWLEDGMENTS

I would like to thank Professor R. A. Helliwell for his guidance of this research. Professor Helliwell has impressed me with his professional integrity and his constructive criticism of new ideas. His insight and comments have improved both the scientific content and the literary style of this report.

I owe a great deal to Dr. T. F. Bell for revising the manuscript and his suggestions and comments at various stages of the work. I am grateful to Professors D. L. Carpenter and J. K. Katsufrakis and Dr. C. G. Park for many suggestions and comments. Most of the data presented here are related to the transmitter at Siple Station, Antarctica. My sincere thanks go to the various people who went to Siple Station. I am grateful to Mr. J. W. Yarbrough for making all the spectrograms in this report. Informal discussions with my colleagues in the Radioscience Laboratory, Stanford University, especially Mr. E. C. Ha with whom I have shared the same office for three years, have contributed significantly to this work.

I would like to thank Professor M. Chodorow for his careful reading of this work. I want to thank all persons involved in the final preparation of this manuscript, in particular, Inga Lof, for her excellent typing.

I am grateful to my parents for their moral support and to my wife, Bi-Hua, for her patience and encouragement throughout the course of this work.

This research was supported in part by the Division of Polar Programs of the National Science Foundation, in part by the Atmospheric Science Section of the National Science Foundation, and in part by the National Aeronautics and Space Administration.

CONTENTS

CONTENTS (Cont)

ILLUSTRATIONS

ILLUSTRATIONS (Cont)

TABLES

Chapter I

INTRODUCTION

This study is concerned with VLF wave-wave interaction (WWI) in the magnetosphere. In this chapter, we give a brief introduction on this topic and outline the contributions of the present work.

A. Magnetosphere

The magnetosphere is created by the interaction between the solar wind and the geomagnetic fields. The solar wind is a plasma consisting mainly of electrons and protons. The solar wind flow is supersonic. At the earth, the solar wind encounters the earth's magnetic field. The result is the bow-shock wave sunward of the planet, where the solar wind is decelerated and deflected. The solar wind drags the geomagnetic field toward the midnight direction. The magnetotail is formed. Most of the solar wind flows past the earth's protective magnetic field, but some leaks through, filling parts of the magnetic cavity with hot plasma. This magnetic cavity, distorted by solar wind flow and filled with tenuous plasma of varying temperatures, is the magnetosphere [e.g., Chapman, 1977]. A sketch of the magnetosphere is shown in Fig. 1.1.

The region of our interest is the so-called "plasmasphere" that, roughly speaking, corotates with the earth. The plasmasphere is populated by cold plasma, mainly electrons and protons in the energy range of a few electron volts or less. The equatorial density could be as high as 10^2 to 10^3 electrons per cm^3. This equatorial density drops by one to two orders of magnitude within 0.5 earth radii (R_E) or less at the boundary between the outer magnetosphere and the plasmasphere

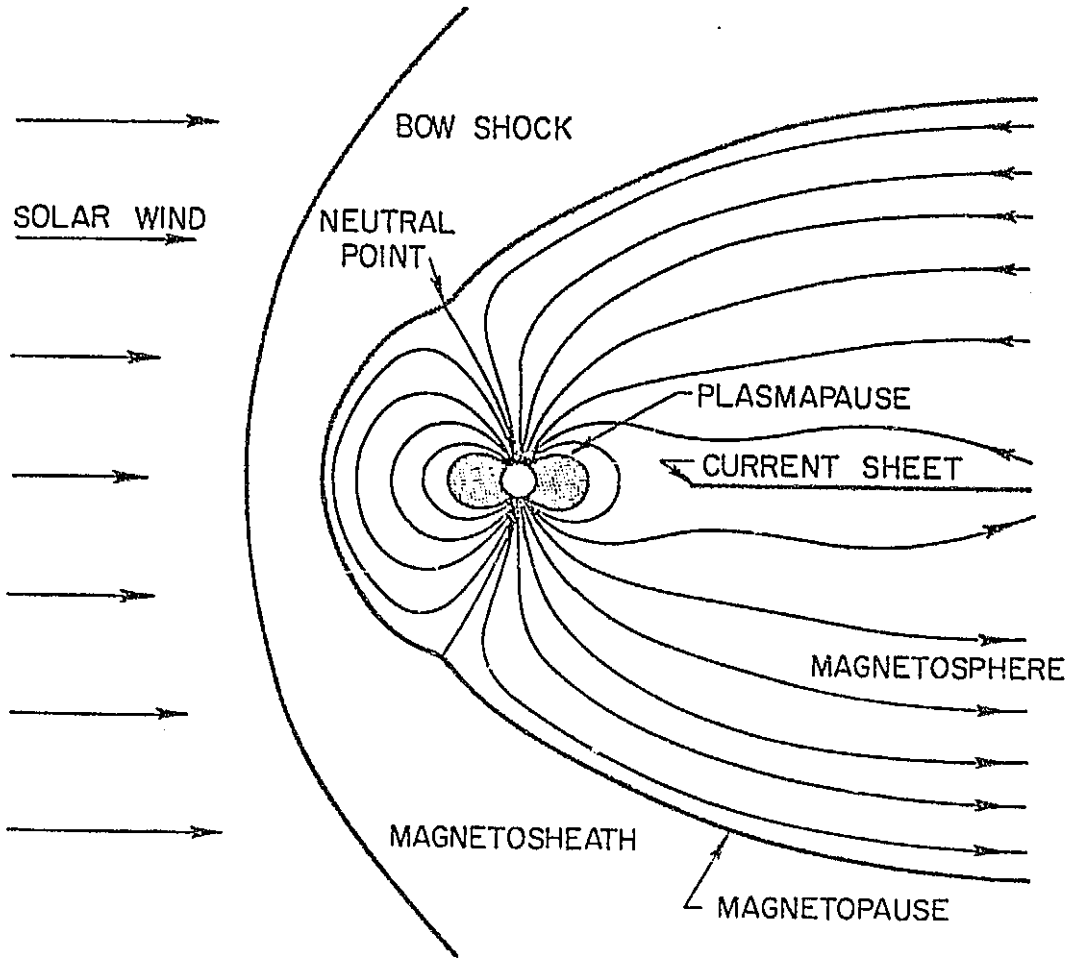

Fig. 1.1. A SKETCH OF THE NOON-MIDNIGHT MERIDIAN SECTION OF A MODEL MAGNETOSPHERE SHOWING THE PLASMASPHERE (SHADED AREA INSIDE THE PLASMAPAUSE) IN RELATION TO OTHER MAGNETOSPHERE FEATURES. (Taken from Ho [1974])

[Carpenter, 1962, 1966]. The boundary, discovered by Carpenter [1962, 1963], is called plasmapause. The location of the plasmapause varies from $2R_E$ after the onset of a major substorm to as much as $7R_E$ after a long quiet period. The plasmapause is generally near $\sim 4R_E$ under moderately disturbed conditions [e.g., Carpenter, 1966].

The cold plasma in the plasmasphere is created mainly by the sun. Photons from the sun produce ionization in the F-region of the ionosphere in the dayside sector. This cold plasma from the ionosphere can diffuse upward along the geomagnetic field lines into the plasmasphere surrounding the earth. At night, the cold plasma "stored" in the plasmasphere flows downward into the ionosphere to maintain the night time F-region [Park, 1970].

Superimposed upon the cold plasma is a tenuous high energy component with energy in the keV or higher range. Most of these high energy particles are trapped in the plasmasphere for reasonably long periods. The electron density of the energetic component can be as low as a few tenths of an electron per cm^3. An electron moving among the magnetospheric protons is practically collisionless [e.g., Ratcliffe, 1972] and moves in a helical path around a geomagnetic field line and bounces back and forth between two mirror points; one in the northern hemisphere and the other in the southern hemisphere. Except for gyrating in the opposite sense and taking a longer period than electrons, a proton also forms a helical path along a geomagnetic field line and bounces back and forth between its mirror points. Superimposed upon the helical motion is a slow longitudinal drift around the earth, eastward for electrons and westward for protons. The oppositely directed drifts of protons and electrons constitute a ring current around the earth, flowing westward [e.g., Roederer, 1970].

How does this high energy plasma get into the magnetosphere? How do the particles diffuse within the magnetosphere? What are the leakage mechanisms of these particles? All of these questions have not been yet completely answered. One possibility may begin with solar wind particles leaking across the magnetopause, which separates the magnetosphere from the outer space, into a boundary layer called the plasma mantle that sheaths the magnetosphere just inside the boundary. These particles are accelerated along the open magnetic field lines and enter the plasmasphere from the polar cusp. Once arriving at the plasmasphere, these particles may move to other field lines through cross-L diffusion [e.g., Hess, 1968]. The cross-L diffusion may come from convective E-field or asymmetrical distortions of geomagnetic field by, say, solar storm. The loss mechanism is believed to be pitch angle diffusion either due to cyclotron resonance or due to bounce motion resonance with external excitations [Robert, 1969; Tverskoy, 1969]. For further information on these topics, the reader is referred to Hess [1968], Roberts [1969], Roederer [1970], Akasofu and Chapman [1972].

B. Whistler-Mode Signals and Cyclotron Resonance

Whistler-mode (WM) is one of the modes of propagation of electromagnetic waves in a plasma in the presence of a static magnetic field and is characterized by the following:

(1) propagation along magnetic field

(2) sense of rotation of wave field the same as electrons

(3) wave frequency less than gyro-frequency and electron plasma frequency

In the magnetosphere, WM waves are, roughly speaking, in the kHz range. (We shall use the term "VLF signal" to represent WM signals in the magnetosphere hereafter.) In this report, we limit ourselves to the ducted WM signals only. Most of the ducted WM waves travel along field-aligned enhancements in the magnetosphere. This confines the wave normal to small angles from the static magnetic field. Ducts for WM waves in the magnetosphere, like optical fiber glass, can guide the signals from one hemisphere to the other. The signals are then able to penetrate the lower ionosphere and reach the ground.

One of the interesting properties of WM waves is their low group velocity. WM waves also propagate with low phase velocity. A typical value of the group velocity near the equator at $\sim 4R_E$ in the magnetosphere is about one-tenth of the speed of light.

Since WM waves and electrons gyrate in the same sense, electrons may experience constant wave fields for reasonably long periods when the doppler-shifted frequencies of the waves seen by the electrons equal the local gyrofrequency. This is the cyclotron resonance condition. For WM cyclotron resonance, the waves and the electrons must travel in opposite directions. In the magnetosphere, the electrons that can interact with the VLF waves are mainly in the keV range. For constant frequency signal, the most effective interaction region is thought to be around the equator, where inhomogeneity of the geomagnetic fields is a minimum.

C. Background of the Experiments

Many types of magnetospheric amplifications and emissions are believed to result from cyclotron interaction between WM waves and energetic

electrons trapped in the radiation belts. In the VLF wave injection experiments that we shall discuss in this report, VLF pulses are injected into the magnetosphere from a 21.2 km dipole antenna at Siple, Antarctica. The signals propagate along an enhancement duct and reach the equatorial region, where they effectively interact with high energy electrons streaming from the opposite direction. As a result of this interaction, the signals are amplified and trigger emissions which are the "new" signals at frequencies other than the parent signals. The amplified signals and triggered emissions then travel along the remainder of the duct and arrive at the conjugate point of Siple near Roberval, Quebec. The geometry of the wave injection experiments is illustrated in Fig. 1.2.

The spectrogram in Fig. 1.3 shows an example of wave amplification and emission triggering. The vertical and horizontal axes show the frequency and time scales, respectively. The blackness indicates the wave intensity. A two-second pulse at 3 kHz is injected into the magnetosphere from Siple. The arrival time of the pulse at Roberval is at $t = 0$. The pulse duration is indicated by the time scale. It is observed that the signal is amplified and triggers two rising emissions; one at about 0.5 sec and the other at the end of the triggering wave.

In addition to producing wave amplification and triggering emissions, these experiments show a variety of interesting and important effects. For example, the emissions may dump electrons into the ionosphere [Inan, 1977; Dingle, 1978]. The precipitated electrons may excite X-ray [e.g., Rosenburg et al, 1971], may perturb electron density sufficiently to affect subionospheric VLF propagation [Helliwell et al, 1973], and may modulate the local conductivity so as to cause the excitation of ULF waves [Bell, 1976]. It is important, therefore, to understand the mechanisms that govern growth of VLF waves and the generation of emissions.

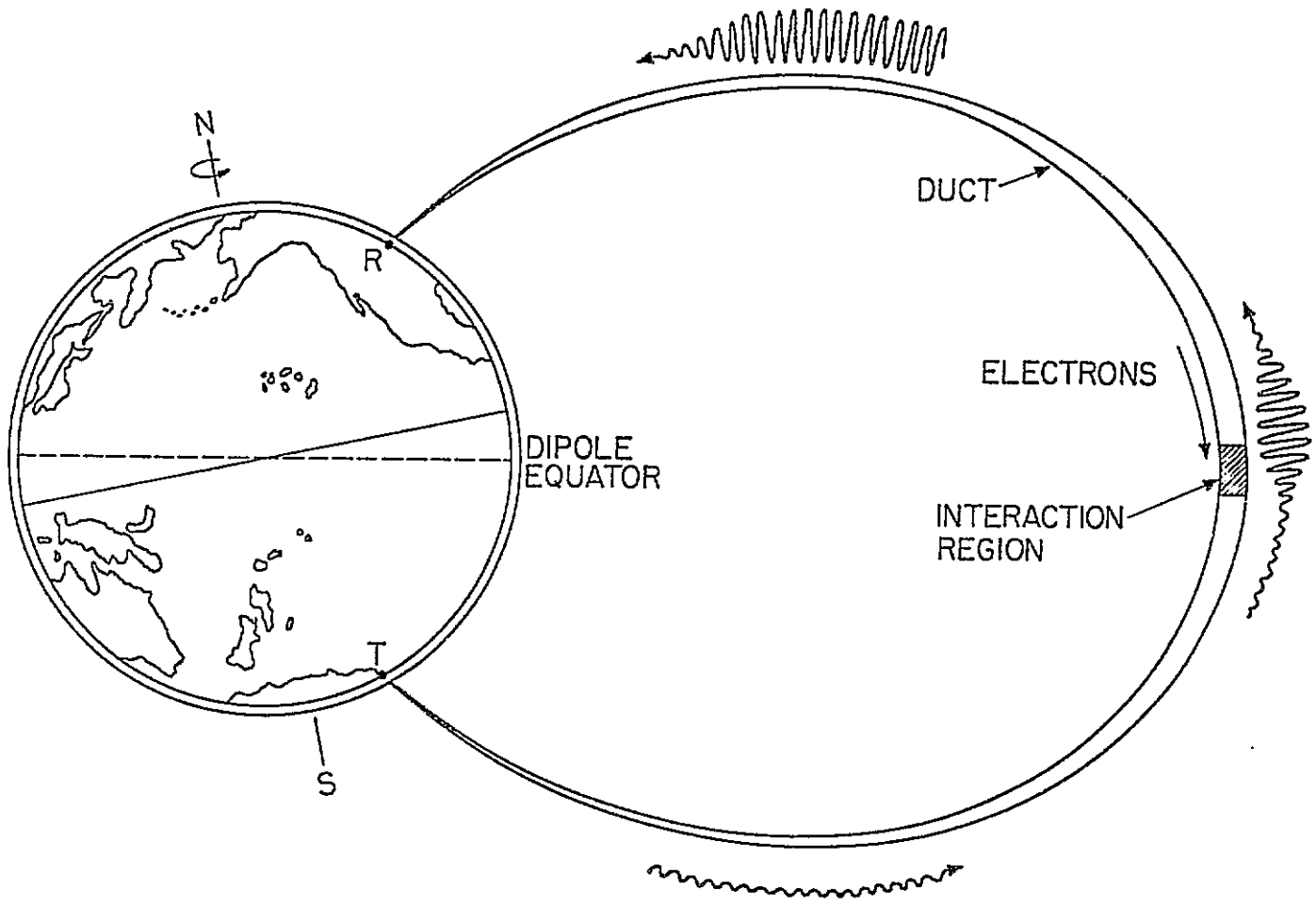

Fig. 1.2. A SKETCH SHOWING PROPAGATION OF TRANSMITTER SIGNALS BETWEEN SIPLE STATION AND ROBERVAL. Signals injected from Siple travel along a field-aligned duct of enhanced ionization. The signals interact with high energy electrons traveling in the opposite direction in an interaction region near the equator. (Taken from Raghuram [1977])

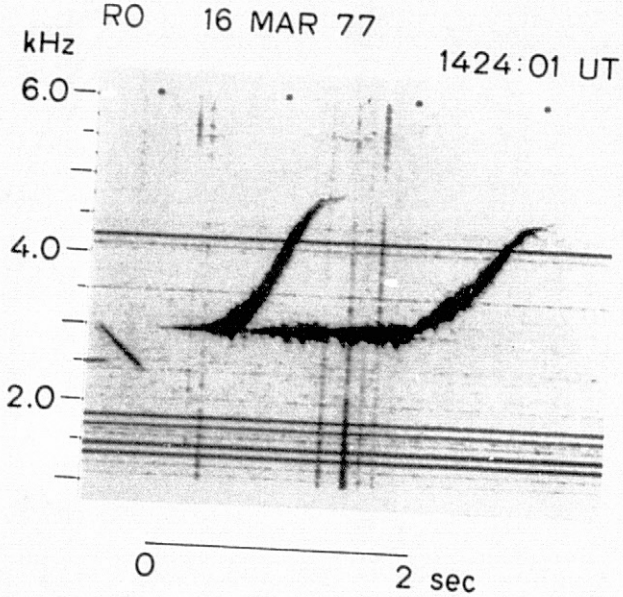

Fig. 1.3. TYPICAL EXAMPLES OF WM WAVE AMPLIFICATIONS AND TRIGGERING EMISSIONS.

There are a number of theories used in explaining wave amplification and triggering phenomena [e.g., Brice, 1964; Bell and Buneman, 1964; Helliwell, 1967; Liemohn, 1967; Dysthe, 1971; Palmadesso and Schmidt, 1971; Matsumoto, 1972; Brinca, 1972; Helliwell and Crystal, 1973; Nunn, 1974; Newman, 1977].

In one class of the theories, phase-bunched current is employed [e.g., Helliwell and Crystal, 1973]. A constant frequency signal can interact with electrons which are nearly in resonance with it. As a result of this interaction, the "phases" of the electrons are organized by the wave. Net transverse currents are produced and they radiate a new field. Thus, some of the kinetic energy of electrons is transferred to the wave, and the wave may appear as being amplified. This process of organizing electrons in phases is called the phase-bunching process. The characteristic time required for the exchange of energy between the wave and the electrons is called the bunching time.

Many VLF wave injection experiments have been designed to study the phase-bunching process in the magnetosphere. Two such experiments have led us to the discovery of two new phenomena: gap-induced emission and sideband triggering. The gap-induced emissions and post-gap transmitter signals often interact. The former can suppress the growth of the latter, and the latter may also suppress the development of the former. This category of wave-wave interaction (WWI), involving emissions as well as amplified injected signals, is one of the WWI's that will be discussed in this report. Another kind of WWI that will be discussed is the mutual interaction among sidebands at various frequencies. Sidebands are generated by injecting frequency-shift-key (FSK) signals into the magnetosphere. Sideband interactions occur when the frequency spacings between

the sidebands are small. We shall also briefly describe this kind of WWI in the next section. These two kinds of WWI mentioned above are the principle topics of this report.

Many types of VLF wave-wave interactions have been reported. Among them are suppression and entrainment of emissions by man-made signals [Helliwell and Katsufrakis, 1974], interactions between whistlers and quasi-periodic emissions [Ho, 1974], interactions between emissions and power-line-harmonics radiated by the North-America power system leaking into the magnetosphere [Helliwell et al, 1975], echo suppression of the growth of transmitter signals [Raghuram et al, 1977a], and suppression of hiss by man-made signals [Raghuram et al, 1977b]. Recently, Helliwell [1978] has summarized various types of interactions between emissions and man-made signals and proposed a phenomenological theory to explain these interactions.

D. Outline of the Thesis

This report deals with three subjects: VLF pulse propagation in the magnetosphere, gap-induced emission, and sideband triggering.

In Chapter II, we shall discuss pulse propagation in the magnetosphere, a highly dispersive medium. VLF pulses traveling through such a medium may suffer distortion before arriving at the wave-particle interaction region. This distortion may alter the details of VLF wave-particle interaction. Experiments for the studies of wave-particle and wave-wave interaction in the magnetosphere are carried out by injecting VLF pulses into the magnetosphere. Knowledge of how the pulses are altered due to propagation distortion developed between the transmitter

site and the interaction region is essential in the interpretation of the results of these wave injection experiments.

In Chapter III, the phenomenon of gap-induced emissions will be presented. It was discovered in one such experiment in which a 10-msec gap was inserted in a one-second pulse to alter the "phase" of the signal. At the time the program was designed, it was believed that a 10-ms gap was too short to affect the wave-particle interaction processes and that the main effects should come from the phase alterations. It was the first program designed to study the details of phase-bunching mechanisms.

It turns out that the phase alterations are immaterial to the growth of the post-gap signals. Furthermore, it is discovered that a 10-ms gap in a triggering wave can induce emissions. The gap-induced emissions may then interact with the post-gap signals. Suppressions and entrainments between those signals are often observed. This is one "type" of wave-wave interaction (WWI) in the magnetosphere we shall discuss in this report. This WWI, involving an amplified transmitter signal and an emission, will be called a forced-mode/natural-mode wave-wave interaction (FNWWI). An emission is said to be in a natural mode because it is not driven by external signals. Once it has been triggered, it is on its own. Amplified transmitter signals are in a forced (or driven) mode because they are driven by external signals. "Forced mode" and "natural mode" adapted in here are defined by considering the wave-particle interaction process in the magnetosphere as a whole to be a single system. They are not defined from the point of view of a single electron motion in the interaction region, which is adapted by Helliwell [1978].

In Chapter IV, we shall study a phenomenon called sideband triggering. It was discovered unexpectedly during a wave injection experiment in which the phase of a one-second signal was alternated regularly to investigate the details of the phase-bunching processes in the magnetosphere. Because of the regular modulation of the phase of a signal, sidebands are generated. We find that some of the sidebands, just like isolated constant frequency signals, can trigger emissions.

The frequency spacings between the sidebands are controllable by changing the modulation periods. It is found that, when the frequency spacing is small, suppression or coupling between sidebands is often observed. The mutual interactions among sidebands belong to the category of sideband mutual interactions (SMI).

E. Contributions of the Present Work

1. Pulse Propagation in the Magnetosphere

We have, for the first time, calculated the distortion of a VLF pulse (of finite duration) that propagates through the magnetosphere. Among the results are the following:

(1) It is found that the group velocity evaluated at the carrier frequency predicts the arrival time of a VLF pulse better when the time delay refers to the "center" and not to the leading edge of the pulse.

(2) It is found that the frequency of a distorted pulse is not constant over the duration of the pulse. The largest deviations occur at the front and/or the rear ends of the pulse.

(3) It is found that the frequency at which a VLF pulse suffers a minimum distortion at the equator is the "nose" frequency which is defined as the frequency at which the signal has the minimum time delay [e.g., Helliwell, 1965].

(4) It is found that a discontinuity in the phase of a sinusoidal wave introduced on the ground develops into an amplitude gap when the signal arrives at the equator. The gap can be as large as 20 msec for the signal at 3 kHz propagating along a duct at $L = 4$.

(5) A digital equalizer has been designed to compensate the phase distortion developed in the magnetosphere. This device can be used as a pre- as well as a post-processor. Computer simulations show that the distortion can be completely compensated by this device.

2. Gap-Induced Emissions

(1) Gap-induced emissions are reported for the first time. A 10-ms gap in a VLF wave can induce emissions, suggesting that emissions start to develop within a time period shorter than 10 msec at the end of the VLF pulse.

(2) The phenomenon of gap-induced emissions is explained by the hypothesis that emissions (natural mode) can begin at the end of the triggering signal.

(3) A transmitter program has been designed to test some of the ideas developed from the studies of gap-induced emission. One of the results confirms an earlier observation that falling emissions always start with a small rise in frequency. It is also found that a 70-msec gap is long enough to allow falling emissions to become fully developed.

(4) A new feature of the WWI has been discovered. The post-gap signal can "capture" a falling emission whose frequency lies 90 Hz below that of the post-gap signal. The falling emission turns around in frequency and overshoots toward the positive frequency direction.

(5) The frequency difference between a gap-induced emission and the post-gap signal appears to be an important factor in determining whether or not they can mutually interact.

3. Sideband Triggering

(1) Sideband amplification and triggering are reported for the first time.

(2) It has been found that the energetic electrons in the magnetosphere only resolve the sidebands generated by signals with short modulation periods. Based on this discovery, we have found a way to estimate the length of the electron interaction region. Our results show that it lies between 2000 and 4000 km.

(3) It is found that sidebands with less than 50 Hz spacings mutually interact. Suppression and energy coupling among the sidebands are often observed. More extensive wave injection experiments, which will be described in detail in Chapter IV, reveal that 50 Hz is the order of magnitude of the critical frequency range within which sidebands interact.

(4) Mutual interaction between two sidebands is explained by the overlaps of $V_{\parallel}$ ranges of electrons which the sidebands can organize. The electrons in the overlap can exchange energy with both sidebands and are responsible for the interaction. Therefore, 50 Hz appears to be a reasonable value for the corresponding frequency range

of the size of the $V_{\parallel}$ range within which electrons can be effectively organized by a sideband.

(5) The sideband intensity in the interaction region is estimated to be on the order of 2.5 ~ 10 mγ according to a homogeneous model (see Appendix B). The estimated sideband intensity by this simple model agrees reasonably well with satellite measurements [e.g., Heyborne, 1966; Burtis, 1974; Inan et al, 1977].

Chapter II

VLF PULSE PROPAGATION IN THE MAGNETOSPHERE

A. Introduction

In this chapter, we discuss the problem of VLF pulse distortion due to propagation through dispersive media. Recently, investigations on the interactions between whistler-mode (WM) signals and energetic electrons have been carried out experimentally by injecting RF pulses into the magnetosphere [Helliwell and Katsufrakis, 1974; Koon et al, 1976]. Among the results of this work are wave growth and triggering emissions on the output signal as received on the ground. But the front end of a pulse may have been distorted by dispersion in such a way that it could appear to have been amplified. Without knowing how a pulse is distorted after traveling through the magnetosphere, we may draw wrong conclusions about wave-particle interaction (WPI) processes based solely on the observed data. Furthermore, the pulse may have been stretched enough in the front by the time it arrives at the interaction region to significantly alter the details of the WPI processes. Thus, it is essential to study the problem of pulse propagations in the magnetosphere.

Pulse propagation in a dispersive medium is a well-known problem [Brillouin, 1960] on which numerous papers have been written. Most (if not all) of these studies are carried out in homogeneous media [e.g., Haskell and Case, 1967; Ronnang, 1968; Vidmar and Crawford, 1975; Seyler et al, 1972; Buckley, 1975]. As far as we know, this is the first time that the distortion of a VLF pulse propagating in an inhomogenous medium, the magnetosphere, has been calculated.

One of the most popular approaches in studying pulse propagation is to obtain an approximate analytical expression for the envelopes of the distorted pulses by using the saddle-point method of integration [Brillouin, 1960; Budden, 1966; Haskell and Case, 1967; Ronnang, 1967; Vidmar and Crawford, 1975]. A less popular approach was adopted by Seyler et al [1972] to study pulse propagation numerically in a lossy but homogeneous magnetoplasma. In their study, they took advantage of the available fast Fourier transform (FFT) technique to decompose a pulse train into its Fourier components, then allowed each component to propagate through the medium separately and, finally at the points of interest, added all the components together by taking the inverse Fourier transform to obtain the amplitude vs time of the distorted pulse.

Formulation of the problem of pulse propagation through a slowly varying medium by any of the analytical methods becomes tedious and complicated. Numerical methods using the FFT technique, on the other hand, require only a knowledge of the phase delays and a local modification on the amplitudes of these frequency components. Therefore, the numerical approach is more attractive than the analytical methods of solving the problem of pulse propagation in a slowly varying inhomogeneous medium.

We are interested in the propagation of a whistler-mode (WM) pulse along a duct in the magnetosphere. By using a well-developed model for electron concentrations along a duct [Angerami, 1966; Park, 1971] and by assuming a dipole model for the geomagnetic field, the phase velocity v_p in every point along the path for each frequency component in a whistler-mode can be easily calculated by the dispersion relationship

$$\frac{c^2}{v_p^2} = 1 - \frac{f_p^2}{f(f - f_H)} \qquad (2.1)$$

where f_p and f_H are the plasma frequency and the gyrofrequency, respectively. The phase delay can then be obtained by

$$t_{ph} = \int_0^z \frac{ds}{v_p} \tag{2.2}$$

We have assumed that the spatial variation is so small that the phase velocity is constant within a wave length.

In the next section, we describe the method of study in detail. In Section C, WM pulse propagation in a homogeneous magnetoplasma is studied. The group velocity is reproduced. Some dispersion characteristics of a WM wave can be seen easily. It is observed that the distortions of a pulse depend on its carrier frequency. In Section D, the problem of pulse propagation along a duct in the magnetosphere is studied. The pulse shape is monitored at six locations along the path. The distortion of a pulse depicts the importance of the choice of the carrier frequency. We demonstrate that it is possible to choose a frequency at which the pulse envelope shows a minimum distortion at a particular location along the path. Discussions and conclusions are presented in Sections E and F, respectively.

B. Theory

An RF pulse has a frequency spectrum centered at its carrier frequency. The bandwidth of the spectrum, roughly speaking, equals the inverse of the pulse duration. In a dispersive medium, the phase velocities of various frequency components of the spectrum are different. As the pulse travels through a distance L, the phase of each frequency component is retarded according to its phase velocity. As a result, the

pulse shape is altered. It is generally (but not always) true that the longer the propagation distance, the greater the distortion.

We shall limit ourselves to cases in which the media are linear and lossless. Suppose that a pulse propagates from $z = 0$ to $z = z_1$ and that the electric or magnetic field at $z = 0$ is

$$a(t,z)\big|_{z=0} = a(t,0) = q(t) \sin 2f_c t \tag{2.3}$$

where

$q(t)$ is bound in time

f_c = carrier frequency

Now, let us express $a(t,0)$ as a Fourier integral

$$a(t,0) = \int_{-\infty}^{\infty} A(f,0)\, e^{2\pi i f t}\, df \tag{2.4}$$

where

$$A(f,0) = \int_{-\infty}^{\infty} a(t,0)\, e^{-2\pi i f t}\, dt \tag{2.5}$$

In general, $A(f,z)$ is a complex function and can be separated into a real and an imaginary part as

$$A(f,z) = A_r(f,z) + iA_i(f,z) \tag{2.6}$$

where

$$A_r(f,z) = \int_{-\infty}^{\infty} a(t,z) \cos 2\pi f t dt \tag{2.7}$$

$$A_i(f,z) = -\int_{-\infty}^{\infty} a(t,z) \sin 2\pi f t dt \tag{2.8}$$

$A(f,z)$ can also be expressed as an amplitude and a phase part as

$$A(f,z) = A_m(f,z) \exp\left[iA_{ph}(f,z)\right] \tag{2.9}$$

where

$$A_m(f,z) = \left[A_r^2(f,z) + A_i^2(f,z)\right]^{1/2} \tag{2.10}$$

$$A_{ph}(f,z) = \tan^{-1} \frac{A_i(f,z)}{A_r(f,z)} \tag{2.11}$$

Unlike a pulse propagating in a homogeneous and nondispersive medium, in which the phase of its spectrum is linearly retarded (e.g., proportional to the frequencies of the components), the phase retardation of a pulse propagating in a homogeneous and dispersive medium depends on the details of the dispersion relationship. In general, the phase retardation in such a medium is not linearly proportional to the frequencies of the components. As a result of this nonlinear phase retardation, the temporal shape of the pulse becomes distorted. In addition to the nonlinear phase retardation, there is a change in the relative amplitudes of the components of a pulse which propagates in an inhomogeneous and dispersive medium. In a slowly varying medium, this change is a local effect; it is discussed in Section D.

1. Homogeneous and Nondispersive Medium

The terms "homogeneous" and "nondispersive" imply that the phase velocity v_p is independent of space and frequency, respectively. Having traveled from $z = 0$ to $z = z_1$, a pulse has a spectrum given by

$$A(f,z_1) = A_m(f,z_1)\ \exp\left[iA_{ph}(f,z_1)\right] \tag{2.12}$$

where

$$A_m(f,z_1) = A_m(f,0) \tag{2.13}$$

$$A_{ph}(f,z_1) = A_{ph}(f,0) - 2\pi f\ \frac{z_1}{v_p} \tag{2.14}$$

Note that the phase retardation $2\pi f(z_1/v_p)$ is linearly proportional to the frequency f. It can be easily shown that

$$A(f,z_1) = A(f,0)\ \exp\left(-i2\pi f\ \frac{z_1}{v_p}\right) \tag{2.15}$$

We can obtain the signal in the time domain simply by taking the inverse transform of Eq. (2.15).

$$a(t,z_1) = \int_{-\infty}^{\infty} A(f,0)\ \exp\left[-i2\pi f\ \frac{z_1}{v_p}\right] e^{i2\pi ft}\ df = a\left(t - \frac{z_1}{v_p},0\right) \tag{2.16}$$

that is,

$$a(t,z_1) = q\left(t - \frac{z_1}{v_p}\right)\ \sin\ \left[2\pi f\left(t - \frac{z_1}{v_p}\right)\right] \tag{2.17}$$

Equation (2.17) indicates that the pulse has just been retarded by a time z_1/v_p and has no distortion at all.

2. Dispersive Medium

The phase velocities of various frequency components are different in a dispersive medium. In general, the phase velocities can be found through a dispersion relationship which characterizes the medium.

The amplitude and phase of a frequency component, after traveling from $z = 0$ to $z = z_1$, can be written as

$$A_m(f,z_1) = A_m(f,0) \cdot m(f,z_1)$$
$$A_{ph}(f,z_1) = A_{ph}(f,0) - \int_0^{z_1} 2\pi f \frac{dz}{v_p(f,z)} \tag{2.18}$$

where $m(f,z_1)$ is the amplitude modulation function. In a slowly varying medium, $m(f,z_1)$ depends only on the refractive index at z_1. In a homogeneous medium, it is unity.

It is noticed that the phase retardation $\int_0^{z_1} 2\pi f(dz/v_p(f,z))$ is not a linear function of frequency in general.

The spectrum of $z = z_1$ can be expressed as

$$A(f,z_1) = m(f,z_1)\, A(f,0) \exp\left(-i \int_0^{z_1} 2\pi f \frac{dz}{v_p(f,z)}\right) \tag{2.19}$$

The corresponding signal is

$$a(t,z_1) = \int_{-1}^{\infty} m(f,z_1)\, A(f,0) \exp\left[i2\pi f\left(t - \int_0^{z_1} \frac{dz}{v_p(f,z)}\right)\right] df \tag{2.20}$$

Equation (2.20), in general, cannot be expressed in terms of $a(t,0)$ easily. By realizing that $a(t,z_1)$ is the inverse Fourier transform of $m(f,z_1)\, A(f,0) \exp[-i \int_0^{z_1} 2\pi f dz/v_p(f,z)]$, and by recollecting that $A(f,0)$ is the spectrum of the input pulse, and that $v_p(f,z)$ can easily be obtained from proper dispersion relations, we can obtain $a(t,z_1)$ numerically by taking advantage of the available fast Fourier transform (FFT) algorithm for both homogeneous and slowly varying media.

We have summarized the method of the simulation of a VLF pulse propagating in a dispersive medium by a flow chart shown in Fig. 2.1.

Because of the discrete nature of the operation in digital computers, analog signals must be sampled first in order to be "manipulated" by digital computers. In our case, both a time domain signal and the corresponding spectrum in the frequency domain would have to be represented by a sequence of numbers properly spaced.

Figure 2.2 shows how sampling in the time domain with a sampling frequency f_s implies generating replicas of the spectrum in the frequency domain at the frequency intervals f_s [e.g., Bracewell, 1965]. The well-known sampling theorem stating that f_s must be equal to or greater than twice the bandwidth of the signals is sufficient to guarantee that the replicas do not overlap. We can always obtain the original signal in the time domain by low-pass-filtering of a properly sampled signal.

Similarly, sampling the frequency spectrum of a single pulse corresponds, in the time domain, to generating a pulse train with a repetition rate equal to the frequency spacing between the samples in the spectrum. We have to work with pulse trains in our approach to the problem. But the repetition rate of the pulses can be chosen as low as we want so that the pulses do not overlap. Furthermore, we shall be able to pick a time window, just as we picked a proper low-pass filter in the previous case, so as to describe a single pulse instead of a pulse train.

Because of this discrete feature of FFT, we are physically monitoring a pulse train instead of a single pulse. The period of this pulse train is fixed in our simulation and equals 512 ms. The received signal at each monitoring station is periodic and has a period of 512 ms.

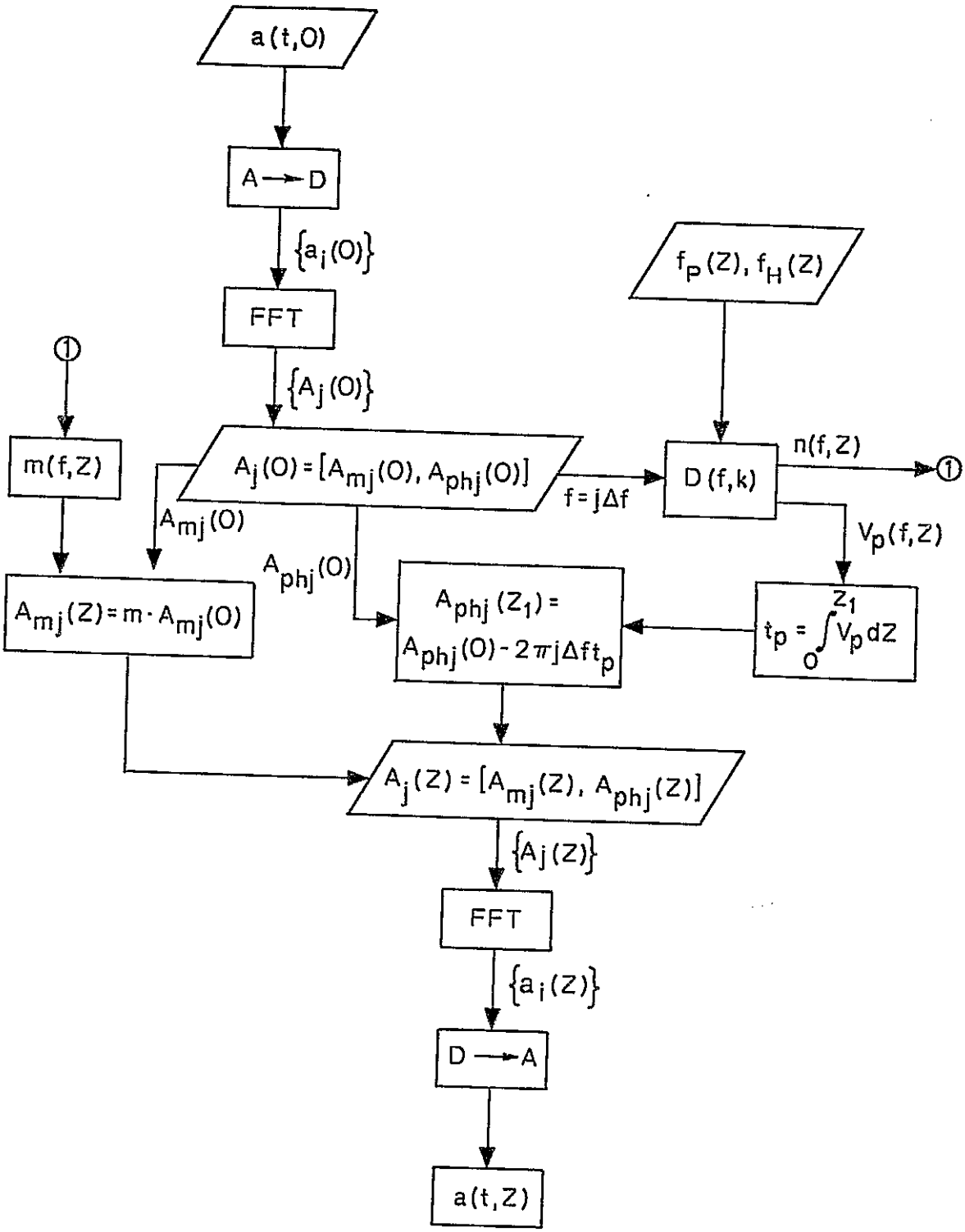

Fig. 2.1. FLOW CHART OF THE METHOD OF INVESTIGATING VLF PULSE PROPAGATION IN THE MAGNETOSPHERE.

a. A time domain waveform g(t) and the corresponding frequency domain spectrum G(f)

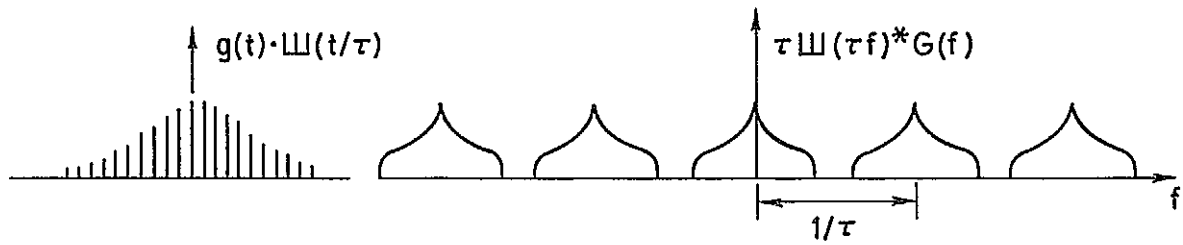

b. A properly sampled case

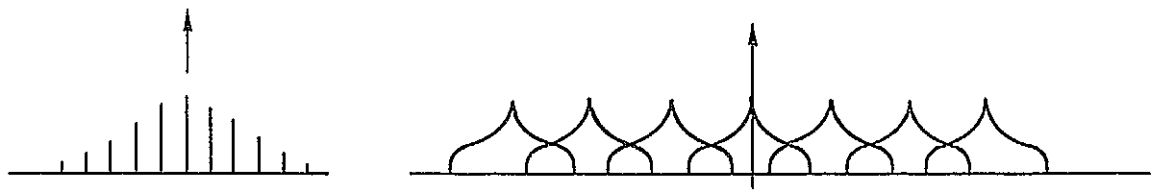

c. An undersampled case

Fig. 2.2. DEMONSTRATION OF THE SAMPLING THEOREM. $\tau = 1/f_s$.

Therefore, by monitoring the signals at every station for only 512 ms, we shall have all of the information we need regarding the pulse distortion.

C. Propagation in a Homogeneous Model

Simulation of WM pulses propagating longitudinally is carried out in a model with a plasma density of 400 electrons per cc and a gyrofrequency of 13 kHz for various carrier frequencies. These values are appropriate to the equatorial region near $4R_E$ in the magnetosphere. The results have been translated down in frequency so that the carrier frequency of the input pulse is always displayed at 500 Hz. The real carrier frequency may be several kHz.

Since WM waves are circularly polarized, a three-dimensional picture is required to illustrate a WM wave. But we can always reconstruct a 3-D picture by two plane-projections perpendicular to each other. Furthermore, the plan projections of a perfect circular wave differ from each other only in a fixed phase relationship. Therefore, only one projection of the WM wave, as shown in Fig. 2.3, is required to illustrate the feature of the wave.

According to whistler theory [Helliwell, 1965], the group velocity can be written as

$$v_g = 2C \frac{f^{1/2}(f_H - f)^{3/2}}{f_p f_H} \tag{2.21}$$

where

f = wave frequency

f_H = gyrofrequency

f_p = plasma frequency

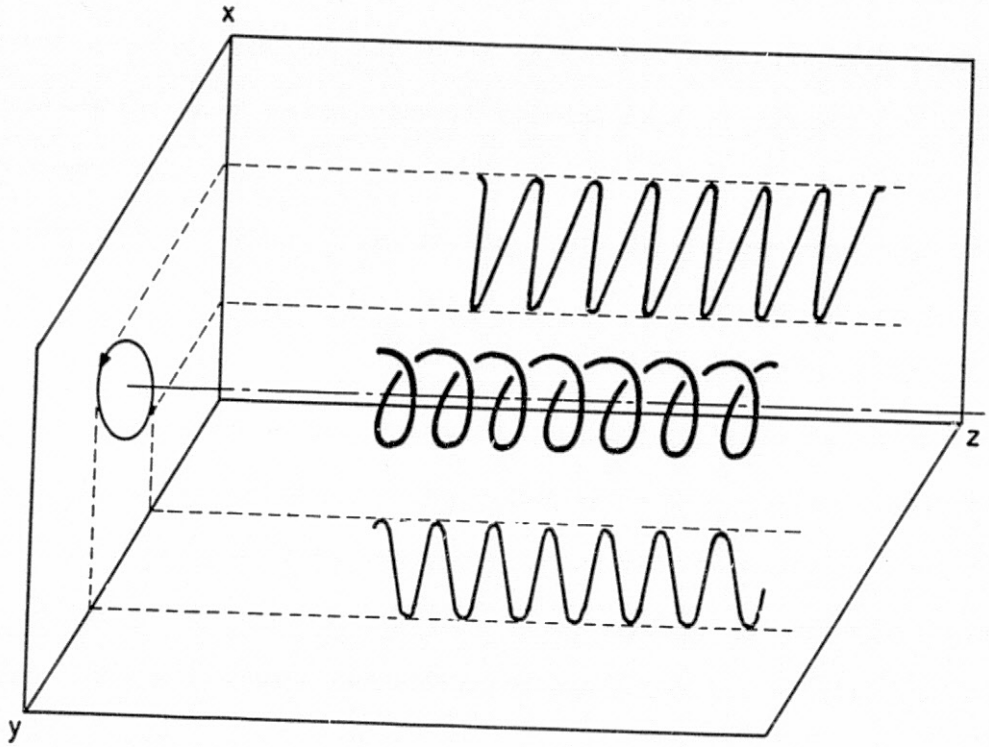

Fig. 2.3. DECOMPOSITION OF A CIRCULARLY POLARIZED SIGNAL INTO TWO LINEARLY POLARIZED SIGNALS.

The group velocity vs frequency is sketched in Fig. 2.4. The maximum group velocity occurs at $f = f_H/4$ and equals

$$v_{g\ max} = \frac{\sqrt{27}}{8}\, c\, \frac{f_H}{f_p} \tag{2.22}$$

In the model, the maximum group velocity occurs at $f = 3.25$ kHz and has a value of 14073 km/sec. An RF pulse at this frequency requires 71.06 ms to travel through 1000 km.

In the simulation, we use phase velocities to calculate the phase retardations for all the frequency components. We have not used the idea of group velocity. However, our simulation result shows that the center* of a RF pulse indeed propagates with the group velocity (within a measurement error of 1 percent).

Figure 2.5 illustrates a simulation of WM pulses propagating along the magnetic field direction. The six panels illustrate the amplitude vs time records monitored at six locations along the path. The spacing between the monitoring stations is 1000 km. The 50 ms pulse is injected into the magnetoplasma at the 10th msec at the first location ($s = 0$ km). It is noticed that the pulse has not been distorted very much and that the difference of the arrival time at the center of the pulse at two adjacent monitoring stations is about 71 ms. Because the measured delay and the theoretical group delay are nearly the same, we conclude that the wave packet is indeed traveling with the group velocity in the magnetoplasma.

*The center of a distorted pulse is defined as the center of the interval within which the signal exceeds 30 percent of the peak value.

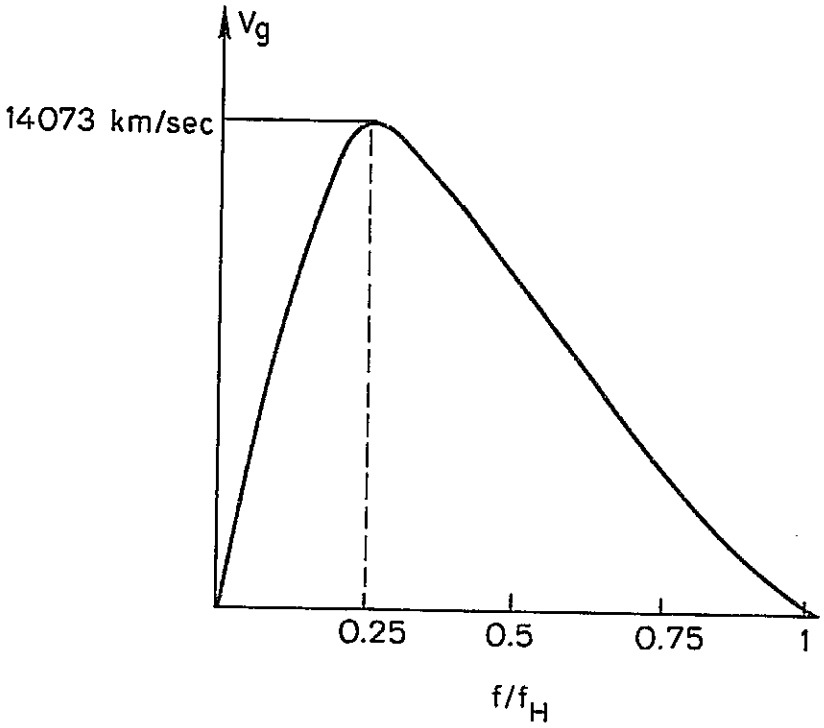

Fig. 2.4. A PLOT OF GROUP VELOCITY VS FREQUENCY OF A WM SIGNAL PROPAGATING IN A HOMOGENEOUS MAGNETO-PLASMA IN WHICH f_N = 180 kHz AND f_H = 13 kHz.

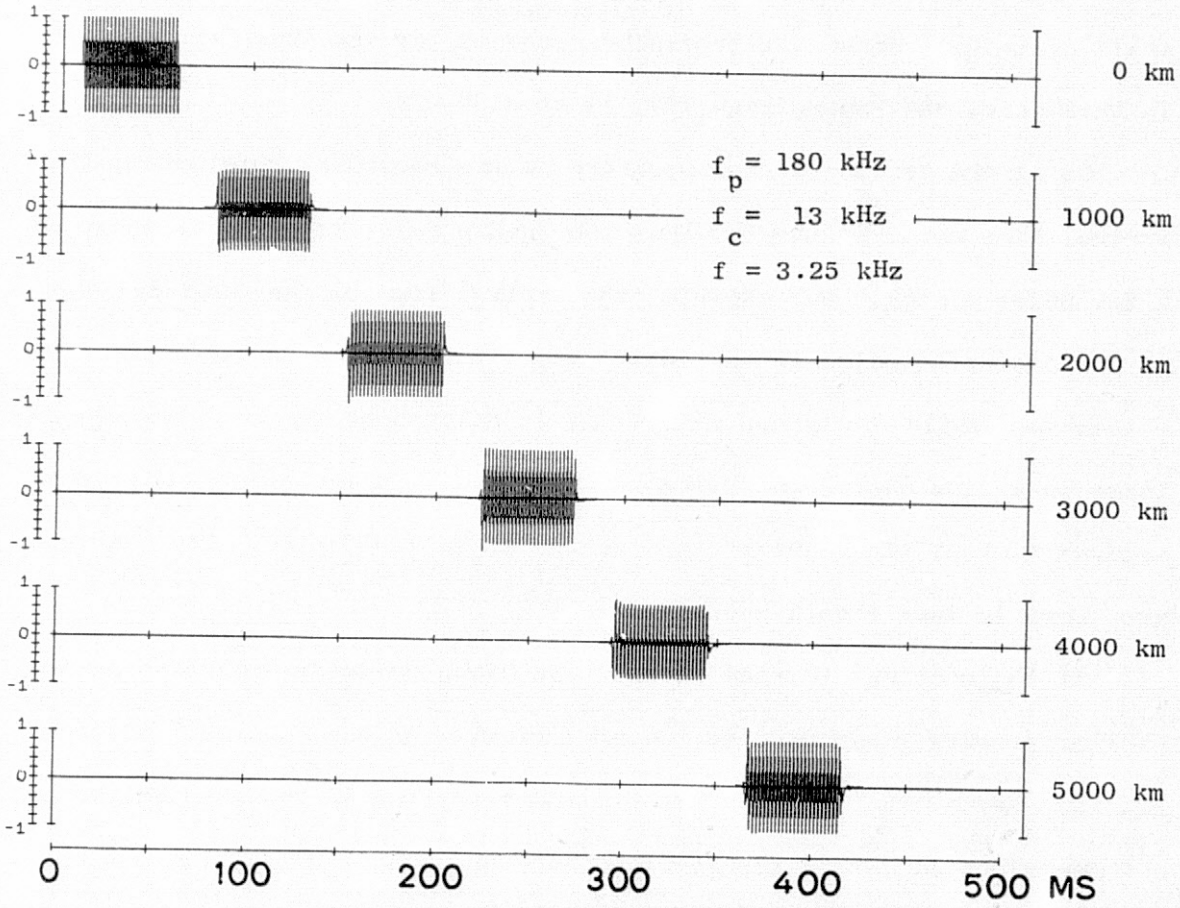

Fig. 2.5. PROPAGATION OF A 50 ms PULSE AT f = 3.25 kHz THROUGH THE HOMOGENEOUS MAGNETOPLASMA.

Figure 2.6 shows the dispersion of 20 msec pulses at different frequencies over a fixed path of length (25000 km). The pulses were injected into the magnetoplasma at -1.526 second. The carrier frequencies are 4.25, 3.75, 3.25, 2.75, 2.25, and 1.75 kHz. It is noticed that the pulse at 3.25 kHz propagates the fastest and has the minimum distortion. We shall call the frequency with minimum group delay the "nose frequency." In this case, the "nose frequency" is at 3.25 kHz.

Using the leading edges appearing on the record as references, the arrival time could be shorter than the "group delay time" by as large as a few pulse widths. For example, the arrival time of the leading edge of the distorted pulse in the lowest panel in Fig. 2.6 is measured to be ~1.846 sec while the group delay time is calculated to be 1.953 sec. There is a time discrepancy of about 100 msec. On the other hand, the arrival time of the "center" is measured to be 1.955 msec. The discrepancy here is less than 1 percent.

It is important to realize that the group velocity evaluated at the carrier frequency can predict the arrival time of the "center," not the leading edge of the pulse. This statement applies in the frequency range not too close to either the gyrofrequency or zero frequency, where the phase velocity equals zero. In the model we use here, the valid frequency range of the carrier of a pulse longer than 10 ms is about from 500 Hz to 12.5 kHz.

Other important features depicted by Fig. 2.6 are:

(1) The distortion of a pulse depends on its carrier frequency; the further away from the "nose frequency," the more the distortion. It is generally true that the distortion is larger below the "nose frequency" than above the "nose frequency."

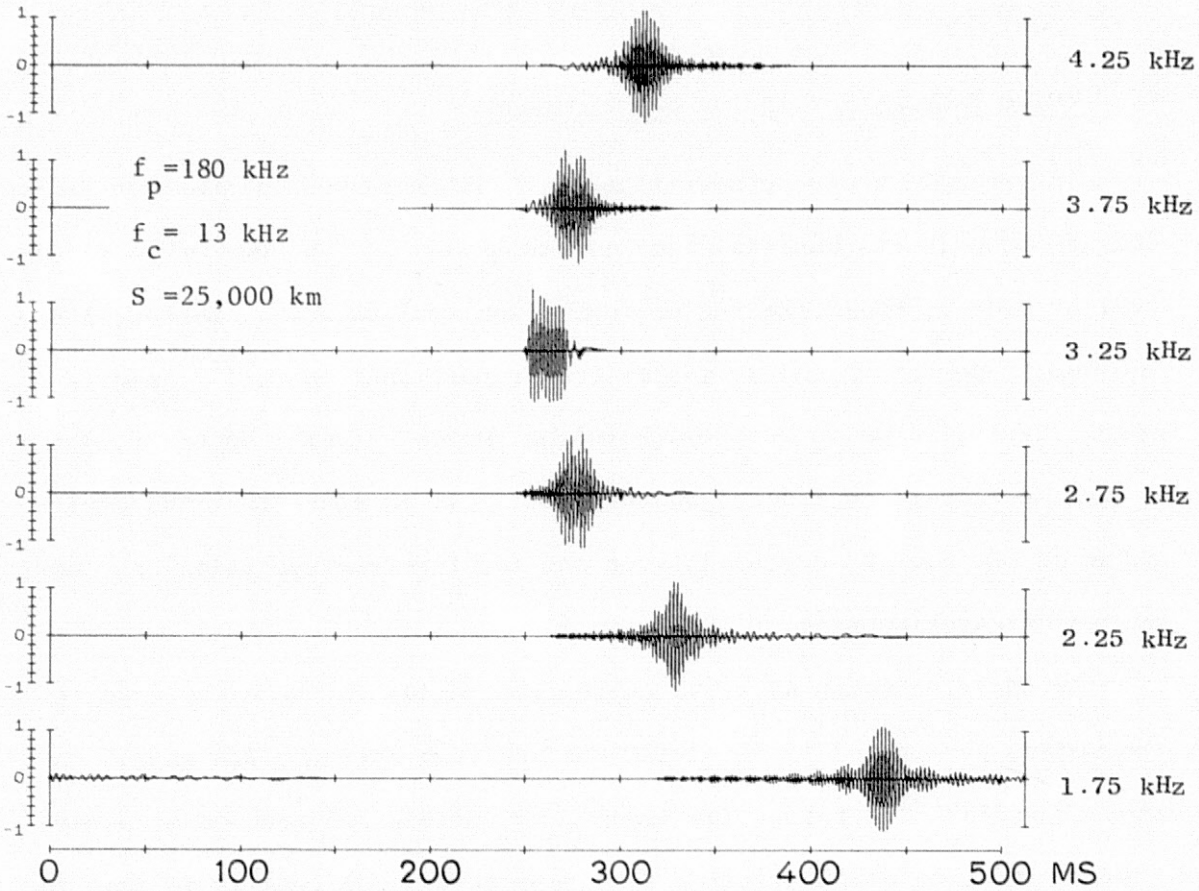

Fig. 2.6. PROPAGATION OF SIX 20 ms PULSES AT 1.75, 2.25, 2.75, 3.25, 3.75, AND 4.25 kHz THROUGH THE HOMOGENEOUS MAGNETOPLASMA FOR 25,000 km. The pulses are injected at -1.526 sec.

(2) When the carrier is above the "nose frequency," the low frequency components arrive before the main wave packet and the high frequency components arrive behind the packet. When the carrier is below the "nose frequency," this sequence is reversed; the high frequency components arrive first, the low frequency components later.

D. Pulse Propagation in the Magnetosphere

In general, a wave propagating in an inhomogeneous dispersive medium changes both in its amplitude and in its phase. In a spatially slowly varying medium, where the WKB approximation applies [e.g., Budden, 1966], the amplitudes of E and H fields are proportional to $n^{-1/2}$ and $n^{1/2}$, respectively, so as to keep the Poynting vector $|E \times H|$ constant, where n is the refractive index [Budden, 1966]. It is clear that the amplitudes of E and H depend only on the local refractive index n, not on the propagation path.

In the simulation of a VLF pulse propagating in the magnetosphere, the medium is assumed to be slowly varying such that the WKB approximation is valid. The refractive indices at various frequencies at a particular location of observation have been normalized locally so that the refractive index at the carrier frequency is unity in calculating differential amplitude changes. The absolute amplitudes are lost in the normalization process, but the ratios between the various frequency components are preserved.

It will be shown later that the differential change in amplitudes of the frequency components in a slowly varying medium has very little effect on the distortion of a pulse. The major contribution to the distortion comes from the nonlinear phase retardation in the frequency components.

The key to solve the problem is to calculate the phase delay time for each frequency component. The phase velocity of any frequency component at a location where the gyrofrequency and plasma frequency are specified is given by

$$v_p(f,z) = c \frac{f^{1/2}\left[f_H(z) - f\right]^{1/2}}{f_p(z)} \tag{2.23}$$

We have assumed that the refractive index is much greater than unity.

A diffusive equilibrium (DE) model [Angerami, 1966] is used to describe the magnetosphere in the simulation. There is empirical evidence in support of a DE model inside the plasmapause under normal conditions [Angerami, 1966; Park, 1971]. A dipole magnetic field is used to model the geomagnetic field. In this model, the gyrofrequency and the plasma frequency at every point are given once the L value and equatorial plasma density is given. L is the McIlwain parameter [McIlwain, 1961] that specifies a magnetic shell surrounding the earth. In a dipole model, a magnetic shell is labeled by an L when the shell's equatorial radius equals L times of the earth radius.

The phase velocities can be obtained for all the frequency components at every location along a duct through Eq. (2.23). The phase delay time at $z = z_1$ can then be calculated numerically by

$$t_p(f,z_1) = \int_0^{z_1} \frac{dz}{v_p(f,z)} \tag{2.24}$$

The distorted pulse at the "monitoring station" at $z = z_1$ is obtained by modifying the amplitude and phase of each frequency component according to the refractive index and the phase delay at z_1 and then

adding all the components together by taking the inverse Fourier transform via the FFT.

The inserted sketch in Fig. 2.7 shows the locations of the six monitoring stations along a duct at $L = 4$. Pulses are injected into the magnetosphere at Location 1 regularly at the rate of one pulse in every 512 ms. The arc length from Location 1 to Location 6 is about 30,000 km. The magnetosphere is modeled by the DE-1 model [Park, 1971], and the equatorial density is assumed to be 400 electrons per cc.

Figure 2.7 depicts the distortion of a pulse as it propagates from Location 1 to Location 6. A 10 ms pulse at 5.065 Hz is injected at the 10th ms at Location 1. As it propagates along the duct, its shape changes. The high frequency components appear to reach the first five monitoring stations prior to the main body of the wave packet, while the low frequency components lag behind. It should be pointed out that the pulse shown in Locations 1, 2, 3, and 4 is the same one injected at the 10th ms at Location 1 and it arrives at Locations 5 and 6 after the 512th ms. The pulse shown in Locations 5 and 6 is actually the one injected into the magnetosphere at -502 ms from Location 1.

It is interesting to notice that the distortion is minimum at the equator (Location 6) at this particular frequency and that the travel time from Location 1 to the equator is about 942 ms. According to Park's result [1971], the one-hop minimum group delay for a whistler propagating at $L = 4$ in the same model magnetosphere occurs at about 5063 Hz and equals approximately 1.88 seconds. The frequency at which the minimum one-hop delay occurs is called the "nose frequency," f_{ns}. Traveling from an end of a duct to the equator requires half of the one-hop time. There is very little discrepancy between our result (942 ms) and Park's

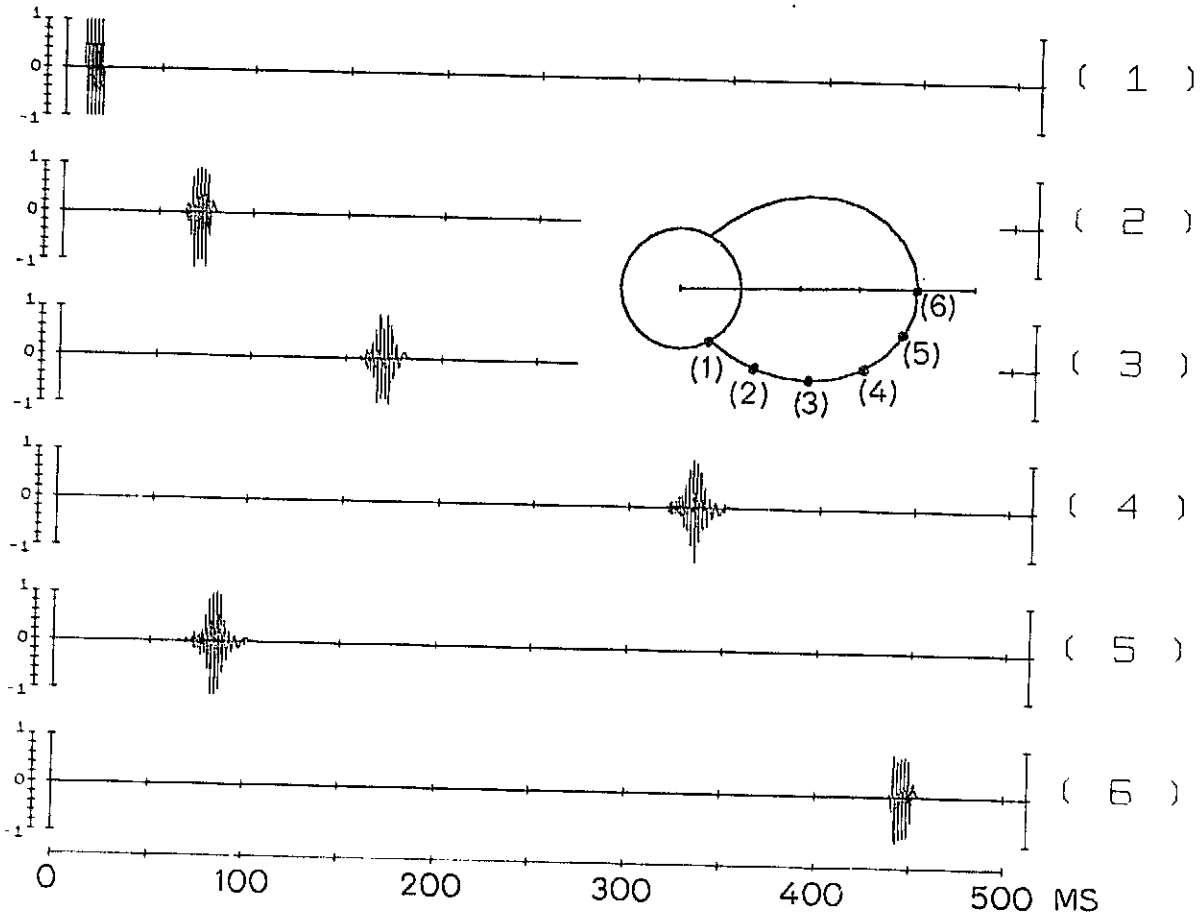

Fig. 2.7. PROPAGATION OF 10 ms PULSES AT 5.065 kHz THROUGH A DUCT AT L = 4 IN A DE-1 MODEL MAGNETOSPHERE. The pulses are monitored at six stations from 1000 km above the earth to the equator.

(940 ms). In his study, group velocities were employed to calculate the group delays for whistlers. In our simulation, on the other hand, the idea of group velocity has never been applied. It is interesting to realize that these two approaches give almost identical results for the delay time of a signal traveling in the magnetosphere.

Pulses injected at other carrier frequencies, f_c, show different features of distortion. Examples of 10 ms pulses at 7.075, 6.065, 4.065, and 3.065 Hz are illustrated in Figs. 2.8, 2.9, 2.10, and 2.11, respectively. It can be seen that the delay time from Location 1 to the equator is indeed a minimum for the pulse at 5.065 Hz.

When $f_c > f_{ns}$, the low frequency components arrive at the equator prior to the main wave packet and the high frequency components lag behind. There is always a location at which the distortion is minimum, as illustrated by the waveform at Location 5 in Fig. 2.8. The arrival sequence of high and low frequency components at Location 4 is the reverse of that of Location 6.

When $f_c < f_{ns}$, the high frequency components arrive at the equator first and the low frequency components last. The further the carrier frequency is away from f_{ns}, the greater the distortion.

E. Discussion

In addition to the "slowly varying" assumption in the simulation of pulses propagating along a duct in the magnetosphere, we have assumed that all frequency components propagate strictly parallel to a geomagnetic field line. Exactly longitudinal propagation seems unlikely to occur. In fact, various frequency components follow different snake-like paths inside a duct. However, in light of the theory of whistler propagation

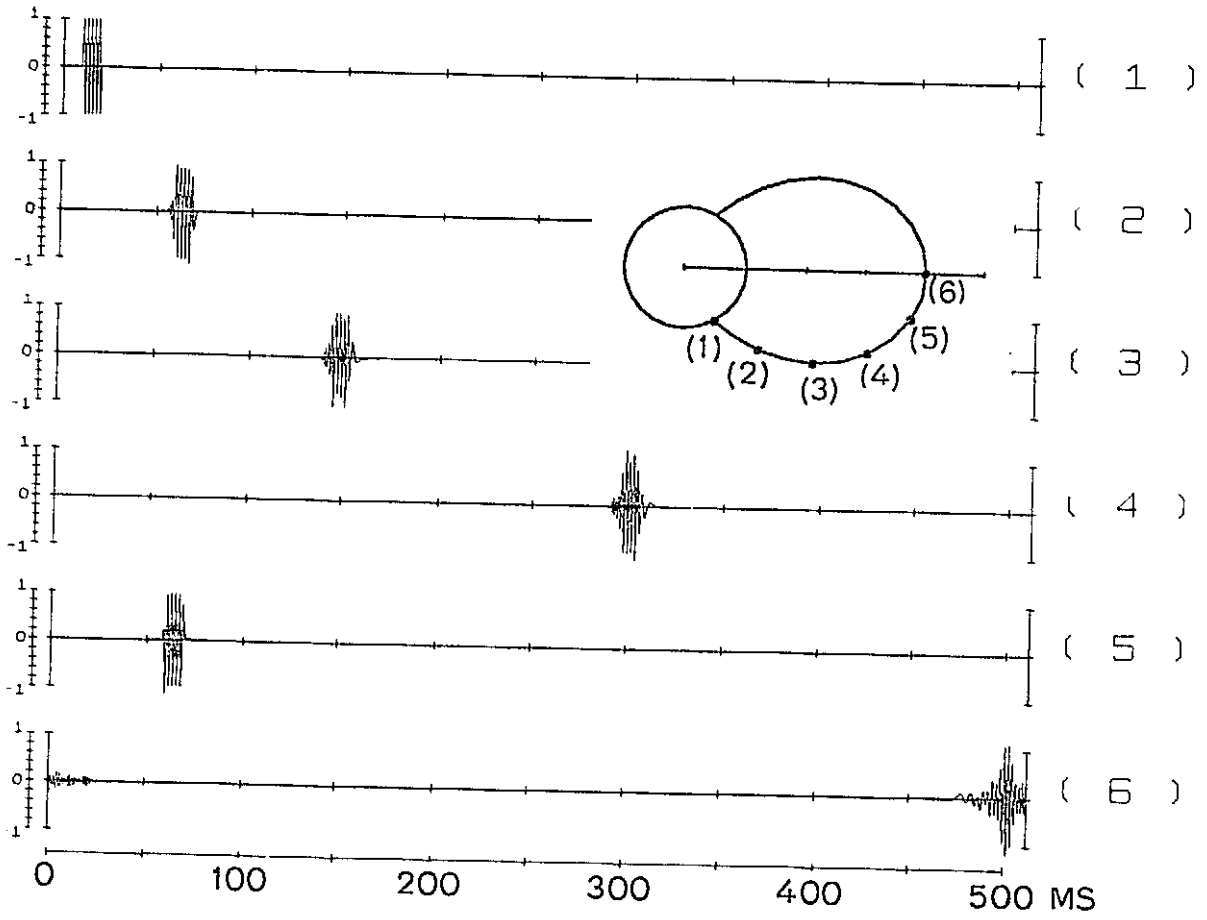

Fig. 2.8. PROPAGATION OF 10 ms PULSES AT 7.065 kHz IN THE MODEL MAGNETOSPHERE.

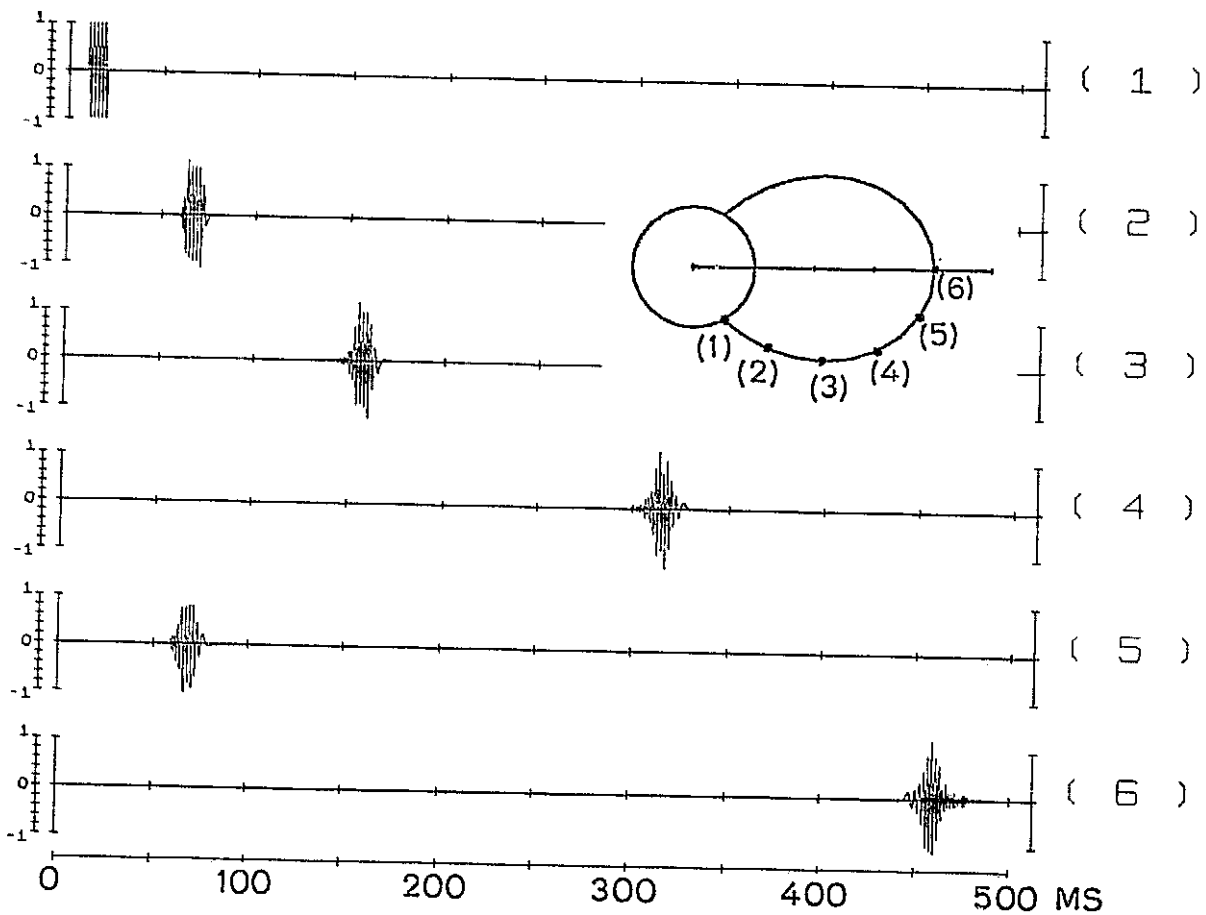

Fig. 2.9. PROPAGATION OF 10 ms PULSES AT 6.065 kHz IN THE MODEL MAGNETOSPHERE.

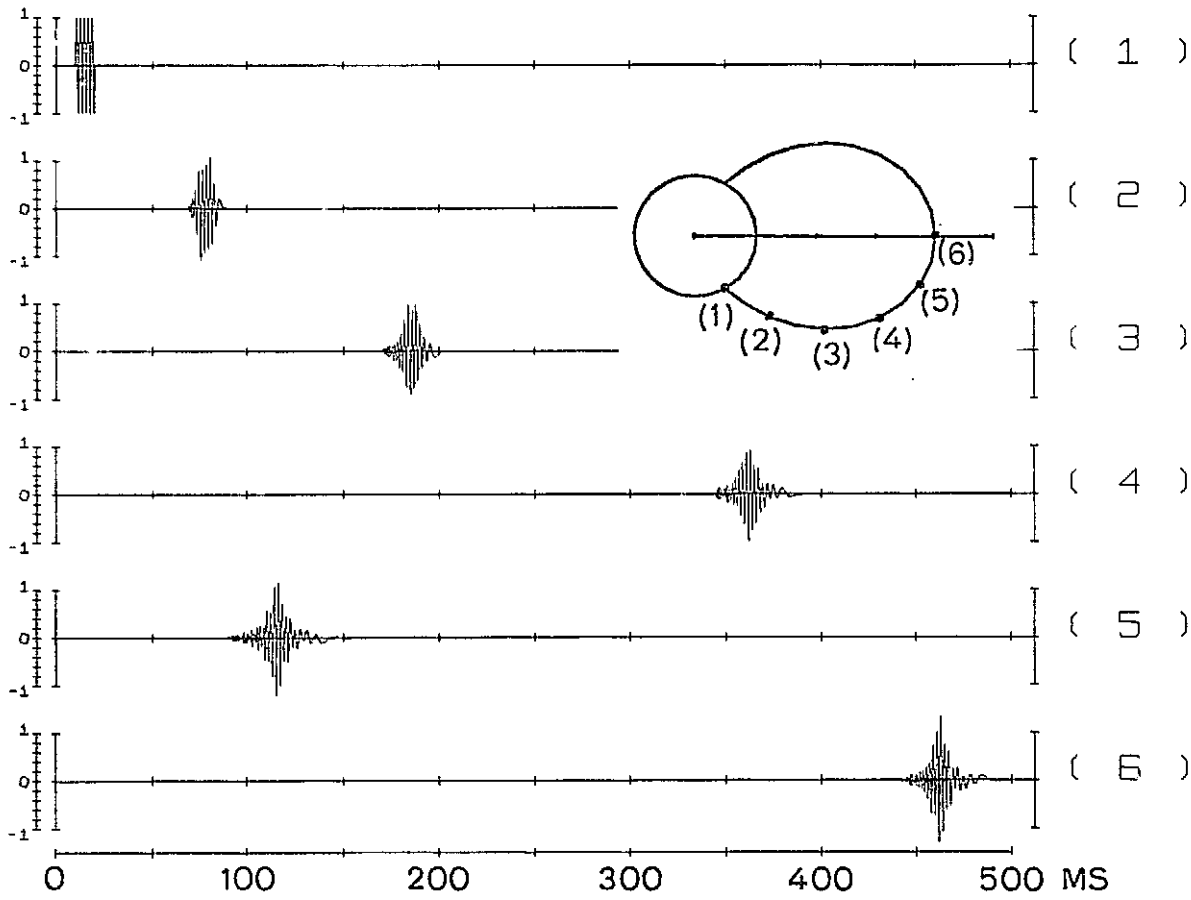

Fig. 2.10. PROPAGATION OF 10 ms PULSES AT 4.065 kHz IN THE MODEL MAGNETOSPHERE.

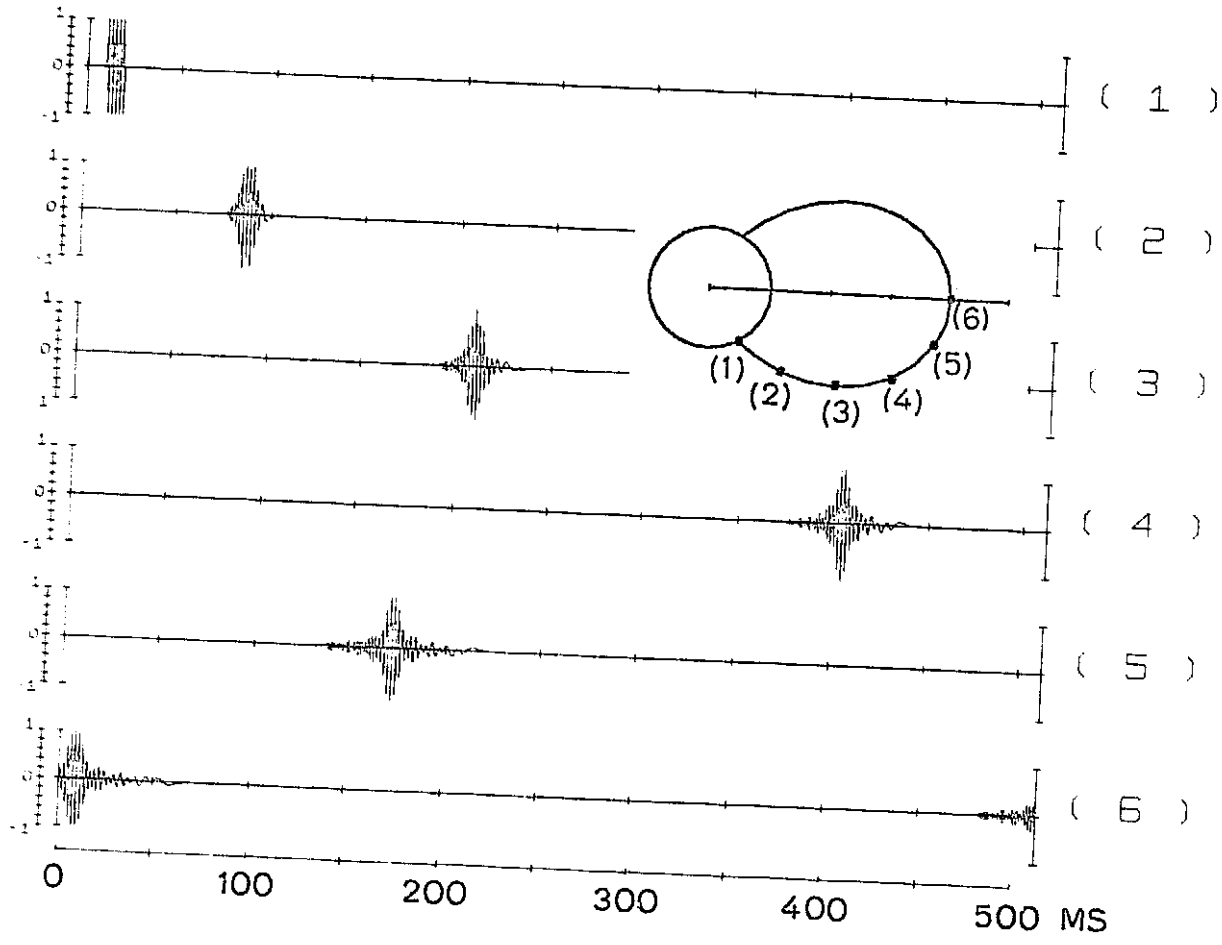

Fig. 2.11. PROPAGATION OF 10 ms PULSES AT 3.065 kHz IN THE MODEL MAGNETOSPHERE.

[Smith, 1961], this assumption appears to be a reasonable approximation for wave propagation below half of the local gyrofrequency inside a duct. On the other hand, exact raytracing for all frequency components inside a duct can, in principle, be included in the simulation if necessary.

A duct can trap WM waves just as an optical fiber can confine optical beams. The cross-sectional area of a duct is not uniform and is assumed to be inversely proportional to the local geomagnetic flux density. Therefore, wave intensity should reach a minimum on the equator since the largest "illumination area" occurs there. Since there is no differential amplitude change among the frequency components in a particular location due to the change in the cross section of a duct, it does not affect the pulse shape. Hence, it is not included in the simulation.

Under the "slowly varying" assumption, the reflected wave energy due to changes in the refractive index is neglected. Thus, a wave propagating in a slowly varying medium must have E and H fields which satisfy the following two physical conditions:

(1) Constant energy flow along the propagation path. In a lossless medium, the Poynting vector $|E \times H|$ shall be independent of the local refractive index, n [Budden, 1966].

(2) $|E/H| = Z_o/n$, where Z_o is the characteristic impedance of free space.

Hence, the electric field E and the magnetic field H are proportional to $n^{-1/2}$ and $n^{1/2}$, respectively. Note that this argument is not rigorous. For a more precise derivation, the reader is referred to Budden [1966]. The condition under which the WKB approximation holds is

$$\frac{1}{K^2}\left|\frac{1}{4}\left(\frac{1}{n^2}\frac{dn}{dz}\right)^2 - \frac{1}{2}\frac{1}{n^3}\frac{d^2n}{dz^2}\right| \ll 1 \qquad (2.25)$$

This relation is a quantitative definition of the term "slowly varying." It requires that the derivatives dn/dz and d^2n/dz^2 be sufficiently small and that n not be too small.

It is noticed that variations of the amplitudes of E and H are purely a local effect. As we mentioned before, normalization has been performed so that $n(f_c)$ equals unity in calculating the wave amplitudes at a particular location. The absolute wave amplitudes are lost in the normalization process. A true amplitude can be obtained by scaling the pulse amplitudes up or down by a factor of $\sqrt{n(f_c)}$ while the shapes remain the same.

The contribution to pulse distortion of the differential amplitude changes in the WKB approximation is small in comparison with that from the cumulative phase retardations. A 10 ms pulse at 3.065 Hz propagating along a duct at $L = 4$ has been simulated for two cases: one with and the other without the differential amplitude changes. The result (not shown) shows that the difference is negligible. This is because most energy (about 90 percent) of a 10 ms pulse is contained between $f_c + 100$ and $f_c - 100$ Hz. Even at the equator, where the maximum dispersion occurs, the amplitude corrections introduced by the WKB approximation within this 200 Hz bandwidth are always less than 1 percent. In general, if the pulse is not too short (say, > 5 ms) and the carrier frequency is far away from the local gyrofrequency and greater than, say, 500 Hz, the amplitude corrections can be neglected.

Knowing how a pulse is distorted by the dispersion in the magnetosphere is essential in interpreting the observed data of many VLF wave experiments. An important feature of a distorted pulse is that it has been stretched in the front in such a way that it appears to have an "exponential growth" when arriving at the receiving site. For example, in one wave injection experiment [Koon et al, 1976], phase alternating signals at 6.6 kHz were injected into the magnetosphere to investigate the effect of WPI due to phase reversing in the triggering waves. The data show that the amplitudes of the 6.6 kHz signal went to zero and recovered with a characteristic time constant of 33 ms whenever the phase of the triggering wave was reversed. This time constant was found to be about ten times longer than the antenna current response time. Koon et al [1976] concluded that the recovery in amplitude was due to the amplifications by WPI processes in the magnetosphere. The apparent "growth rate" was measured to be about 260 dB/sec, which was significantly higher than those commonly observed [Helliwell and Katsufrakis, 1974]. The growth time (~33 ms) was short in comparison with that obtained from other experiments. Furthermore, there was no other evidence of amplification or triggering of emissions at that period.

It was suggested by Helliwell [private communication] that the "growth" may be just another propagation phenomenon. A phase-reversing signal consists of several sections of RF pulses with the same carrier frequency. Any two successive pulses are 180° out of phase. As the phase-reversing signal propagates in the magnetosphere, the front and rear ends of each section will be distorted and stretched. Therefore, interference between successive pulses is expected during the transitions. There will be amplitude depletions during the transitions.

We have simulated a phase-reversing signal at 6.6 kHz traveling through a duct at $L = 3.1$. The equatorial plasma density is chosen to be about 1000 electrons per cm^3. These parameters are chosen to fit the nose frequency and minimum delay time reported by Koon et al [1976]. The result is shown in Fig. 2.12. The phase is alternated at $t = 0$ on a 100 ms pulse injected at -50 ms at Location 1. As the pulse propagates along the duct, a "gap" is developed near the time of phase alternation. When it reaches the equator, the gap becomes about 10 ms. We expect that the gap will be about 20 ms long when it reaches the conjugate point of Location 1. By considering the finite antenna current response time (~3.3 ms) and a finite time constant associated with the analyzers, we speculate that the gap will appear to be 30 to 40 msec, consistent with Koon's report [1976]. Under these circumstances, we conclude that it is the propagation distortion, not WPI, which causes the amplitude depression for about ~33 ms near the times of phase alternations.

Another important result from these studies is that the stretching of a pulse is large enough by the time it arrives at the interaction region to significantly alter the details of WPI processes. A pulse at 4 kHz propagating from an altitude of 1000 km up to the equator at $L = 4$ may be stretched about 30 msec in the front, comparable to a typical bunching time of 20 ms (see Helliwell and Crystal [1973], Fig. 4). It is therefore necessary to either consider this distortion in the front of a pulse in some of the studies of WPI or build equalizers in the future to compensate for such distortion. For example, the experiment of phase alternations can conceivably be carried out in the future by "preprocessing" the injected signal so that, when a phase-reversing signal reaches the interaction region, the phase of the signal will appear as

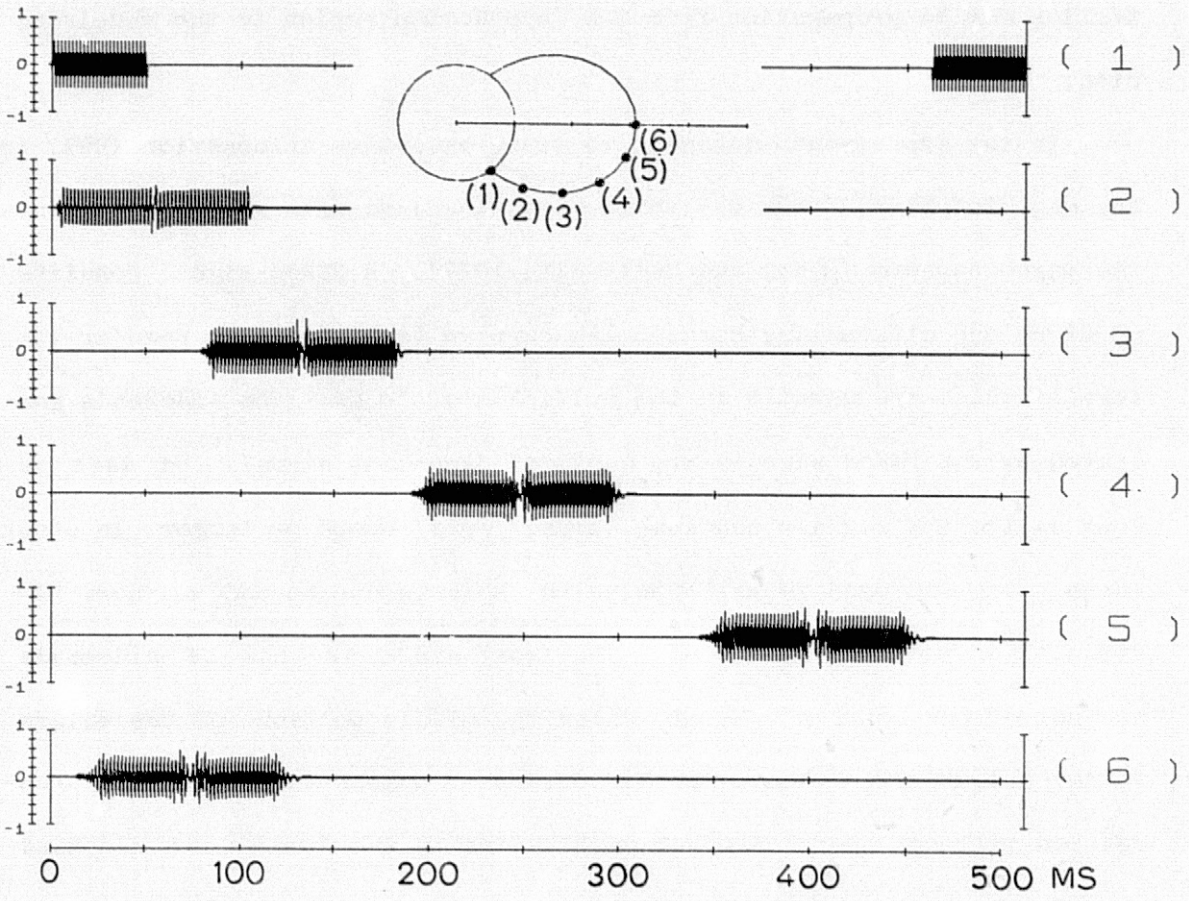

Fig. 2.12. PROPAGATION OF A 100 ms PULSE AT 6.6 kHz WITH A PHASE DISCONTINUITY THROUGH A DUCT AT L = 3.1. The discontinuity occurs at t = 0.

being reversed instantaneously. Figure 2.13 illustrates a pre-processed signal propagating along the duct at L = 3.1. As the signal reaches the equator, the signal becomes "clean." By the same principle, post-processing of the received signal can be implemented to compensate for the distortion due to propagation from the interaction region to the receiving site.

In the experiments designed to study wave-wave interaction (WWI) in the magnetosphere, frequency shift-keyed (FSK) signals are injected into the magnetosphere [Chang and Helliwell, 1977]. A FSKed signal consists of RF pulses alternating between two carrier frequencies at regular intervals which are usually in the multiples of 10 ms. The sidebands generated by the FSKed signals are constant frequency signals and last as long as the FSK signals continue, usually one second or longer. In other words, each sideband is an RF pulse which lasts one second or more instead of on the order of 10 ms. The front and rear ends of sidebands are not of our concern. We are using the middle portions of the pulses to investigate WWI. Thus, the distortion of pulses as a result of propagation will not jeopardize our conclusions in the studies of sideband mutual interactions.

F. Conclusion

Among the results of the study of pulse propagation in the magnetosphere are the following:

(1) By properly choosing the carrier frequency of injected pulses, the propagation effects can be minimized. The best frequency to choose is the "nose frequency" (as measured at the equator).

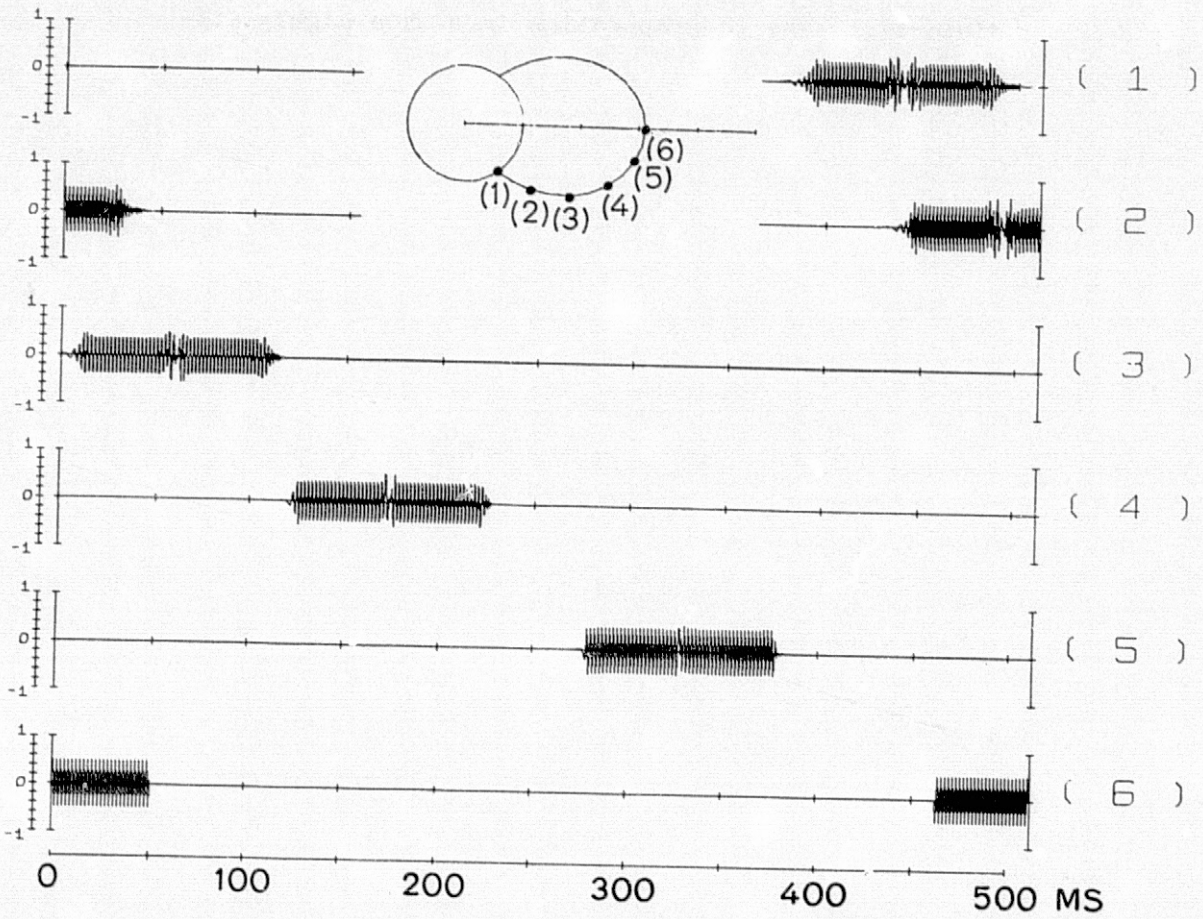

Fig. 2.13. PROPAGATION OF A PRE-PROCESSED 100 ms PULSE (WITH A PHASE REVERSAL) AT 6.6 kHz THROUGH A DUCT AT L = 3.1.

(2) In designing certain wave-injection experiments in the study of WPI processes in the future, such as the phase-alternation experiments, we should include pre- and post-processing filters in the transmitting and the receiving facilities, respectively, to remove the distortions due to propagation in such a highly dispersive medium.

Chapter III

GAP INDUCED EMISSIONS

A. Introduction

Recently, many VLF wave injection experiments have been performed to investigate the details of VLF wave-particle interaction (WPI) processes in the magnetosphere. As a result of this interaction, coherent VLF waves may grow exponentially with time and trigger a variety of emissions [Helliwell and Katsufrakis, 1974]. It is generally believed that the amplification and triggering mechanisms are due to cyclotron resonance between energetic electrons and VLF waves. Beyond that, there is no general agreement.

It has been suggested that coherent wave amplification is the result of the phase bunching of electrons [e.g., Helliwell, 1967]. The WM waves phase-bunch the electrons, producing transverse currents that cause the waves to grow. In Appendix B, we shall discuss the mechanisms of VLF wave-particle interaction in the magnetosphere to give the background and rationale for many VLF wave injection experiments related to this report.

In Section B, we present an unexpected and interesting result from one such experiment designed to study how the wave growth is affected by altering the phase of the triggering signal. The experiments have been conducted between Siple, Antarctica, and its conjugate point near Roberval, Quebec [Helliwell and Katsufrakis, 1974]. Because of inherent limitations of the Siple transmitter, a phase alternation in a VLF signal is achieved by inserting a 10 msec pulse offset in frequency from the main signal by several hundred hertz. The frequency offset is so large

that the 10 msec offset pulse does not interact significantly with the electrons in resonance with the main signal. The main signal can therefore be viewed as having been interrupted by a 10 msec gap. The portion of the signal behind the gap is either in phase or in antiphase with the one preceding the gap.

The data show that the post-gap growth rates and the saturation levels of the main signals are the same regardless of whether the phase of the triggering waves have been shifted by zero or π-radians during the 10 msec gaps. Furthermore, a rising emission often is induced by the 10 msec gap. This gap-induced emission closely resembles the tail-end emissions that frequently appear at the ends of constant frequency pulses. These gap-induced emissions may develop into fully independent rising emissions or they may be either suppressed or entrained by the main signals.

The key to an explanation of the phenomenon of gap-induced emissions is based on the hypothesis that the radiation from the wave organized electrons can switch from a forced mode to a natural mode at the end of the triggering wave. Triggered emissions are said to be in a natural mode because they are not driven by external sources. The amplified signals on (or near) the frequencies of triggering waves are in a forced mode since they are driven by the triggering waves. The detailed mechanism of the development of a natural mode emission is dealt with separately [Helliwell, 1978]. A qualitative explanation is presented in Section C.

A preliminary result from a new wave injection experiment (gap-triggering experiment) will be presented in Section D. This experiment has been designed to investigate how large a gap shall be to allow a falling

emission to become fully developed within the gap. One of the results confirms an earlier observation that falling emissions always start with a small rise in frequency [Stiles, 1974]. A new feature of WWI is identified. A post-gap signal can capture a gap-induced falling emission whose frequency is 90 Hz below the post-gap signal, causing the emission to turn around toward the positive frequency direction.

In Section E, the results are summarized and the recommendations for future studies on this subject are presented.

B. Examples of Gap-Induced Emissions

It is assumed that WM wave amplification and triggering in the magnetosphere are due to nonlinear phase-bunching of energetic electrons by VLF waves. The "phases" of electrons refer to the angles between the transverse velocity components of the electrons and the wave magnetic field. It was thought that the phase-bunched currents might be diminished by perturbing the phases of the bunched electrons. A transmitter program was proposed to study how the growth rate and the saturation level of a wave would be affected simply by reversing the phase of the triggering wave. The idea is shown in Fig. 3.1. Electrons are randomly distributed in phase initially. The wave organizes the electrons by $V_\perp \times B_w$ forces. The electrons are phase bunched after a period of time. At $t = t_1$, we reverse the phase of the waves. Whether the electrons would be debunched by this reversed-phase wave is the question.

Because of inherent limitations of the Siple transmitter, a 10 ms pulse offset from the main signal at f_o by a few hundred hertz must be inserted in order to achieve a phase change in the main signal. The amount of phase change in the main signal is determined by

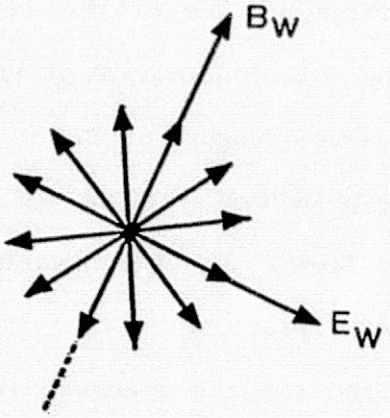

a. Electrons initially are uniformly distributed in phase. There is no net transverse current.

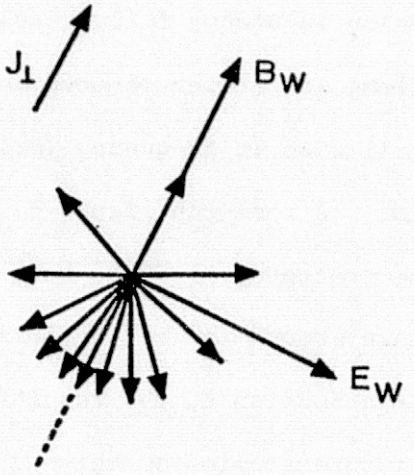

b. After a period of time, electrons are phase-organized to form a transverse current $J_\perp$.

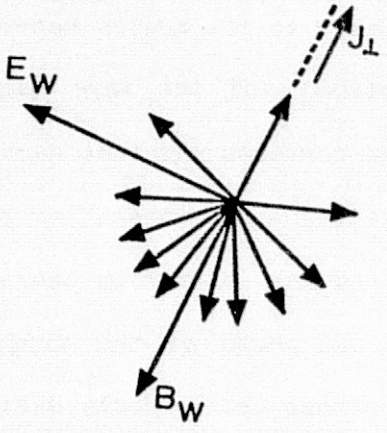

c. The phase of the signal is reversed. The phase-organized electrons may suffer opposite forces and undergo a debunching process.

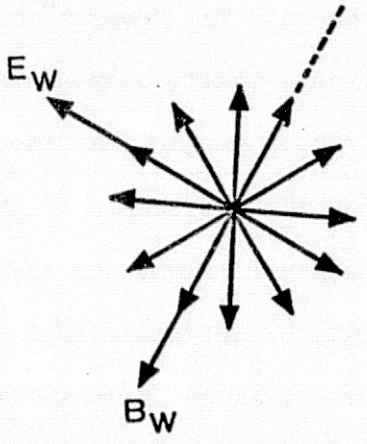

d. After the electrons become randomized in phase, the post-transition signal starts afresh to organize these electrons.

Fig. 3.1. DEMONSTRATION OF THE IDEA OF HOW A PHASE REVERSING SIGNAL AFFECTS THE PHASE-BUNCHED CURRENT. Short arrows represent $v_\perp$'s of the resonant electrons. It is assumed that $v_\perp$ is constant and that electrons initially are in exact resonance with the wave.

$$\Delta\phi_w = 2\pi\Delta f\Delta t \tag{3.1}$$

A schematic illustration of how to achieve a phase change in the main signal is shown in Fig. 3.2. In this experiment, Δt is fixed at 10 ms. Setting Δf to ± 300 and ± 350 Hz gives a phase shift of $\pm 6\pi$ and $\pm 7\pi$, respectively. Thus, the in-phase and the anti-phase conditions are achieved. For simplicity, we shall call the waves in the in-phase condition 0-waves and those in the anti-phase condition π-waves.

At the time the experiment was designed, it was believed that the 10 ms gap would be too short to affect the wave growth processes and that the main effect would come from the phase reversing. The data show just the reverse. The growth rates and the saturation levels of the signals after the interruptions are the same regardless of whether the triggering wave is a π-wave or an 0-wave. In addition, rising emissions often are induced by the gaps. These gap-induced emissions may develop into fully independent rising emissions or they may be either suppressed or entrained by the main signals.

Two examples of the gap-induced emissions are illustrated in Fig. 3.3. Rising emissions are developed from the 10 ms gaps. The frequency and time resolutions of these records are about 20 Hz and 60 msec, respectively. The dynamic spectrums in the two lower panels, showing the same data as the ones on the upper panel, have been expanded in frequency by a factor of 2 and 5, respectively. The two triggering waves at 5 kHz are π-waves. Both last for one second and are interrupted at the 400th msec by a 10 ms gap. The durations of the signals are indicated by the one-second long horizontal bars just above the time scale. The time of interruptions are indicated by the small vertical bars. The delay time of the gap with respect to the beginning of the signal is called τ_d.

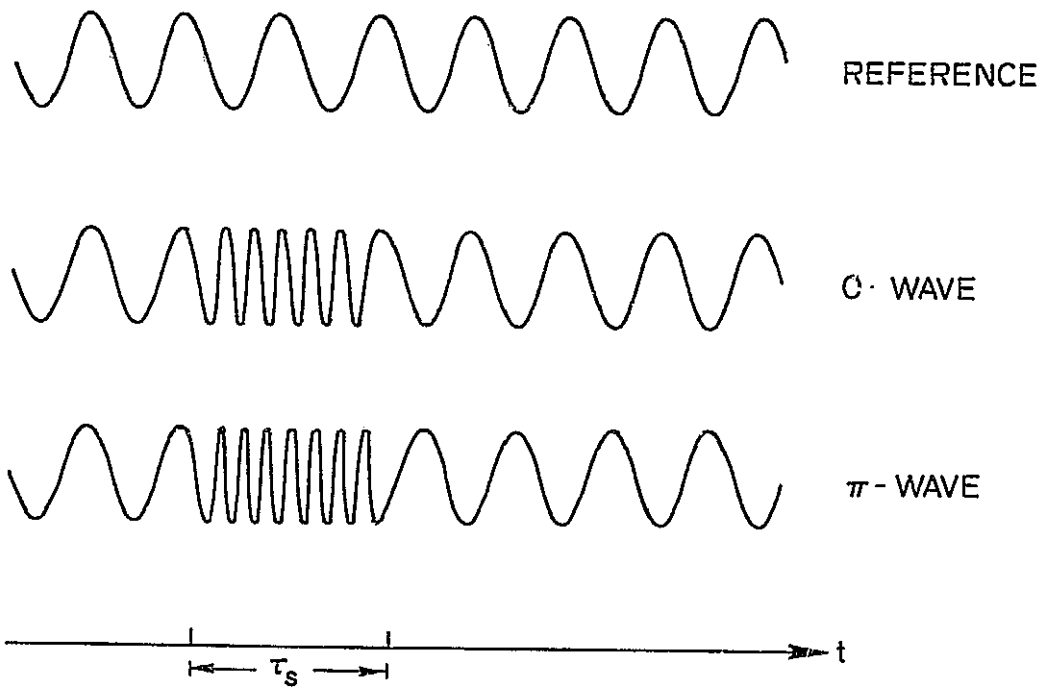

Fig. 3.2. DEMONSTRATION OF HOW A PHASE REVERSAL IS ACHIEVED.

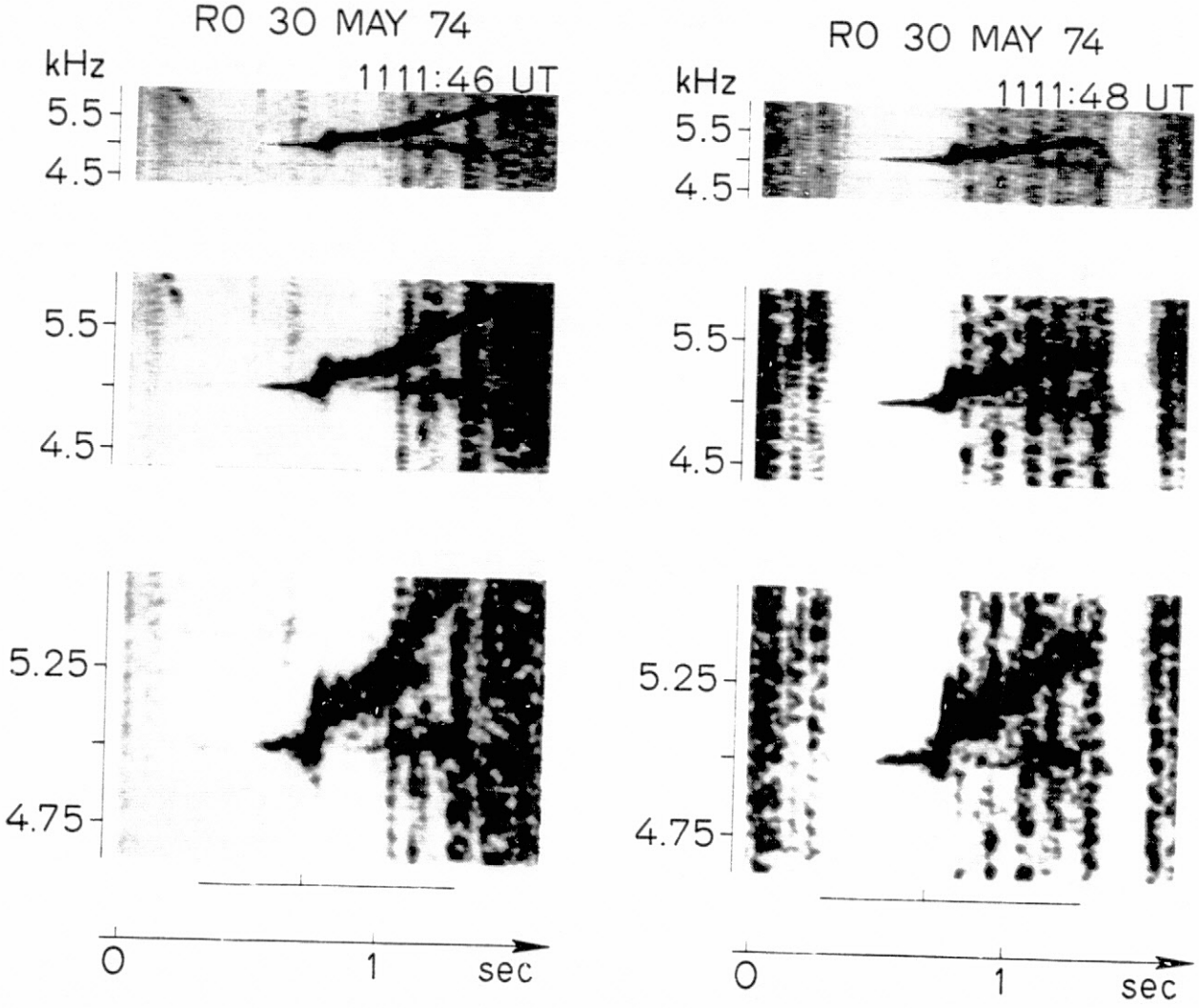

Fig. 3.3. TWO EXAMPLES OF TYPICAL GAP-INDUCED EMISSIONS. The middle and the lower panels contain the same data in the upper panel but are expanded in the frequency scale by factors of two and five, respectively. Both of the one-s triggering signals at 5 kHz are interrupted by a 10 ms gap after 400 msec. The duration of signals are indicated beneath the lower panel by the horizontal bars on which the small vertical bars indicate the time of interruptions. A rising emission with $df/dt \sim 8$ kHz/sec is induced by each interruption. The emissions appear to feed energy to the 85th and/or the 86th PLH's, at 5.1 and 5.16 kHz, respectively, that, in turn, induce rising emissions with $df/dt \sim 1$ kHz/sec.

There were several ducts in the magnetosphere in this period as evidenced by multiple traces of whistlers on the Roberval data (not shown). It is believed that each whistler trace observed on the ground corresponds to a physical duct in the magnetosphere [e.g., Carpenter, 1966; Park, 1970]. Only two whistler traces were observable above 4.8 kHz. The two-hop delays were measured to be ~2.10 and ~2.62 sec at 5 kHz for these two whistlers. Moreover, the second whistler appears to be much intenser in amplitude than the first one. (The L values of these ducts were found by a standard curve-fitting method [e.g., Smith and Carpenter, 1961; Ho and Bernard, 1973] to be at $L = 3.3$ and $L = 3.5$.)

The one-s pulses at 5 kHz were transmitted on the seconds from Siple. The one-hop delay of the signals (referring to the gaps and the ends of the pulses) was measured to be ~1.3 sec, in good agreement with the delay time of the second whistler (at $L \sim 3.5$). Therefore, we conclude that the received signals can be viewed as single-path signals.

The first example shows that a rising emission is developed near the time of the 10 msec gap. The slope of the gap-induced emission is about 8 kHz/sec. As the emission develops, it appears to feed energy to the 85th and 86th power line harmonics (PLH's) at 5.10 and 5.16 kHz, respectively. The PLH's then trigger emissions with $df/dt \approx 1$ kHz/sec. The gap-induced rising emission with $df/dt \approx 8$ kHz/sec is quenched near 5.25 kHz.

The PLH's are believed to be signals radiated by the North American power distribution systems leaking into the magnetosphere [Helliwell et al, 1975].

The second example shows almost the same features of gap-induced emissions as the first example. The gap-induced emission with $df/dt \sim 8$

kHz/sec is quenched near 5.3 kHz. Only one PLH, at 5.1 kHz, has been activated by the gap-induced emission and triggers a rising emission with slope of ~1 kHz/sec. Near the time of triggering, the main signal suddenly decreases in magnitude. As the rising emission drifts away from the main signal, the main signal starts to grow again.

The amplitude behavior of the main signal before and after the gap is illustrated by four more examples, shown in Fig. 3.4. Here, τ_d is 200 or 400 ms, as indicated in the middle panel by a vertical bar below the "0" or "π" symbol.

It has been determined through whistler studies that there were several paths available at that time. The dominant one was at $L \sim 4.6$.

The signal amplitude measured in a narrow-band filter (340 Hz) centered at 4.5 kHz shows an initial growth rate of (75 ± 10) dB/sec in all four examples and a growth time of roughly 250 ms. It is seen that, when $\tau_d = 200$ ms, the gap occurs before saturation while, for $\tau_d = 400$ ms, the gap occurs after saturation. There are very pronounced amplitude drops associated with the gaps in the main signals. The growth rates after the gap are the same as the initial growth rate (within a limit of observation error), regardless of whether the signal is an 0-wave or a π-wave. The 0 and π conditions do not seem to affect either the growth rate or the saturation levels after the gap.

The spectrogram in the upper panel of Fig. 3.4 shows that the emissions triggered by the gaps are not fully developed. They may have been suppressed by the main signal or by some other process. The evidence suggests that emissions are, in fact, suppressed by the main signal.

This suppression effect is demonstrated by the records on Fig. 3.5. The two examples of gap-induced emissions in the middle panel occurred a

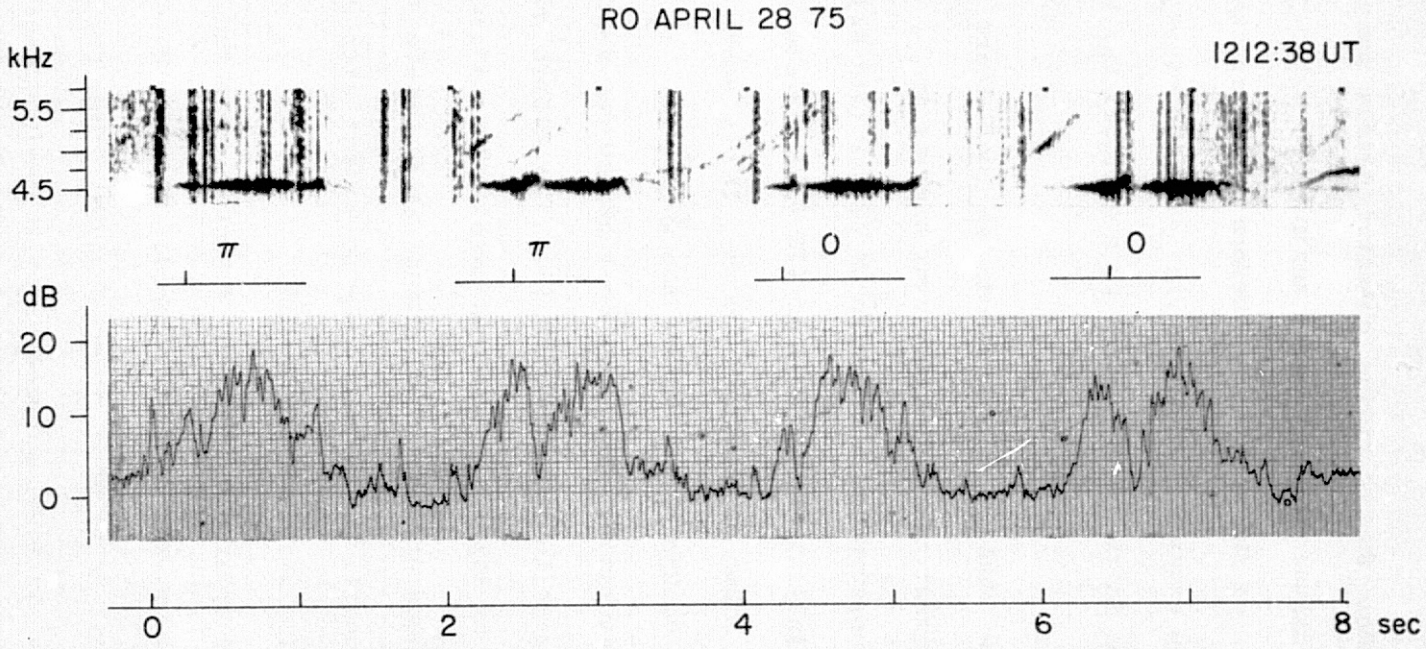

Fig. 3.4. EXAMPLES OF GAP-INDUCED EMISSIONS. Upper panel shows the dynamic spectrum. Lower panel shows amplitude (log scale) measured in a 340 Hz band centered at 4.5 kHz. The interruptions occur at the 200th or 400th msec as indicated by the vertical bars in the middle panel. Shortly after each gap, the amplitude drops approximately to the noise level and then grows again. The initial and post-gap growth rates are almost identical regardless of whether the triggering wave is in an 0- or a π-condition. The saturation level is also independent of the 0 or π condition. The growth time is about 250 msec.

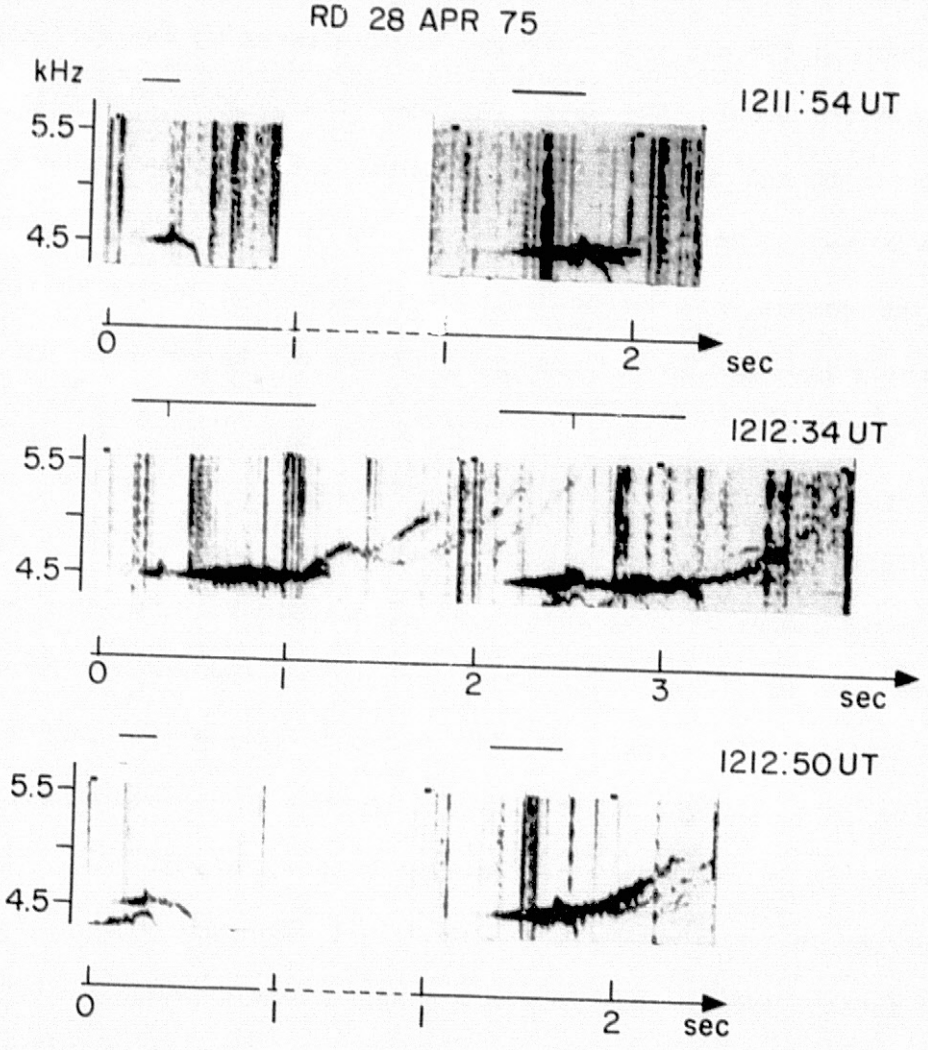

Fig. 3.5. EXAMPLES SHOWING WAVE-WAVE INTERACTIONS BETWEEN GAP-INDUCED EMISSIONS AND THE POST-GAP SIGNALS. The three panels are arranged in chronological order. The calibration waves, shown in the upper and the lower panels, are 200 and 400 msec constant frequency signals. As indicated by the horizontal bars on the tops of the panels, these signals have exactly the same durations as the pre-gap sections of the triggering waves on the middle panel. The calibration waves trigger BLI type emissions followed by falling and/or rising tone emissions, while the pre-gap sections of the gap-triggering signals induce only BLI type emissions. No falling or rising emissions are observed following BLI's, indicating that the emissions are either suppressed or entrained by the post-gap section of the main signal.

few seconds earlier than the ones displayed in Fig. 3.4. Here, τ_d equals 200 and 400 ms, respectively, as indicated by the vertical bars just above the panel. The upper and lower panels show the calibration waves prior to and following the examples shown in the middle panel (within 30 sec). The calibration waves, as indicated by horizontal bars above the panels, are constant frequency pulses of length 200 and 400 ms, exactly the same as the pre-gap sections of the waves in the middle panel.

It is clear that both the 200 and 400 ms calibration waves trigger "band-limited-impulse" (BLI) type emissions [Helliwell, 1978], followed by fully developed falling and/or rising emissions. But the pre-gap sections (200 or 400 ms long) of the gap-triggering waves trigger BLI-type emissions only. There are no fully developed falling or rising emissions following the BLI's, suggesting that the emissions are either suppressed or entrained by the post-gap section of the main signals. Remembering that the post-gap growth rate of the main signals is the same as the initial growth rate in all examples shown in Fig. 3.4, we rule out the possibility of entrainment. Therefore, we conclude that the emissions have been suppressed by the main signals and that the main signal following the gap has not been significantly altered by the emissions in this particular case.

Table 3.1 lists the averaged initial growth rate, post-gap growth rate, and the saturation level over 52 examples taken on April 28 and May 13, 1975. The result shows that the saturation levels are practically the same and that the initial growth rate is identical to the post-gap growth rate, regardless of whether the wave is in a 0- or a π-condition.

Table 3.1

AVERAGED INITIAL GROWTH RATE, POST-GAP GROWTH RATE, AND SATURATION LEVEL OVER 52 EXAMPLES TAKEN ON APRIL 28 AND MAY 13, 1975, FOR BOTH 0-WAVES AND π-WAVES

τ_d	200 ms		400 ms		Average
Wave type	0	π	0	π	
Initial growth rate (dB/s)	79 (26)*	79 (23)	76 (27)	78 (23)	78
Growth rate after gap (dB/s)	74 (27)	78 (26)	74 (30)	77 (23)	76
Saturation** level (dB)	15 (2.8)	14 (3.3)	16 (2.8)	16 (3.2)	15

*(M) indicates the standard deviation.

**Above noise level.

The data on gap-induced emissions show many instances of rising emissions. So far, no fully developed falling emission has been observed within the gap in more than a hundred cases we have studied. This indicates that falling emissions require a longer time to develop. This is understandable since all tail-end falling emissions first show a slight rise before falling [Stiles and Helliwell, 1975]. By the end of the gap, the frequency of the falling emission is still within the range for which interaction between the post-gap signal and the emission can occur. Thus, the falling emissions are suppressed by the post-gap signals.

C. An Interpretation of Gap-Induced Emissions

The key to an explanation of gap-induced emissions is based on the hypotheses that the radiation from the wave-organized electrons can switch from a forced mode to a natural mode at the end of a triggering wave. As the wave propagates through the equatorial interaction region in the magnetosphere, it phase-bunches electrons, producing transverse currents that radiate a new field, causing the wave to grow. The frequency of the new radiation field usually remains within a few hertz of the triggering wave [Stiles and Helliwell, 1975]. The new outgoing radiation organizes incoming electrons, which then radiates new fields again and the process continues. As noted by Helliwell [1978], this "wave-particle system" resembles a resonant circuit driven by signals which may not be at the natural frequency of the circuit. The resonant circuit is in a driven mode or forced mode. When the external signal disappears, the resonant circuit switches to its natural resonance frequency and is then operating in a natural mode.

As a gap-triggering wave arrives at the equator, the gap has changed because of the fact that the wave has been traveling through a highly dispersive medium. Computer simulation results (not shown) indicate that the gap is expanded to 20 to 25 ms for the cases discussed in the previous section.

When the electrons organized by the pre-gap section of a wave cross the gap (this transit requires about 10 ms because their parallel velocity makes the gap appear shorter than the lab frame value of about 20 ms), there are several possible responses for the "wave-particle system." First, when the gap is very small compared to the debunching time, the coherence of the organized electrons tends to be preserved during the gap. Assuming no inhomogeneity in the interaction region, the post-gap section of the wave is able to control these previously bunched electrons if the triggering wave is an 0-wave. The signal then continues to grow when the interruption occurs in the initial growing phase. On the other hand, if the wave is a π-wave, the post-gap section has to reverse the phases of currents, if that can be done, before the wave grows again. We expect to see a systematic difference in growth behavior after the gaps for these two cases.

An electron motion in an 0-wave and that in a π-wave is shown in Figs. 3.6 and 3.7, respectively. On the left of both figures, an electron trajectory in the phase plane $(V_{\parallel},\psi)$ prior to, during, and following the gap is shown in panels (A), (B), and (C), respectively. The corresponding time domain motion is shown on the right. Prior to the gap, the electron is trapped by the wave and executes a pendulum type of motion as indicated by 1, 2, and 3 in both the phase plane and the time domain. During the gap, $V_{\parallel}$ of the electron is constant because

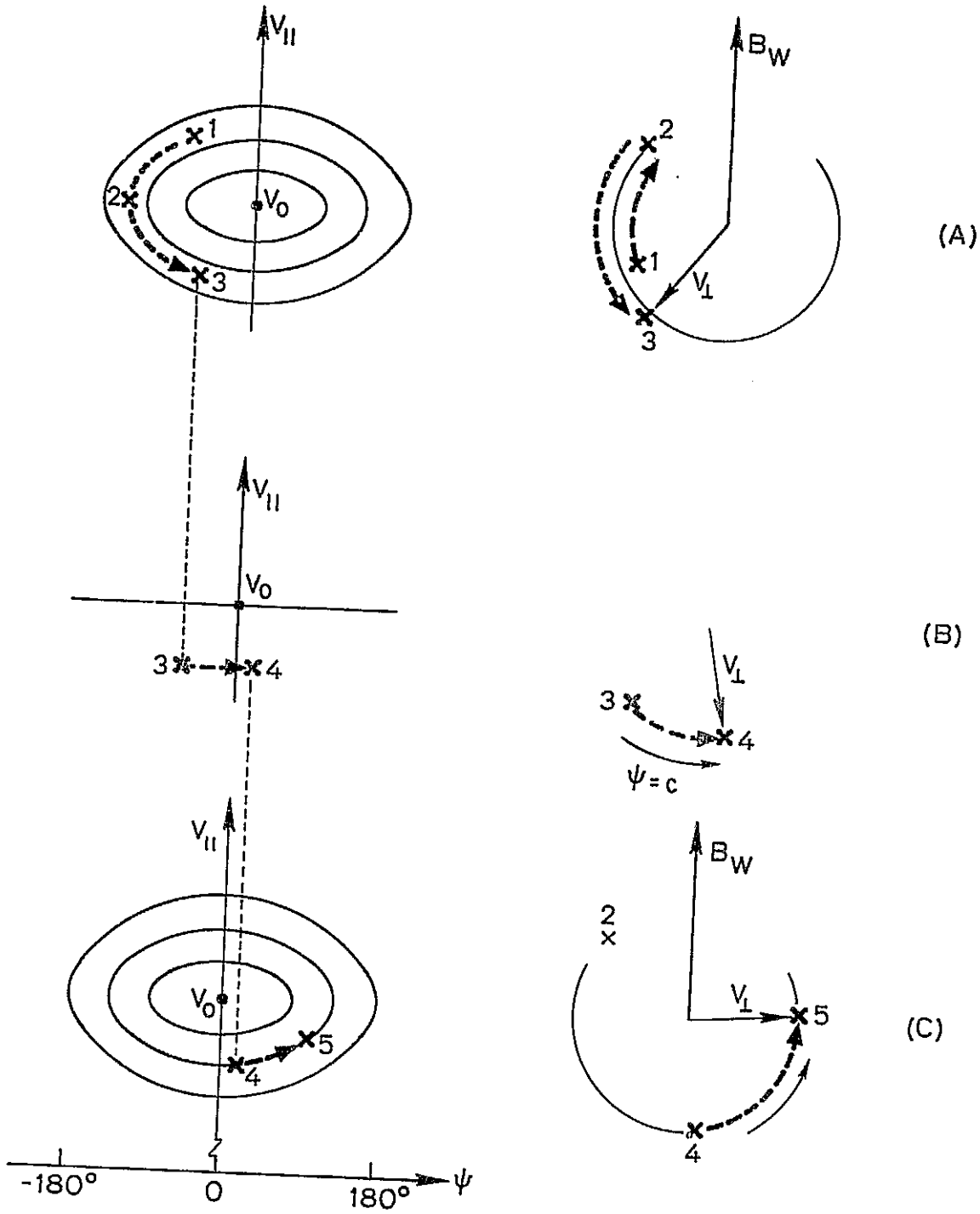

Fig. 3.6. ELECTRON MOTION IN AN O WAVE. (A) Before the gap, (B) during the gap, and (C) after the gap. The electron is still "trapped" after the gap.

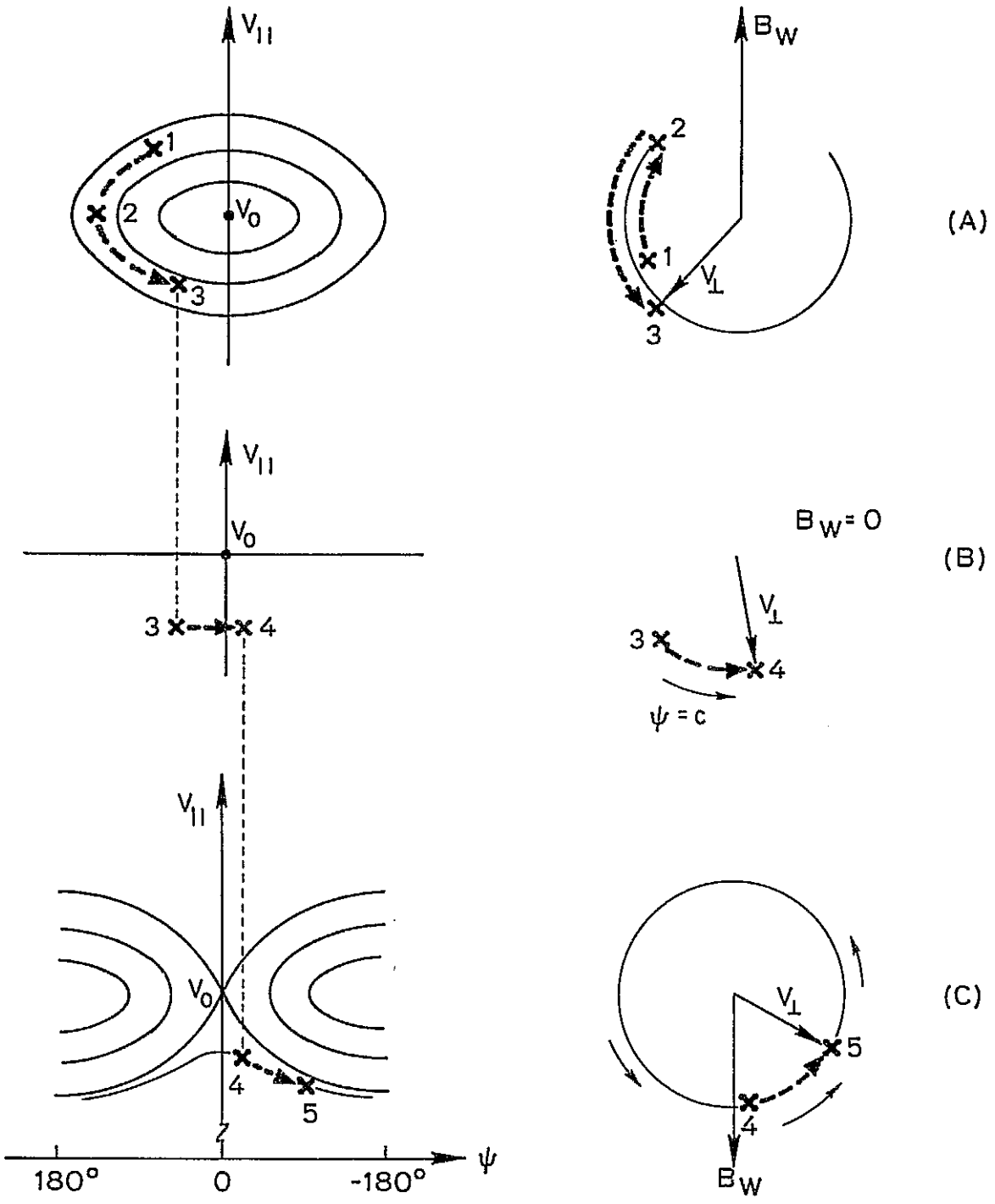

Fig. 3.7. ELECTRON MOTION IN A π WAVE. (A) Before the gap, (B) during the gap, and (C) after the gap. The electron becomes "untrapped" after the gap.

there is no wave that can effectively perturb the electron. The phase angle ψ changes at a constant rate $K(V_o - V_{||})$. In the phase plane, the electron traces a line parallel to ψ-axis while, in the time domain, it rotates with a constant angular rate of $K(V_o - V_{||})/2\pi$ cycles per second. At the end of the gap, the electron reaches Location 4. After the gap, the electron can be trapped in the 0-wave but not in the π-wave. In the 0-wave case, the electron has been shifted to a different contour closer to the origin in the phase plane. The corresponding time domain motion has been changed too. The electron still swings back and forth about the wave field but with less excursion in ψ and with a smaller oscillation period. In the π-wave case, the electron has been moved to an unclosed contour in the phase plane, as shown in Fig. 3.7. It becomes untrapped. In the time domain, the electron rotates about the wave field. Thus, this particular electron remains trapped after the gap for the 0-wave case and becomes untrapped for the π-wave case.

Not all the trapped electrons become untrapped after the gap in a π-wave. Only a portion of them do. Figure 3.8 illustrates the temporal development of the trapping region during the gap. The inhomogeneity forces have been neglected for the time being. Panels (a), (b), and (c) show the cases in which the gap is 0, 10, and 20 msec, respectively. 0-wave and π-wave conditions are indicated by the "0" and "π" symbols. The regions enclosed by the broken lines are the deformed trapping regions developed during the gap. Assuming the wave intensity is the same for both the pre- and the post-gap sections, the trapping regions for the post-gap signal are indicated by the solid lines. The overlap of the deformed and the new trapping regions is shown by the shaded areas in which electrons trapped by the pre-gap signals are trapped again by the

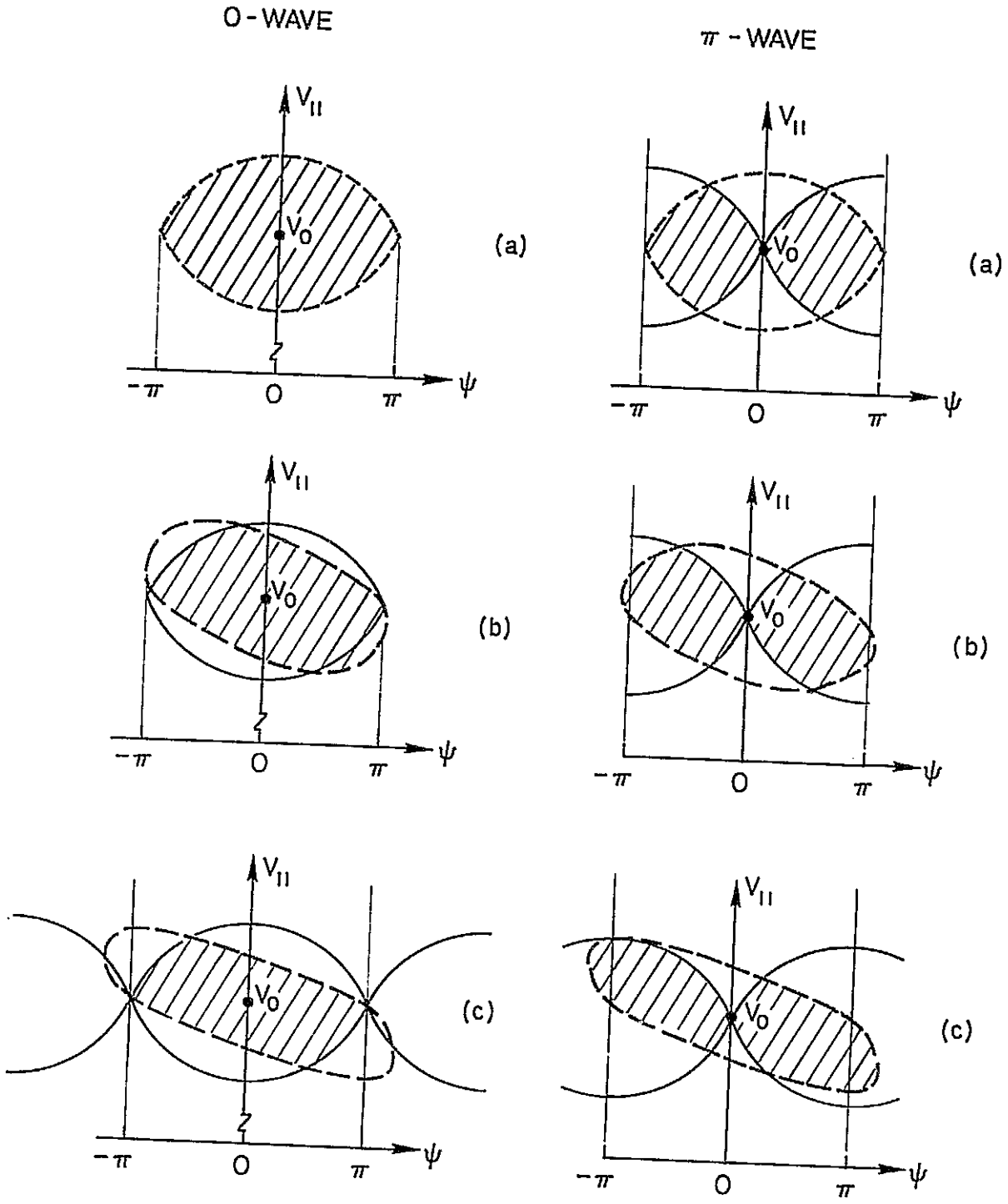

Fig. 3.8. DEFORMATION OF THE TRAPPING DOMAIN DURING THE GAPS. The gap size equals (a) 0 msec, (b) 10 msec, and (c) 20 msec. Electrons in the shaded areas are those which were trapped by the pre-gap section and are still trapped by the post-gap section of the signal. A homogeneous model is used. The corresponding frequency range of the trapping range in $V_{||}$ is assumed to be 50 Hz.

post-gap signals. Those electrons outside the shaded area become untrapped and are assumed to make no contribution to the growth of the post-gap signals. It must be noted that using trapped electrons to calculate the transverse current may only give us a rough estimation. However, by examining how many percent of the trapped electrons have been lost during the gaps, it is possible to determine whether the post-gap wave will take advantage of the previously organized electrons or start afresh to organize a new set of electrons. In this illustration, the wave intensity and particle pitch angle are set up so that the corresponding frequency range of the trapping width in $V_{\parallel}$ equals 50 Hz. It is observed that the 0-wave has more control over the previously organized electrons than the π-wave for a small gap (less than 10 ms).

The inhomogeneity force can be taken into account by a model of a constant external torque, as discussed in Appendix B. This torque deforms the trapping range, reducing the size of the range and moving the stable point $\psi = 0$ to other values of ψ. In addition, the $V_{\parallel}$ changes during the gap because of the adiabatic force. We have used a simple model for the inhomogeneity by considering a constant $V_{\parallel}$ change during the gap for all the trapped electrons, neglecting the deformation effects introduced by the external torque. But the deformation by the differential ψ-drift due to $V_{\parallel}$ spreading is included. The result is shown in Fig. 3.9. The trapping width in $V_{\parallel}$ is chosen so that the corresponding range in frequency is 50 Hz. The inhomogeneity has changed the electron $V_{\parallel}$'s. Using typical parameters at $L = 4$ and assuming electron pitch angle at 30°, we can obtain a $V_{\parallel}$ change that corresponds to a 15 Hz change in frequency at a distance 500 km away from the equator within 5 msec. It is clear that about 50 percent of the trapped "area" becomes "untrapped"

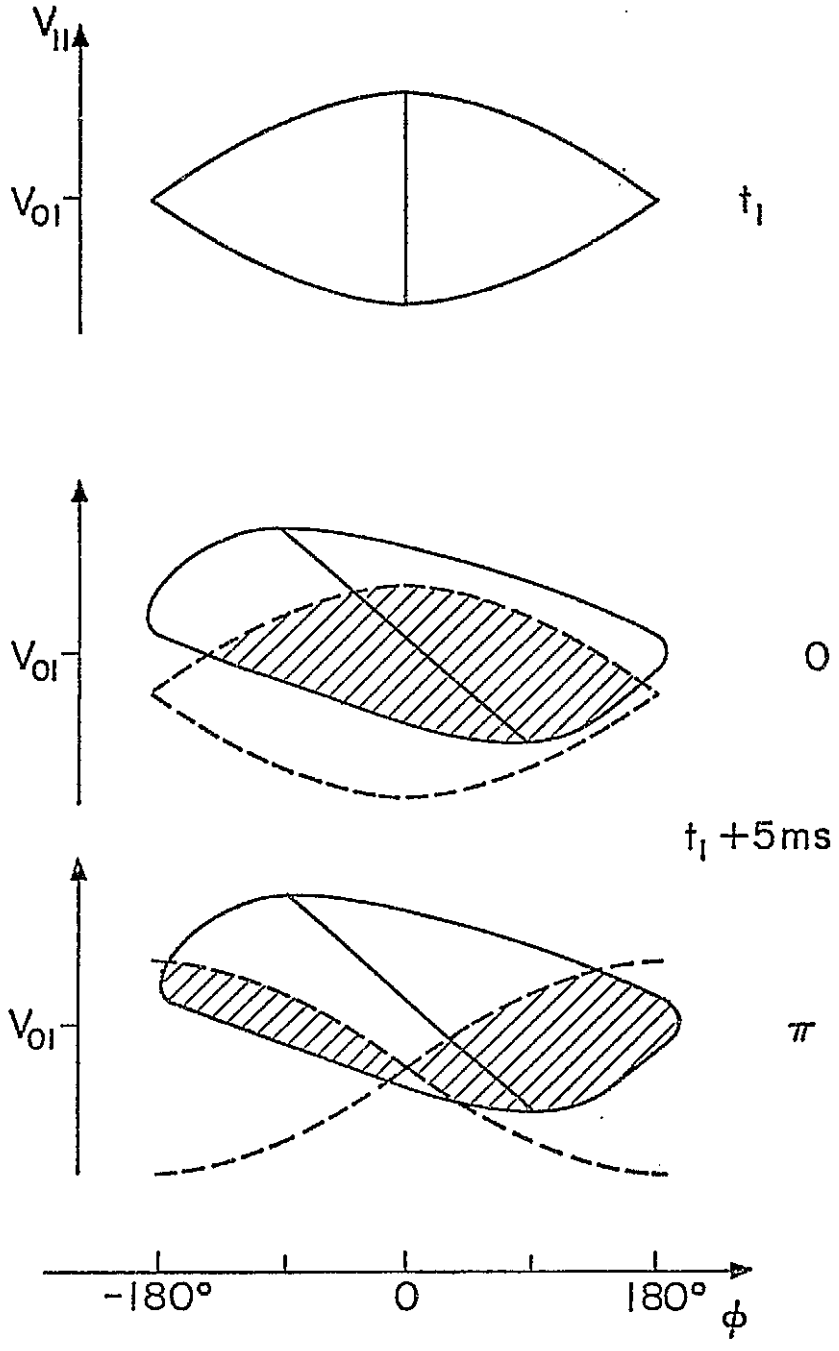

Fig. 3.9. DEFORMATION OF THE TRAPPING DOMAIN DURING A 10 msec GAP IN AN INHOMOGENEOUS MODEL. The transit time of an electron to cross the gap requires about 5 ms because the electron and the wave travel in opposite directions.

after the 10 ms gap for both the 0- and π-waves. If the deformation due to the inhomogeneity were included, the percentage of electrons becoming untrapped after the gap would have been larger than 50 percent, even for a gap as small as 10 ms. Therefore, we expect no significant difference in the growth after the gap between 0- and π-waves unless the gap is much smaller than 10 ms.

As noted in Chapter II, even an instantaneous phase alteration on a sinusoidal signal introduced on the ground will develop into an amplitude gap on the order of 10 ms or more when the signal arrives at the equator. Hence, we shall not see a significant difference in the post-gap growth between 0- and π-waves. In the future phase alteration experiments, an equalizer is needed to pre-process the injected signals so that, when they arrive at the equatorial interaction region, the phase appears to change instantaneously. Under this circumstance, the post-gap growth of the π-wave and that of the 0-wave should be different.

The second possible response of the "wave-particle system" is when the gap is larger than the debunching time and the phase-bunched currents are not strong enough to maintain a self-sustaining emission. In this situation, the coherence of the organized electrons may be destroyed by the debunching processes. Therefore, the coherent radiation from the organized electrons will be quenched. As the post-gap section of a triggering wave enters the interaction region, the bunching process must start afresh. The 0 and π conditions will be immaterial.

The third possibility is that the phase-bunched current is large enough to maintain a self-sustaining emission. The radiation from the bunched electrons switches from the forced mode to a natural mode of the system and changes the radiation frequencies accordingly. The radiation

frequencies of the organized electrons are shifted from the main signal frequency at a rate corresponding to the local inhomogeneity. After the gap, there are two signals: an emission and the main signal. When the frequency difference between the two signals is large, they behave independently and the emission can become fully developed. At the same time, the main signal organizes its own electrons from the beginning, regardless of whether the signal is an 0-wave or a π-wave. On the other hand, when the frequency difference is small, the emission may interact with the main signal. In this situation, the emission may be entrained or suppressed by the main wave. The emission may also suppress growth of the main signal.

The data discussed in Section B show that a 10 ms in a triggering wave can induce emissions in favor of the third possibility. The remaining questions are:

(1) What are the criteria for a self-excited oscillation in the wave-particle system?

(2) How long does it take for radiation from this oscillating system to switch from a forced mode to a natural mode at the end of an external wave?

(3) For two waves to interact, are there conditions between the relative phase, wave frequencies, and wave amplitudes to produce different effects such as entrainments and suppressions?

These questions have not yet been answered satisfactorily. However, the gap triggering data and related experiments do give us some insights on the questions.

It should be recalled that short individual pulses (< 50 ms) do not usually trigger emissions, while the long pulses (> 100 ms) do [Helliwell, 1965; Stiles and Helliwell, 1977; Helliwell and Katsufrakis, 1974; McPherson et al, 1974]. This suggests that the wave amplitudes must grow beyond a threshold level in order to generate self-sustaining emissions. The question of how the threshold levels depend on input wave intensities is still under investigation.

In a simple lumped resonant circuit, the oscillation switches from the forced mode to a natural mode "instantaneously" when the external excitation is removed. On the other hand, the wave particle system in the magnetosphere may not be able to switch from a forced mode to a natural mode instantly. One of the reasons is the dispersion distortion on the ends of signals. A VLF pulse may appear to have a "tail" when arriving at the interaction region near the equator. The "end" is not a sudden termination. Since a 10 ms gap in the triggering wave can induce emissions, we conclude that the radiations from the organized electrons can switch from a forced mode to a natural mode in less than 10 ms.

After the gap, the main signal and the triggered emission interact with incoming electrons at the same time. If the frequency difference is large, these two signals will organize their own groups of electrons independently. They do not interact with one another. On the other hand, if the frequency difference is small, interaction between the gap-induced emission and the post-gap signal may occur.

The detailed mechanisms of this kind of WWI are not yet clearly understood. It is, however, believed that both the inhomogeneity of the geomagnetic field and the overlap of the coherence bandwidth (see the next chapter) are responsible. In the next chapter, we shall show that

two forced-mode signals with frequency difference less than 50 Hz tend to interact with each other. Coupling, suppression, and entrainment are often observed in such signals. The interaction is attributed mainly to the overlap of perturbed $V_{\parallel}$ ranges in the electron distribution function [Chang and Helliwell, 1977]. Electrons in the range of overlap carry energy between these signals. The same mechanism may happen in FNWWI. This hypothesis needs further investigation. On the other hand, Helliwell [private communication, 1978] suggests that the inhomogeneity is the main source of wave couplings.

As to the question of whether the frequency slopes and the relative phase between two interacting waves are important to the processes of entrainment, suppression, or coupling, the available gap-triggering data are not able to provide a proper answer. More refined, controlled experiments or computer simulations are required to solve this problem. One of the refined experiments, Gap Triggering Experiment, will be discussed in the next section.

In summary, the phenomenon of gap-induced emissions is explained by the hypothesis that radiation from the "wave-particle system" switch from the forced-mode to a natural mode at the end of a triggering wave. Natural mode emissions are developed in a 10 ms gap. The wave intensity is strong enough to maintain a self-sustaining emission. The frequency of the emission during the gap changes according to the local inhomogeneity in the interaction region. The frequency difference between the emission and the post-gap section of the main signal may be large after the gap. The emission may then have developed into an independent rising or falling tone, and the post-gap section of the main signal starts afresh in organizing new sets of electrons. The 0- and π-condition is immaterial

as far as the growth of the post-gap section of the signal is concerned. On the other hand, when the frequency difference is small, interaction between the gap-induced emission and the post-gap signal occurs. The frequency difference between the emission and the main signal after the gap is the main criterion in determining whether mutual interactions occur or not.

D. GATR Transmitter Program

The gap-triggering data show many instances of inducing rising emissions from the 10 ms gaps. So far, no fully-developed falling emission has been observed within the gap, indicating falling emissions require a larger gap to develop. It is believed that a fully developed falling emission might have been observed, had the triggering signal had a larger gap. It is therefore beneficial to increase the length of the gap to determine the critical length beyond which a fully-developed falling emission can occur. We expect that waves with gaps less than the critical size will produce WWI's. This program also provides an opportunity to actually "scan" the development of falling emissions. These are the reasons for designing the so-called GAP-TRIGGERING (GATR) PROGRAM.

In all the examples shown in Fig. 3.10, the 750 msec triggering waves are interrupted by a gap at the 250th msec. The gap size, T_g, has five different values: 10, 40, 70, 100, and 130 msec, and all the waves are in the 0-condition (no phase reversal). The carrier frequency is 3.85 kHz. From the multiple traces of the ramps appearing on the records (not shown), it is found that there were two dominant paths at this period. They were very close to each other. The difference of the time delay for these two paths at 3.85 kHz is about 50 ± 10 ms (refering to the centers of the traces).

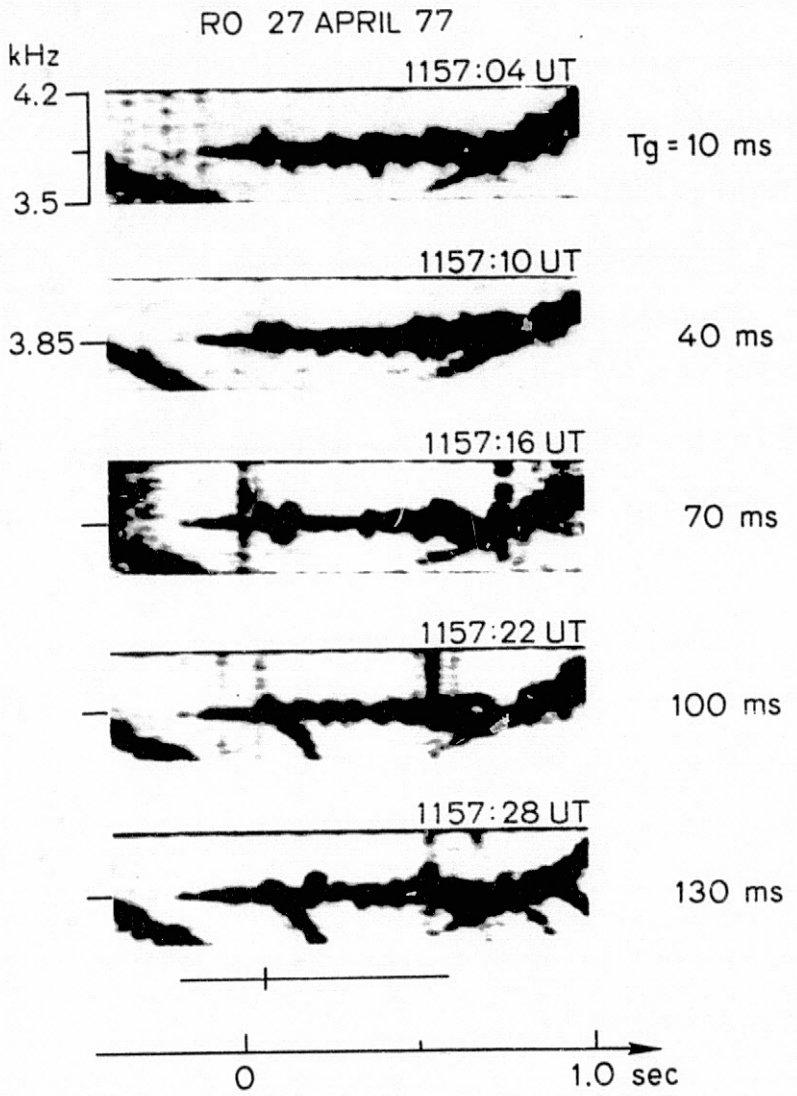

Fig. 3.10. THE FEATURES OF GAP-INDUCED EMISSIONS VS VARIOUS GAP SIZES.

It is observed that, as the gap T_g increases from 10 to 70 ms, all the gap-induced emissions are either suppressed or entrained by the post-gap signals. When T_g is 100 ms or more, a fully-developed falling emission is observed from one of the two paths. On the other path, path 2, even when the gap becomes as large as 130 ms, the emission can still be "captured" by the post-gap section of the main wave. This is because the slope df/dt of the emission is small on path 2. After the 130 ms gap, the frequency difference between the emission and the post-gap signal is small enough to permit the WWI to occur. This "capture" feature can also be seen for the signal on path 1. When the gap equals 70 ms, the gap-induced falling emission has been developed. It rises in frequency initially and then turns around in frequency as a typical tail-end falling emission. At the end of the gap, the emission frequency is 90 ± 10 Hz less than that of the main signal. The post-gap signal "captures" the falling emission, causing the emission to overshoot toward the positive frequency direction. This "capture" feature of WWI is identified for the first time through this program.

Explanations of this "capture" feature of WWI are still being investigated. It may be an important clue to understanding the mechanisms of WWI in the magnetosphere.

E. Summary and Recommendations

We have found that a 10 ms gap in a triggering wave can induce emissions. The relative phase between the pre- and post-gap sections is immaterial as far as the growth processes of the post-gap sections are concerned. A qualitative explanation has been found by postulating that the radiation from the organized electrons can switch from a forced-mode

to a natural mode at the end of a wave train. The 0- and π-conditions are not important to the growth of post-gap sections of signals. On most occasions, the gap-induced emissions interact with the post-gap signals. This wave-wave interaction involves one natural mode emission and a forced-mode signal and is termed force mode/natural mode wave-wave interaction (FNWWI). For cases shown in Figs. 3.4 and 3.5, we have shown that the growth of the post-gap signal seems not to be affected, at least not noticeably, and that the development of the natural emission is quenched by this interaction, regardless of whether the wave is in an 0- or a π-condition.

A refined transmitter program based on the observations of the gap-induced emissions has been designed to actually "scan" the development of triggered emissions. One of the results confirms an earlier observation that triggered emissions always start with a small rise in frequency. It has also been found that falling emissions with a negative frequency offset as large as 90 Hz from the triggering wave can still be "captured" by the post-gap signal. This is the first time the "capture" feature of FNWWI have been identified. This refined transmitter program can produce FNWWI's in a somewhat predictable way. For small gaps, suppressions are usually observed. For large gaps ($\geq$100 ms), falling emissions can be fully developed. For medium size gaps (~70 ms), one form of entrainment, the "capture" feature, is often observed. It seems feasible to use this program to generate various features of FNWWI's. A refined version could be employed to investigate the importance of the relative phase, the frequency difference, and the slope df/dt of the emission in a FNWWI by controlling the phase and the frequency of the post-gap section of the triggering wave.

Phase distortion due to propagation in a duct from the transmitter site to the interaction region increases the size of the gap and changes its shape as well. A pre-processing device, an equalizer, is required to compensate for the distortion so that, when the signal arrives at the interaction region, it has the correct form. For the experiments designed to study how a phase alternation (without a gap) in a triggering wave can affect the growth of the forced-mode signal, this device is required.

Chapter IV

SIDEBAND TRIGGERING

A. Introduction

In this chapter, we shall discuss another kind of wave-wave interaction (WWI): sideband mutual interaction (SMI). It was discovered unexpectedly during a wave injection experiment for studies on the relation of signal growth to phase reversals in triggering signals. The triggering signal can also be categorized as an 0-wave or a π-wave, as before. The rationale for this kind of wave injection experiments has been discussed in the preceding chapter. In this particular experiment, which will be described in detail in Section B, the phase of a one-second signal is altered regularly at periods that are multiples of 10 msec. At the time of designing the experiment, we did not consider the discrete sidebands at various frequencies that were generated by the regular phase modulation of the signals. We were expecting to see systematic differences between the growth of 0-waves and that of π-waves. The data show that 0- and π-conditions are immaterial to wave growth and triggering. Furthermore, the period of phase modulation in the signal appears to be closely related to the occurrence of triggered emissions. The longer the period, the less the occurrence of triggered emissions when the period is less than $100 \sim 200$ msec. Signals with modulation periods longer than 200 ms trigger emissions similar to those triggered by one-second pulses. These observations lead to the discovery of sideband triggering.

In Section C, we shall discuss how the length of the interaction region can be estimated from our observations. This estimation is a measure of electron "memory time" which is assumed to be the same as

the transit time for electrons to pass through the interaction region.

In Section D, we shall show that the emissions triggered by individual sideband components are similar to those triggered by constant frequency signals. This phase modulation technique results in the injection of multiple waves (sidebands) into the magnetosphere. The frequency spacing between these sidebands have been changed by varying the modulation period. Therefore, this experiment becomes the first controlled experiment on SMI in the magnetosphere. We shall also show two features of energy coupling between two sidebands at different frequencies.

In Section E, we shall discuss the mechanisms of WWI in both time and frequency domains. Then, a simple model of coherence bandwidth is used to estimate the wave intensity in the interaction region.

In Section F, we shall show results from a new transmitter program which was developed recently based on the studies of the first experiment on SMI. We shall show that, for most cases, the coherence bandwidth is about 50 Hz. The corresponding wave intensity in the interaction region is about $2.5 \sim 10$ mγ, in reasonable agreement with satellite measurements [Heyborne, 1966; Burtis, 1974; Inan et al, 1977]. More examples related to the coherence bandwidth from various transmitter programs are shown in Appendix D.

The conclusions are presented in Section G.

B. A Transmitter Program for Generation of Sidebands

The special transmitter program described below exhibits several features, including phase shifts, shifts in frequency, and variations in pulse length. The phase shift of a signal at a given frequency is

accomplished by shifting the frequency by Δf for an interval τ_s. The phase shift $\Delta\phi_w$ equals $2\pi\Delta f\tau_s$. In this experiment, Δf ranges between 100 to 150 Hz and τ_s ranges from the minimum achievable length 10 to 100 msec. The phase is shifted at a regular interval of $2\tau_s$ at a given frequency. Figure 4.1 schematically shows part of the waveform and a frequency-time (f-t) display of a one-s wave with τ_s = 10 msec.

The total program lasts for 30 seconds. It consists of 30 one-s waves which are grouped into five sets according to the value of τ_s. τ_s has the values of 10, 20, 30, 50, and 100 msec. Figure 4.2 illustrates two of the five sets with τ_s = 50 and 100 msec. Each set has six waves which alternate between two frequency bands separated by 500 Hz. The 500 Hz separation applies to the lower frequency of the upper band and the upper frequency of the lower band. Hence, the offset frequencies Δf are positive in the upper band and negative in the lower band. In each set, $|\Delta f|$ exhibits three different values: 0, 100, and 150 Hz, except when τ_s = 20 and 100 msec. In these cases, $|\Delta f|$ are 0, 100, and 125 Hz. When Δf = 0 Hz, the signal is a one-s constant frequency wave and is called the calibration wave or C-wave. When Δf = 100 Hz, the 0-wave or in-phase condition is produced and, when Δf = 125 or 150 Hz, the π-wave or antiphase condition is achieved. The transmission sequence for the upper frequency band in a set is 0-, C-, and then π-wave. For the lower frequency band, it is π-, 0-, and C-wave. There are five identical C-waves, plus five 0- and five π-waves for various combinations of Δf and τ_s in each frequency band for one cycle of the program. We shall call these one-s waves FSK waves.

Table 4.1 lists the phase changes between successive pulses in a carrier of all the FSK waves in the program. The 0-wave, π-wave, and C-wave conditions depend on the proper choice of τ_s and Δf.

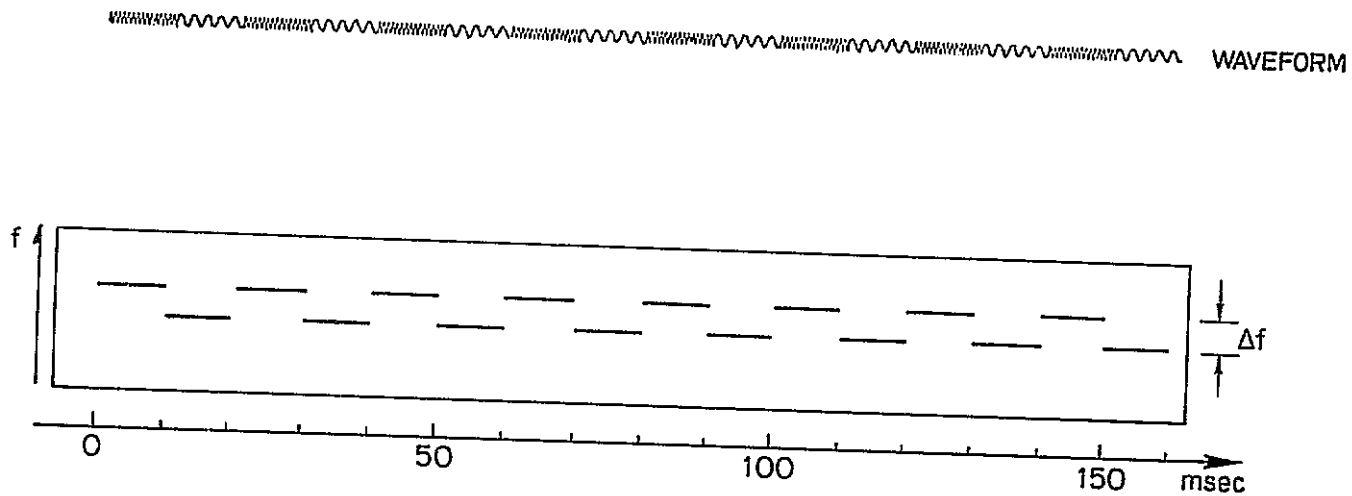

Fig. 4.1. WAVEFORM AND f-t DISPLAY OF AN FSK SIGNAL. τ_s is the length of the sine wave segment.

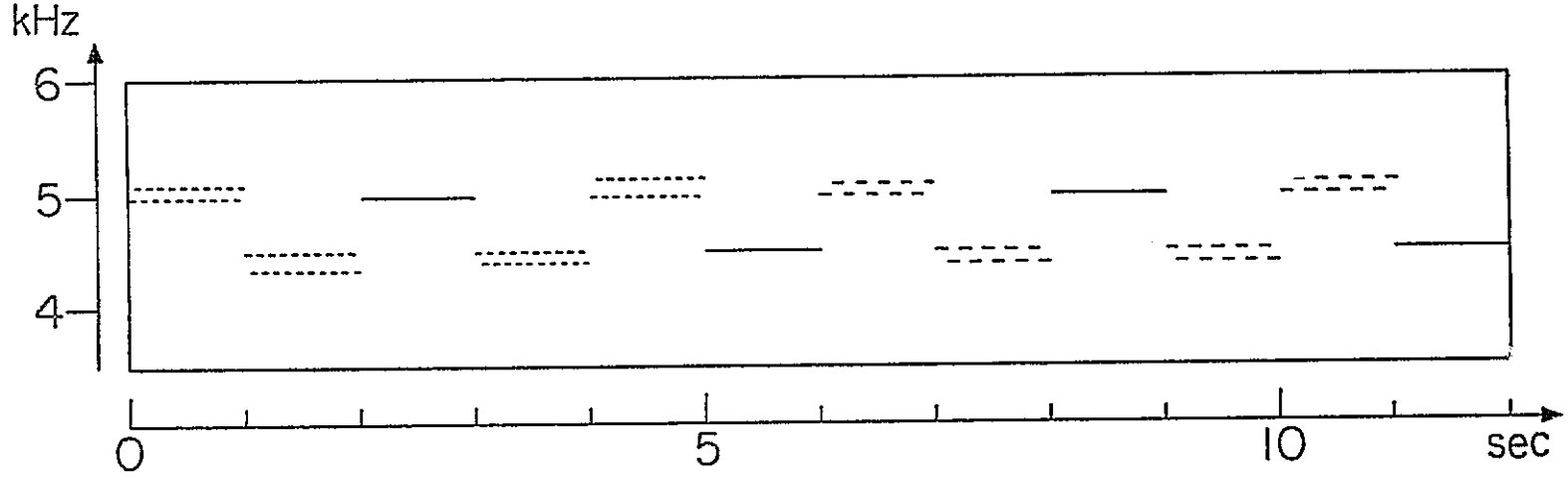

Fig. 4.2. PART OF THE TRANSMITTER PROGRAM DESCRIBED IN SECTION B.

C-2

Table 4.1

THE RELATIVE PHASE BETWEEN SUCCESSIVE PULSES AT A PARTICULAR CARRIER FREQUENCY FOR VARIOUS FSK WAVES

Δf (Hz) / τ_s (ms)	0 Hz	100 Hz	125 Hz	150 Hz
10 ms	0	2π	---	3π
20 ms	0	4π	5π	---
30 ms	0	6π	---	9π
50 ms	0	10π	---	15π
100 ms	0	20π	25π	---
Types of waves	C wave	0 wave	π wave	

There are other versions of the program based on the same principles with slight changes in the sequence as well as of the values of Δf and τ_s. In this report, those cases in which $2\pi\Delta f\tau_s$ equals a multiple of π radians will be discussed. Other versions of the program will not be presented here. Whenever examples are illustrated, the values of Δf and τ_s will be indicated.

A one-s FSK wave can be decomposed into its Fourier components which are discrete "spikes" in the frequency domain. The bandwidth of the spikes is about 1 Hz. In the time domain, each spike corresponds to a sine wave. Thus, a FSK wave can be viewed as the sum of many sine waves at various frequencies, phases, and amplitudes. All the sine waves last one second. The reason why the sidebands last as long as the FSK wave continues and the detailed derivation of the sidebands of FSK waves are discussed in Appendix C.

In f-t space, an FSK wave could be represented either as segments of sine waves alternating between two frequencies at regular intervals for one second or as several one-second long sine waves with proper amplitudes, frequencies, and phases. These two representations are schematically illustrated in Fig. 4.3. It is interesting to note that the same waveform can be represented by two different displays in f-t space. This is because "frequency" and "time" are not independent quantities. The information contained in a "point" in the time domain is spread out on every point in the frequency domain. To obtain precise and complete information for a single point in the time domain, we must have information over the entire frequency domain and vice versa.

But, in practical data processing, we are not willing to wait an infinitely long time in order to obtain precise information on frequency.

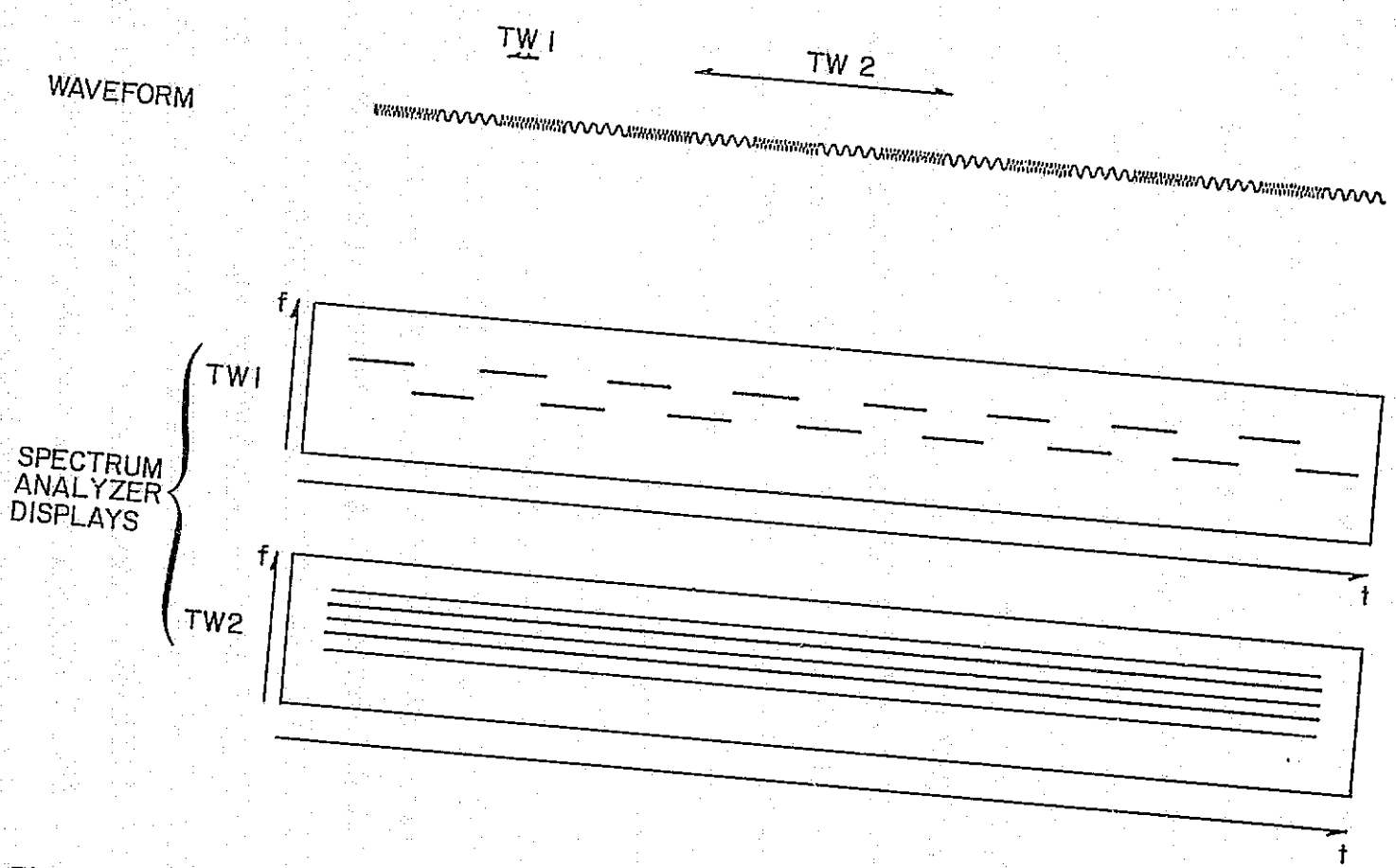

Fig. 4.3. TWO DIFFERENT f-t DISPLAYS OF AN FSK SIGNAL. The segment feature is resolved by a small time window, TW1. Sideband feature becomes observable when a large time window, TW2, is applied.

Thus, we chop off a set of data in the time domain and estimate the frequency components within the time period TW. There is definitely an uncertainty of the estimated frequencies. It has been shown [e.g., Blackman and Tukey, 1958] that, roughly speaking, the product of the uncertainty in frequency Δf and in time Δt must be greater than unity.

Considering $h \triangleq \Delta f \Delta t$ as a basic cell in f-t space where $h \geq 1$, we still have a choice of either Δf or Δt in practical data processing devices. There are no "points" but "cells" in f-t space. The "shape" of the "cell" can be arbitrary so long as the "area" of the "cell" is conserved. Choosing a long Δt corresponds to choosing high frequency resolution (small Δf), while a short Δt provides good time resolution but with a large uncertainty in frequency.

In analyzing the FSK waves, we can resolve the pulses by making the time window (TW), the length of data which are processed in a single scan, shorter than the individual pulse τ_s. On the other hand, we can resolve the sidebands of the FSK waves by setting $TW \geq 4\tau_s$. A data processor, which can "print" the estimated information in f-t space, estimates the intensities of the frequency components of the signals within the time window and "prints" the information on a vertical line specifying an instant in the time domain. This "instant" is somewhat arbitrary within the period of TW. In many data processors, the location of the line is set to represent the instant at the "center of gravity" of a weighted time window. The uncertainty in the time domain can be specified by the "second moment" of this window and definitely depends on the choice of TW. After the processor has finished the first scan, it slides its time window to a new segment for the next scan. The estimated information is "printed" on another line corresponding to another instant.

The process continues for the third scans, fourth scans, and so on. Usually, an appreciable portion of the data in successive scans are overlapped. It is important to point out that the sliding "distance" in the time scale between successive scans may be much smaller than the time window. But, a smaller sliding distance in the time scale does not imply a better time resolution.

As illustrated in Fig. 4.3, the processor sees single frequency signals except at the edges of the segments when TW1 is chosen. The signals are resolved as consisting of square waves alternating at two carrier frequencies. When TW2 is chosen, the processor resolves several spikes in frequency in each scan. Therefore, the resolved signals consist of several horizontal lines representing sinusoidal waves at various frequencies. Thus, depending on the length of the time window, the processor shows either segments of sine waves or continuous sidebands.

An important question is raised: Do the energetic electrons that interact with the FSK wave in the magnetosphere see the wave as segments of sine waves or continuous sidebands? An answer is given in the next section. It has led us to develop a method of remotely estimating the length of the interaction region in the magnetosphere.

C. Estimation of the Length of the Interaction Region in the Magnetosphere

In the magnetosphere, the interaction between a WM wave and the energetic electrons resonant with it is thought to take place within a limited region, usually around the equator. When electrons move away from this region, the inhomogeneity in the geomagnetic field destroys

the resonance between the electrons and the WM wave, and there will be no average energy exchange between the WM wave and the electrons. Since there is no "clear-cut" type of boundary separating the region in which interaction occurs from where there is no interaction, there must be an essential arbitrariness about every definition of the length of the interaction region (IR). For example, Helliwell [1967] defined an interaction region as the region over which the unperturbed phase angle between the WM wave and a resonant electron remains within $\pm\pi$. Inan [1977] defines an interaction region as the distance between the equator to the point where the perturbed phase angle between the wave and an electron becomes π-radian and shows that the length of the interaction region not only depends on the wave intensity, the electron pitch angle, but is also closely related to the initial phase angle between the electron and the wave. For a small wave amplitude, these two definitions differ by a factor of two. These two definitions refer to the region within which electrons are scattered effectively. Whether the VLF wave that interacts with the electrons is amplified or not depends on the details of the electron distribution in the IR [Nunn, 1974; Dysthe, 1971]. An IR defined in these ways may then be categorized as a particle interaction region (PIR), suggested by Helliwell [1978].

It is believed that waves are amplified in the interaction region. There must be spatial variation of the wave intensity from one end of the IR to the other end in the steady state. Another definition of IR can then be stated as the region between the location where the wave intensity starts to increase spatially and to the location where the wave intensity becomes uniform spatially. The length of the IR defined in this way can be measured by satellites moving along a duct in the

magnetosphere. This IR is categorized as a wave interaction region (WIR) [Helliwell, 1978].

The length of the IR we shall discuss in this section is characterized by the averaged memory time of the resonant electrons. It must be related to Inan's definition of IR, that is, characterized by the time that the electrons remain trapped by the wave. The method is to find the critical pulse length, τ_{sc}, of the FSK waves. For the FSK wave with τ_s less than τ_{sc}, the electrons can resolve the sidebands of the waves. For a wave with τ_s greater than τ_{sc}, the electrons can only resolve pulses of the FSK wave. Therefore, τ_{sc} must be related to the electron's memory time. This effect provides a basis for measuring the average electron's memory time in VLF wave-particle interactions in the magnetosphere. By assuming that electrons can remember only the wave that they have encountered during the interaction, the length of the IR has been estimated.

Figure 4.4 shows the histogram obtained by counting the number of the FSK waves which trigger emissions vs the values of τ_s of the waves from the data between 1500 to 1525 UT on 11 October 1974. The program described in Section B was transmitted during this period. The abscissa indicates the values of τ_s and the ordinate shows the number of the FSK waves which trigger emissions. Therefore, the vertical axis could be thought of as indicating wave triggering ability. The 0- and π-wave conditions are also indicated. The C-waves show up five times more frequently than any other waves in the transmitter program. The number of the C-waves that trigger emissions has been divided by five in the histogram.

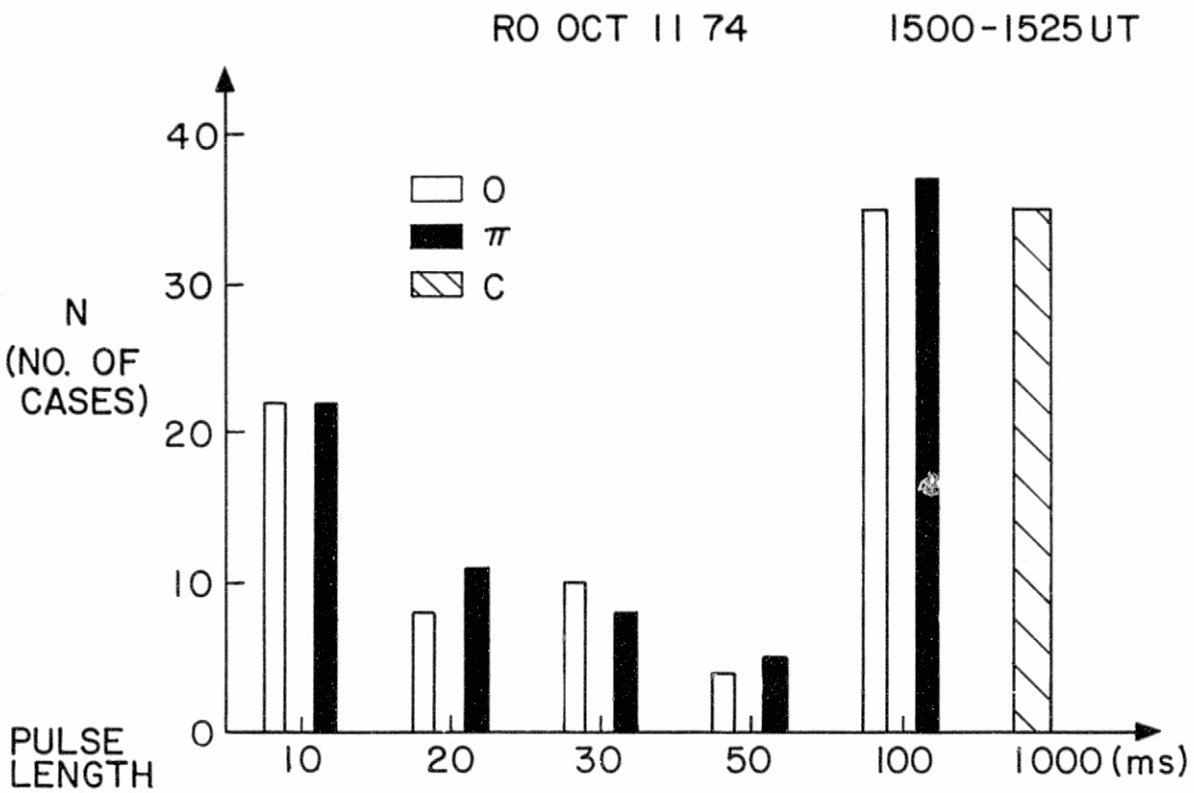

Fig. 4.4. HISTOGRAM OF THE NUMBER OF THE FSK WAVES THAT TRIGGER EMISSIONS VS THE VALUES OF τ_s. The number of C-waves has been divided by five.

The histogram shows that whether the FSK wave is in 0- or π-condition is immaterial to its triggering ability. The parameter on which the wave triggering ability depends is the pulse length τ_s. The waves with τ_s = 100 msec, the longest pulse length among the five sets, show an emission triggering ability as high as that of C-waves and are much higher than the others. Among the other four groups of FSK waves with τ_s = 10, 20, 30, and 50 ms, the triggering ability decreases as τ_s increases.

This can be explained by two hypotheses:

(1) Electrons can only resolve the segment features of the FSK waves when $\tau_s \geq 100$ msec and the sideband features of the waves when $\tau_s \leq 50$ msec.

(2) There are wave-wave suppression effects among the sidebands.

As indicated before, an FSK wave consists of two sets of RF pulse trains at carriers f_1 and f_2, respectively. The electrons encountering more than four pulses of an FSK wave during the interaction resolve the sidebands. Each sideband can perturb and organize electrons within a finite $V_{\parallel}$ range centered at the corresponding resonance velocity. When the frequency spacings between the sidebands are large, their perturbed ranges of electrons in $V_{\parallel}$ do not overlap. The sidebands organize their own groups of electrons, and there is no mutual interaction between the sidebands. As the frequency spacings decrease, the perturbed ranges may overlap one another. The closer the spacings in frequency, the more the overlap. The chance of the electrons being organized by any one sideband coherently will be decreased, and hence

the wave triggering ability is reduced. This is a mutual suppression effect.

In Appendix C, we show that the frequency spacings between sidebands of a FSK wave are closely related to the value of τ_s. Roughly speaking, the spacings are inversely proportional to τ_s and independent of whether the wave is in 0- or π-conditions. As τ_s increases from 10 to 50 ms, the frequency spacings between sidebands are reduced from 50 to 10 Hz. There is more mutual suppression among the sidebands as their frequency spacings become smaller. This explains why the triggering ability of the FSK waves decreases as τ_s increases from 10 to 50 ms, regardless of whether they are 0-waves or π-waves.

An explanation for the observation that FSK waves with $\tau_s = 100$ ms can trigger emissions as often as the C-waves is postulated. The electrons have resolved the segment feature of the waves. Since τ_s is long, an electron may only encounter a single pulse and leave the interaction region before seeing a second pulse at the same carrier. Various electrons may see different portions of a pulse or different pulses. They will respond to individual pulses accordingly. By noting that a 100 ms pulse can trigger emissions by itself, we postulate that the emissions induced by the FSK waves with $\tau_s = 100$ msec are triggered by individual pulses. A 100 ms pulse is long enough to produce a "self-sustaining" oscillation in the "wave-particle system" in the magnetosphere in this period. Therefore, it can trigger emissions as often as a longer pulse. The emissions triggered by short pulses may have different forms than those triggered by long pulses [e.g., Helliwell and Katsufrakis, 1974]. The former tends to be weaker, too.

In Fig. 4.5, three FSK waves with τ_s = 10, 30, and 100 ms are illustrated. These examples are taken from the data from which the histogram in Fig. 4.4 is constructed. The spectrograms in the upper panel are analyzed by setting the time window TW of the data analyzer to 100 ms. The analyzer can clearly resolve the sidebands of the FSK wave with τ_s = 10 msec but not of those with τ_s = 30 and 100 msec. The spectrograms in the lower panel are obtained by setting TW to 250 msec. The sidebands of the FSK waves with τ_s = 10 and 30 msec but not those with τ_s = 100 ms can be resolved. It is clear that emissions developed from the FSK wave with τ_s = 100 ms are triggered by individual pulses. The emissions developed from the FSK wave with τ_s = 10 ms are triggered by sidebands. The 4.6 kHz sideband triggers a rising emission at its end. The 4.75 kHz sideband triggers an emission that "steps up" to the 4.8 kHz sideband at about the 400th msec and then forms a rising tone. Subsequently, it is observed that the FSK wave with τ_s = 30 ms exhibits an interesting modulation pattern in the upper panel. A rising emission appears to develop from the upper cutoff frequency of the pattern. However, the spectrogram with better frequency resolution shown in the lower panel indicates clearly that the modulation pattern is formed by the amplified sidebands and that the rising emission is triggered by the sideband at 4.6 kHz.

By Figs. 4.4 and 4.5, we have shown that electrons have a finite "memory time" during interactions with the FSK waves in the magnetosphere. The memory time is long enough for electrons to resolve the sidebands of the FSK waves with $\tau_s \leq$ 50 msec and short enough to respond to individual pulses of the FSK waves with τ_s = 100 ms.

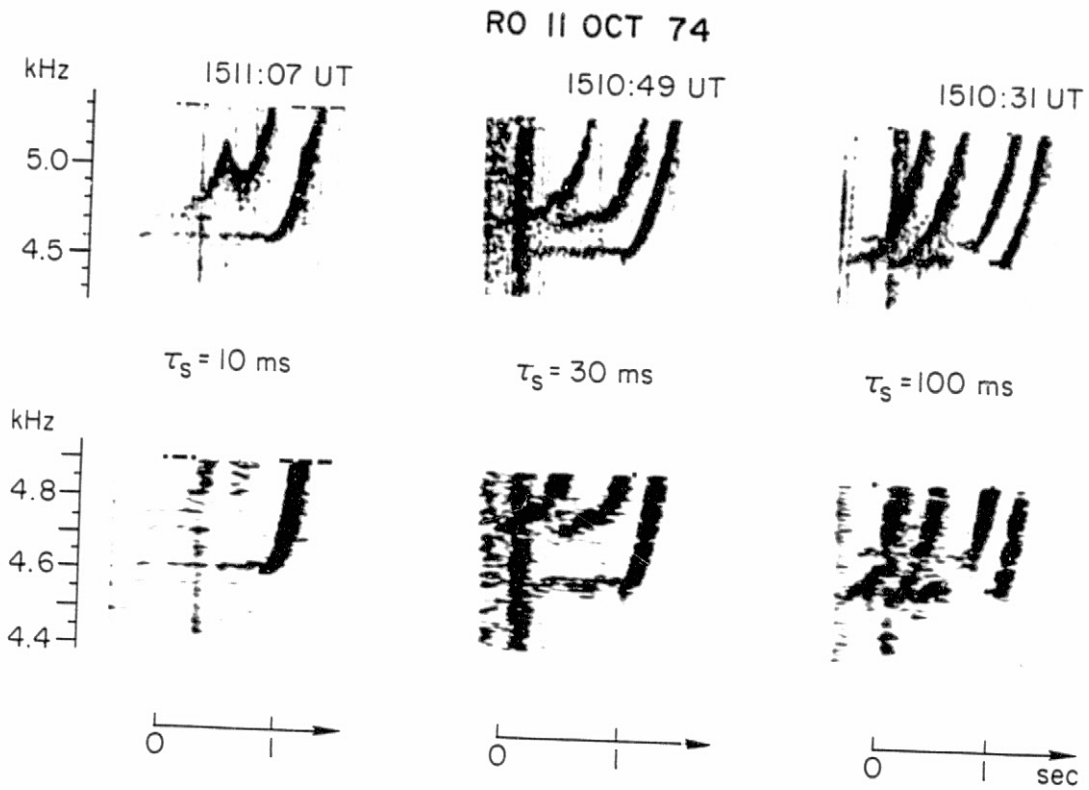

Fig. 4.5. EXAMPLES OF THE FSK WAVES FROM WHICH FIG. 4.4 IS CONSTRUCTED. The time and frequency resolutions of the spectrogram in the upper panel are ~70 ms and ~20 Hz, respectively, and that in the lower panel are 160 ms and 8 Hz.

A WM wave and an electron in resonance with it travel in opposite directions as shown in Fig. 4.6. The length of the interaction region is L_I. Assuming electron velocity $V_{\parallel}$ and wave group velocity V_g are constant in this region, then we have

$$L_I = t_W V_g = t_e V_{\parallel} \tag{4.1}$$

where t_W and t_e are the time required for a group front of a wave and an electron to pass through the region, respectively. As an electron moving from left to right through the IR, it encounters a portion of the wave. That same portion when measured at a receiving site will extend over a time interval $t_e + t_W$ that we shall call the apparent interaction time (AIT), i.e.,

$$AIT = t_W + t_e = L_I(1/V_g + 1/V_{\parallel}) \tag{4.2}$$

It is important to point out that AIT is not the real time period over which the electron and the wave interact. The interaction time is t_e as far as the electron is concerned and t_W as far as a group front of the wave is concerned. The AIT is a mapping in time of the "length" of the portion of a wave which the electron has encountered during their interaction.

The sidebands can be resolved only when more than two pulses in each carrier frequency have been encountered by the electrons. In other words, the electrons encountering more than four pulses of an FSK wave during the interaction can resolve the sidebands of the wave. Therefore, we adapt the condition

$$AIT \geq 4\tau_s \tag{4.3}$$

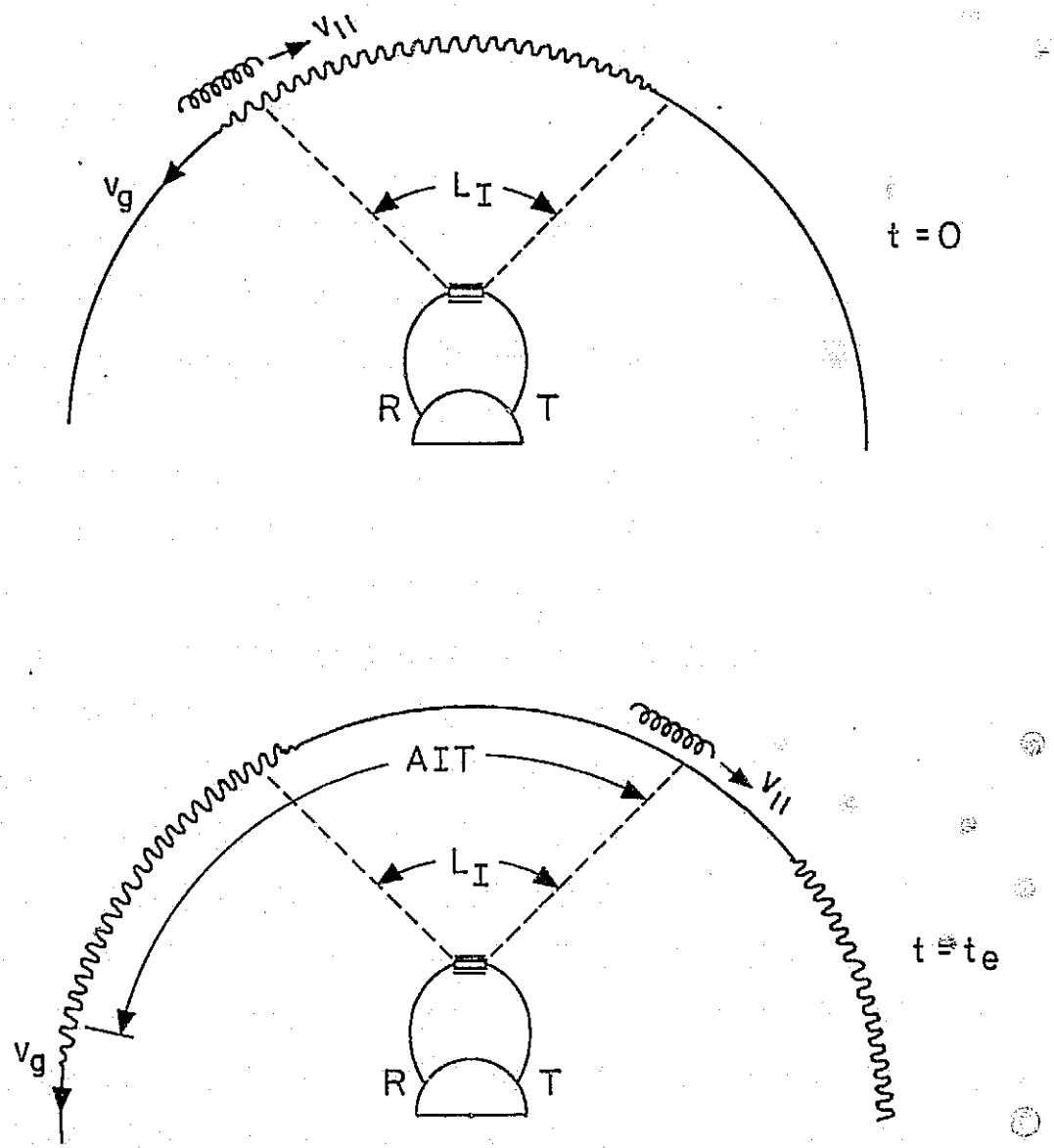

Fig. 4.6. ILLUSTRATION OF THE APPARENT INTERACTION TIME (AIT). The upper panel shows that an electron enters the interaction region, encountering a pulse traveling in the opposite direction. The lower panel shows the situation where the electron is leaving the interaction region.

that must be met for the electrons to resolve the sidebands. Electrons can resolve sidebands of the FSK waves with $\tau_s \leq 50$ ms. Thus, 200 msec appears to be a reasonable lower bound for AIT.

From the electron resonance condition and WM dispersion relation, it can be shown [e.g., Helliwell, 1965]

$$V_g = 2V_p(1 - \Lambda) \tag{4.4a}$$

$$V_{\parallel} \approx V_o = V_p\left(\frac{1 - \Lambda}{\Lambda}\right) \tag{4.4b}$$

where

$$V_p = \frac{cf_H}{f_p}\left[\Lambda(1 - \Lambda)\right]^{1/2}$$

$$\Lambda = f/f_H$$

Therefore,

$$AIT = \frac{L_I}{2V_p}\left[\frac{2\Lambda + 1}{1 - \Lambda}\right] \tag{4.5}$$

Using typical parameters at $L \approx 4$,

$$f_p \approx 180 \text{ kHz}$$

$$f_H \approx 13 \text{ kHz}$$

$$f = 1/3\ f_H$$

and assuming AIT = 200 msec, we find that

$$L_I > 2000 \text{ Km}$$

Furthermore, we know that the resonant energetic electrons do not resolve the sidebands when $\tau_s \geq 100$ ms. This fact sets an upper bound on L_I. We conclude that

$$4000 \text{ Km} > L_I > 2000 \text{ Km}$$

D. Sideband Triggerings and Features of Coupling

Multiple waves with small frequency spacings in between, propagating in the whistler mode (WM) in the magnetosphere, can interact with one another. A WM can interact with energetic electrons through cyclotron resonance, perturbing and organizing electrons contained within a small range of $V_{\parallel}$ centered at the cyclotron resonance velocity. The corresponding frequency range is termed the "coherence bandwidth." As the wave intensity increases, the perturbed $V_{\parallel}$ range grows and so does the coherence bandwidth. Multiple waves often organize different groups of electrons at various $V_{\parallel}$ ranges when the wave frequencies are largely separated. On the other hand, when the frequency spacings are so small that the perturbed $V_{\parallel}$ ranges of electrons overlap, electrons organized by one wave can also exchange energy with another. Wave-wave interactions thus occur through these electrons.

In this section, we shall show more examples of sideband triggering and then examples of energy coupling between sidebands.

Figure 4.7 shows an example of sideband triggering. The triggering wave is a π-wave with $\tau_s = 10$ ms and $\Delta f = 150$ Hz. The corresponding sidebands are spaced in frequency by 50 Hz. The calculated unamplified intensities of the sidebands are shown on the right. As noted in Appendix C, a FSK wave in a π-condition is a carrier-suppressed signal. The two

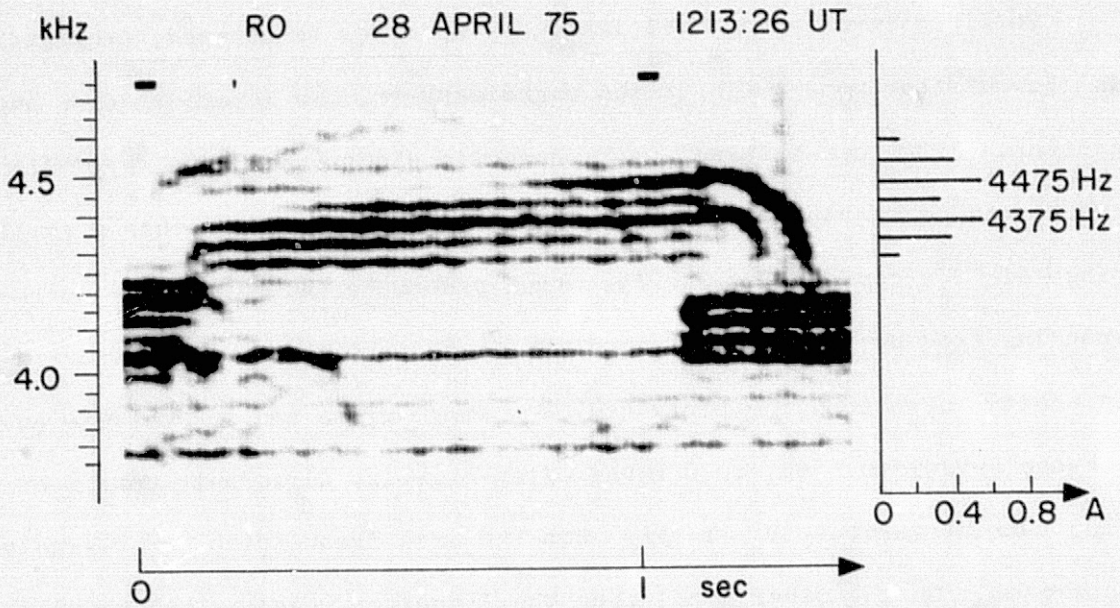

Fig. 4.7. A TYPICAL EXAMPLE OF SIDEBAND TRIGGERINGS. Sidebands can be amplified and trigger emissions, just like any other constant frequency WM signal.

carrier frequencies of the FSK wave in Fig. 4.7 are at 4.35 and 4.50 kHz. It is clear that there is no frequency component at these two frequencies.

There may be weak coupling between the 4.425 and 4.475 kHz sidebands; the intensity of one sideband decreases while the other increases. It is clear that the sidebands at 4.375 and 4.475 kHz, which happen to be the strongest ones at the input, trigger falling emissions at their ends. The sidebands can trigger emissions just as any constant frequency wave can.

The spectrogram is obtained by setting the time window to 100 ms. A triplet weighting function which is used to reduce the sidelops of the spectrum has reduced the time uncertainty by a factor of ~1.6. Therefore, the time and frequency resolutions of this spectrogram are ~70 ms and ~20 Hz, respectively.

It is worth mentioning that sidebands at various frequencies but with the same input power usually are not amplified uniformly. As a good example, the sidebands at 4.325 and 4.525 kHz have the same input intensity but the former has been amplified in the magnetosphere about 6 dB more than the later. (We shall show how this quantitative figure is obtained in Fig. 4.8.) The sideband amplification processes in the magnetosphere are either very frequency dependent or very sensitive to adjacent sidebands. In the latter case, the coherence bandwidth must be greater than the frequency spacings between the sidebands.

Figure 4.8 illustrates three more examples of sideband triggerings. The spectrograms in the four panels containing the same data are obtained by successfully reducing the gain of the analyzer in 6 dB per step. The relative intensities of the amplified sidebands then can be visualized.

The first example is repeated from Fig. 4.7. It clearly shows that the 4.325 kHz sideband is about 6 dB stronger than the 4.525 kHz sideband.

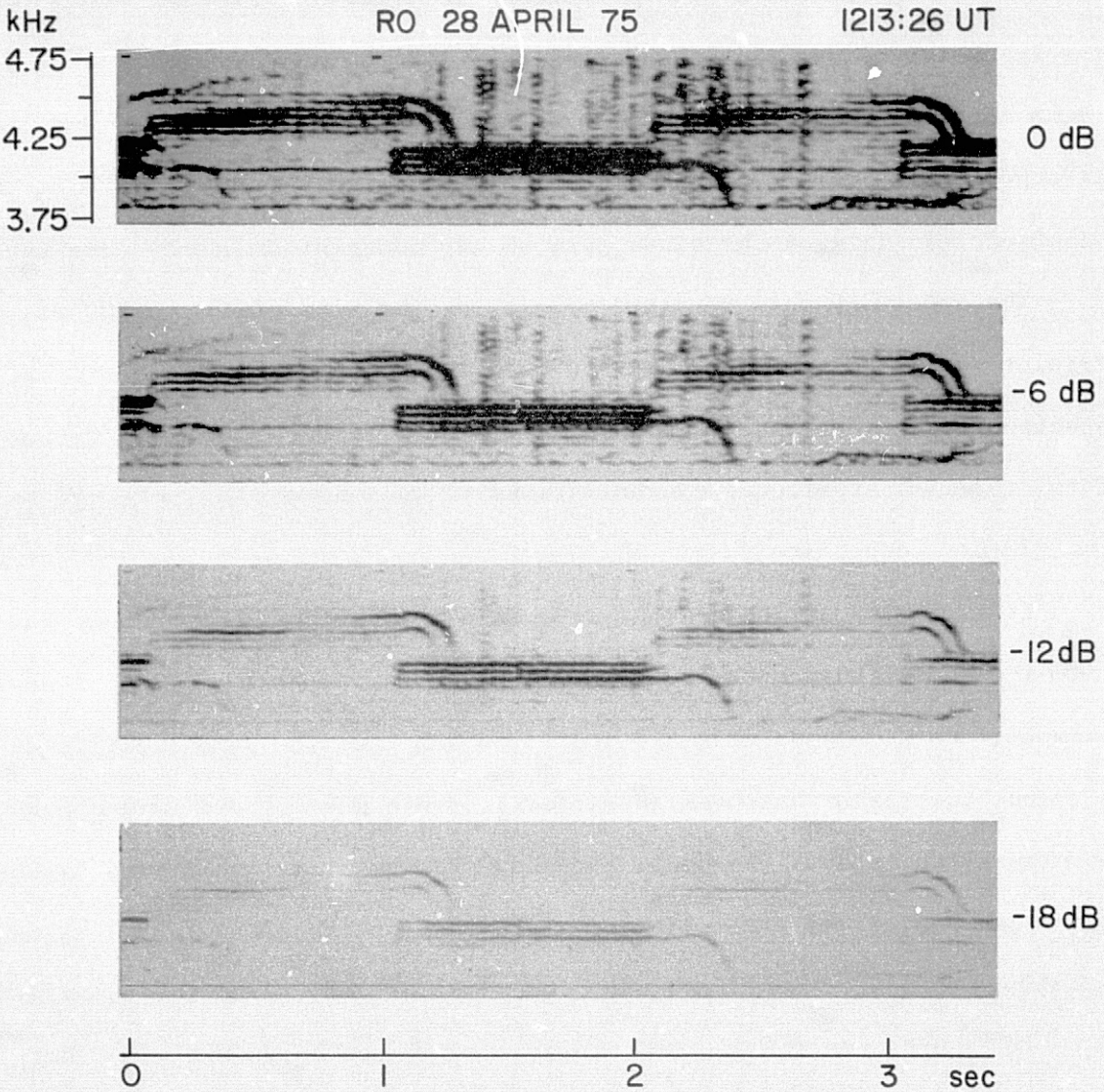

Fig. 4.8. MORE EXAMPLES OF SIDEBAND TRIGGERINGS. The panels showing the same data are obtained by successively reducing the analyzer's gain. The amplitude information is roughly obtained by this method.

The growth rate of the 4.475 kHz sideband is estimated to be ~36 dB/sec by measuring the time difference of the points where the sideband appears to have the same intensity between the successive panels. This is a rough estimation of sideband growth rate.

The second example, at a lower frequency band, is an O-wave with τ_s = 10 ms and Δf = 100 Hz. Its sidebands are 50 Hz apart too. There appears to be no mutual interaction. At the ends, the 4.1 kHz sideband triggers a small rising emission and the 4.05 kHz sideband triggers an emission that remains almost the same frequency for 120 msec and then becomes a falling tone.

There are at least two active power-line harmonies appearing on the records: one at 3.78 kHz (63rd PLH) and the other at 4.02 kHz (67th PLH). The emission triggered by the 4.05 kHz sideband appears to be entrained by the 67th PLH.

The fact that there are no apparent mutual interactions between the sidebands may indicate that the perturbed electron $V_{\parallel}$ ranges associated with various sidebands do not overlap. We may then conclude that the frequency spacings (50 Hz) between the sidebands are greater than the coherence bandwidth. But it is possible that the small frequency spacings between the sidebands have imposed limitations on the growth of the sidebands (a mutual suppression phenomenon). Under this condition, the sidebands may also appear as if there were no mutual interaction.

In order to resolve the ambiguity, a transmitter program, SIDEBAND SUPPRESSION (SISU) PROGRAM, has been designed for future experiment on this problem.

The third example is a π-wave. The amplified sidebands have almost the same features as the corresponding ones in the first example.

Figure 4.9 illustrates an example of sideband couplings. The triggering wave is a π-wave with $\tau_s = 10$ ms and $\Delta f = 150$ Hz. Its sidebands, whose unamplified intensities are calculated and shown on the right, are 50 Hz apart. The duration of the FSK wave is indicated by the horizontal bar just below the spectrogram. At the beginning, the magnetosphere favors the 3.975 kHz sideband which is not the strongest one at the input end. This sideband has been amplified in the magnetosphere 12 dB more than the others. The amplitude information is obtained by the same technique illustrated in Fig. 4.8.

As time goes on, the intensity increases. It is observed that the energy is coupled from the 3.975 to 4.025 kHz sidebands at about the 400th msec and that the coupling is through a discrete frequency jump.

Note that the time and the frequency resolutions of this dynamic spectrum are about 70 ms and 20 Hz, respectively.

At about the 600th msec, energy is transferred from the 4.025 to the 4.075 kHz sideband. Several "weak" rising emissions developed from the former sideband tend to release their energy to the latter.

The coupling processes seem to favor the coupling of energy to sidebands at higher frequencies. However, near the end of the FSK wave, the energy couples back from the 4.075 to the 4.025 kHz sideband, which then triggers an emission that remains almost at a constant frequency for about 500 msec after the sidebands are terminated; it then becomes a rising tone. The emission has grown about 12 dB. This suggests that there are mutual suppressions among the sidebands. The sidebands may have been amplified further, had their frequency spacings been larger. At the ends of the sidebands, the triggered emission, possibly entrained by a power line harmonic (PLH) at 4.02 kHz (5 Hz below the 4.025 kHz sideband),

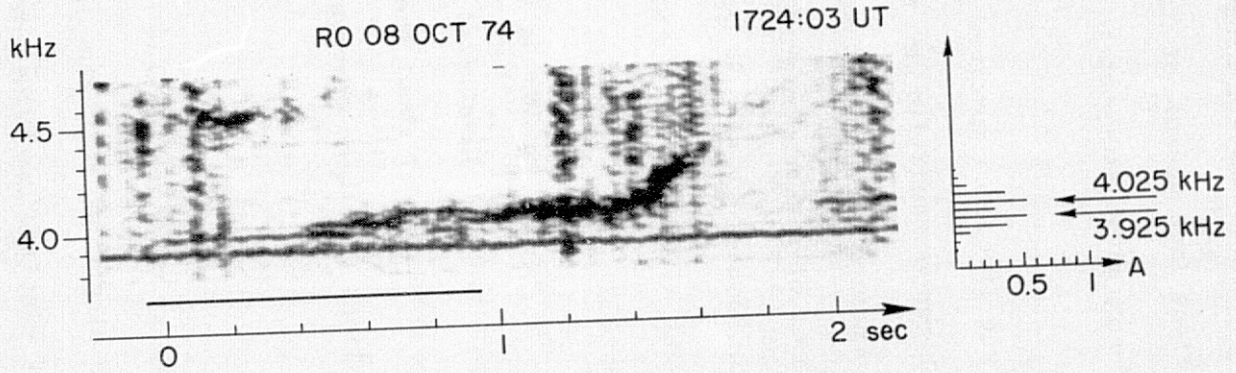

Fig. 4.9. AN EXAMPLE OF SIDEBAND COUPLINGS. The FSK wave with τ_s = 10 ms, Δf = 150 Hz, is a π-wave. The duration of the wave is indicated by the horizontal bar below the spectrogram. The thick horizontal line at 3.9 kHz is a local induction line. The energy of the 3.975 kHz sideband is coupled to the 4.025 kHz sideband at about the 400th msec, then to the 4.075 kHz sideband at approximately the 600th ms.

becomes the only coherent signal near 4.02 kHz capable of organizing electrons efficiently. There are no other signals to suppress its growth. Therefore, the emission grows.

The existence of an active PLH at 4.02 kHz is postulated because the emission frequency remains almost constant for about 500 msec. Furthermore, there are a few indications (not shown) of the existence of the 4.02 kHz PLH within half an hour, giving support to this interpretation.

This example indicates that the frequency spacings among the sidebands limit their growth. The coherence bandwidth in this particular case is greater than 50 Hz and depends on the intensity of the signal.

It also illustrates two features of sideband coupling. The first feature in which energy steps up or down discretely in frequency is illustrated by the coupling between the 3.975 and the 4.025 kHz sidebands at about the 400th msec and that between the 4.075 and the 4.025 kHz sideband at about the 950th msec. The second feature in which energy is transferred between sidebands by emissions is illustrated by the couplings between the 4.025 and the 4.075 kHz sidebands at about the 600th msec. These two features of sideband couplings have been observed many times.

E. Discussion

The key to an explanation of energy coupling between two waves at different frequencies involves those electrons that can interact with both waves in the magnetosphere. An electron perturbed by a WM wave oscillates in $V_{\parallel}$ around the cyclotron resonance velocity V_o. The range of excursion in $V_{\parallel}$ depends on the wave intensity, the electron pitch angle, as well as the instantaneous phase angle between the electron

and the wave when the electron is exactly at $V_{\parallel} = V_o$ (see Appendix B). Various electrons in resonance with the wave may have different excursion range in $V_{\parallel}$. As far as the wave is concerned, it can perturb and organize electrons which are in a finite $V_{\parallel}$ range centered at the resonance velocity V_o. We assume the perturbed $V_{\parallel}$ range to be the trapping range ΔV_t. The corresponding frequency range is the coherence bandwidth. Two waves with a large frequency difference organize electrons in different $V_{\parallel}$ ranges. The waves are mutually independent. When the frequency difference is small, the perturbed $V_{\parallel}$ ranges overlap. Electrons in the overlapped range can exchange energy with both waves. They serve as means of energy coupling between waves.

According to the homogeneous model in which a constant wave is assumed (see Appendix B), the perturbed $V_{\parallel}$ range ΔV_t is proportional to the square root of the wave intensity. The wave intensity can be "measured" by estimating the size of ΔV_t. We have estimated the size of ΔV_t by finding the critical frequency difference within which two waves interact.

It is important to point out that in reality this homogeneous model may not be adequate because

(1) the inhomogeneity of the geomagnetic field changes the size of ΔV_t, and

(2) the wave intensity in the interaction region is not uniform.

To the author's knowledge, there is no published relationship between the size of ΔV_t and wave intensity (even assuming a constant wave) in inhomogeneous models.

According to Dysthe's simple model [1971] in which a constant external torque is assumed to account for the inhomogeneity in an interaction region (IR), the size of ΔV_t is reduced as the IR moves away from the equator. Thus, to produce the same ΔV_t, a stronger wave is required in the inhomogeneous model than in the homogeneous model. Since WPI is believed to occur around the equatorial region where the inhomogeneity is small, we shall use the homogeneous model to estimate the wave intensity in the IR. The wave intensity in an inhomogeneous IR must be greater than the estimated value. Moreover, the actual wave intensity is not uniform in the IR. Therefore, the estimated value can only account for the order of magnitude of the average intensity in the IR.

It is interesting to visualize the coherence bandwidth from the point view of electrons. A constant frequency WM wave interacts with energetic electrons in a finite IR, causing the electrons to oscillate in $V_{\parallel}$. The Doppler-shifted frequency of the wave as seen by an electron with a small velocity excursion $\Delta V_{\parallel}$ is not constant. The wave has a finite bandwidth $k\Delta V_{\parallel}$ as far as the electron is concerned. This bandwidth is a "resonance bandwidth" produced by WPI. Electrons with various $\Delta V_{\parallel}$ see different bandwidths $(k\Delta V_{\parallel})$ associated with the wave. The electrons with $\Delta V_{\parallel} = \Delta V_t$ see the largest bandwidth which we call the coherence bandwidth. The coherence bandwidth is in the order of 50 Hz or more for most of the coherent WM waves in the magnetosphere.

When an electron encounters two waves in the magnetosphere, its motion becomes more complicated. Suppose that the two waves at f_1 and f_2, traveling with the phase velocities V_{p1} and V_{p2}, have intensities (E_{w1},B_{w1}) and (E_{w2},B_{w2}), respectively, where $f_1 > f_2$, $V_{p1} > V_{p2}$, and $B_{w1} > B_{w2}$. The total wave magnetic field B_{wT}, as shown in Fig. 4.10,

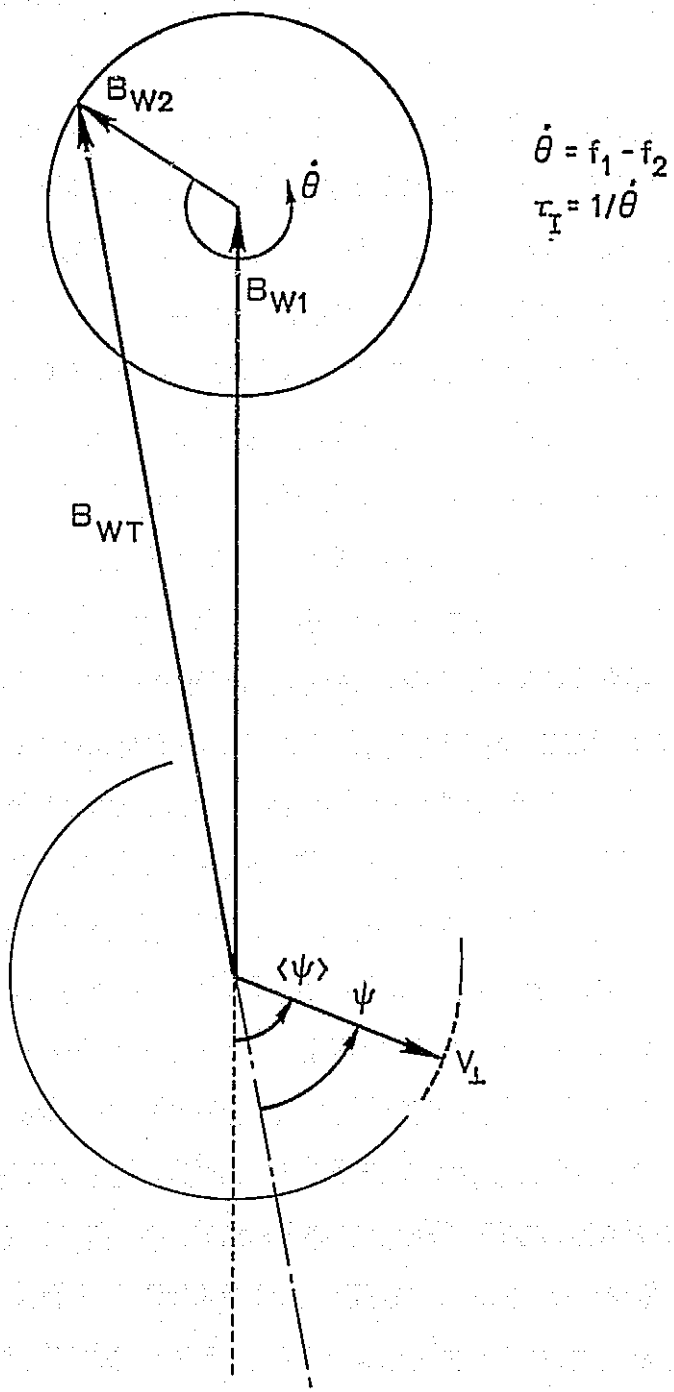

Fig. 4.10. AN ELECTRON MOTION IN TWO WAVES. The frame is moving with the phase velocity of wave 1. The magnetic field of wave 2 rotates with an angular frequency that equals the frequency difference of these two waves.

is a vector sum of B_{w1} and B_{w2} and varies with time in the frame moving with V_{p1}. We have assumed that $|V_{p1} - V_{p2}|$ is much smaller than V_{p1} and V_{p2} so that the electric field of wave 2 is negligible. In that frame, E_{w1} disappears, B_{w1} is static [e.g., Matsumoto, 1972], and B_{w2} rotates with a frequency $\dot{\theta}$, where $\dot{\theta}$ equals $|f_1 - f_2|$. $1/\dot{\theta}$ corresponds to a time constant that equals the rotation period of B_{w2} and is called τ_I, i.e.,

$$\tau_I = 1/\dot{\theta} \tag{4.6}$$

This time constant τ_I shall be the same in the lab frame. The reason we derive this quantity in a wave frame is to "fix" one wave in a frame so that the relative rotation between the field components of these two waves can be visualized easily.

The detailed calculation of energy coupling between two waves through the resonance electrons is still being investigated. Meanwhile, we can still argue qualitatively for a rough criteria that determines whether the waves will mutually interact or not. It is believed [e.g., Helliwell, 1967; Helliwell and Crystal, 1973] that the bunching time T_b is a characteristic time of energy exchange between a constant amplitude wave and its resonant electrons. When $f_1 - f_2$ is large, the electrons in resonance with wave 1 can not effectively interact with wave 2. In one bunching period, B_{w2} has rotated more than one cycle. Its effect on an electron which is in resonance with wave 1 has been smeared out. Similarly, electrons in resonance with wave 2 cannot effectively interact with wave 1. Thus, these two waves are organizing different sets of electrons and do not mutually interact. One could specify a criterion under which two waves are mutually independent as

$$T_b > \tau_I \tag{4.7}$$

According to Eqs. (B.16) and (4.6), we can rewrite the criterion as

$$\Delta f_{CB} < |f_1 - f_2| \tag{4.8}$$

It states that, when the frequency difference is greater than the coherence bandwidth, two waves do not interact. Thus, by finding the critical frequency difference within which two waves interact, we have found the coherence bandwidth Δf_{CB}. The wave intensity can then be estimated by Eq. (B.16).

Equation (4.8) is a rough criterion. We have assumed B_{w2} to be small enough so that it does not alter the motions of electrons which are in resonance with wave 1. This is a "small perturbation" assumption. When B_{w2} is not small, a criterion that determines whether two waves interact or not must involve both B_{w1} and B_{w2}. One such criterion is

$$\frac{1}{2}\,(\Delta f_{CB1} + \Delta f_{CB2}) < |f_1 - f_2| \tag{4.9a}$$

where Δf_{CB1} and Δf_{CB2} are the corresponding coherence bandwidths of wave 1 and wave 2. It implies, as shown in Fig. 4.11, that the perturbed $V_{\parallel}$ ranges associated with the two waves in the electron distribution overlap unless

$$\frac{1}{2}\,(\Delta V_{t1} + \Delta V_{t2}) < |V_{01} - V_{02}| \tag{4.9b}$$

where V_{01} and V_{02} are the resonance velocities associated with wave 1 and wave 2, respectively.

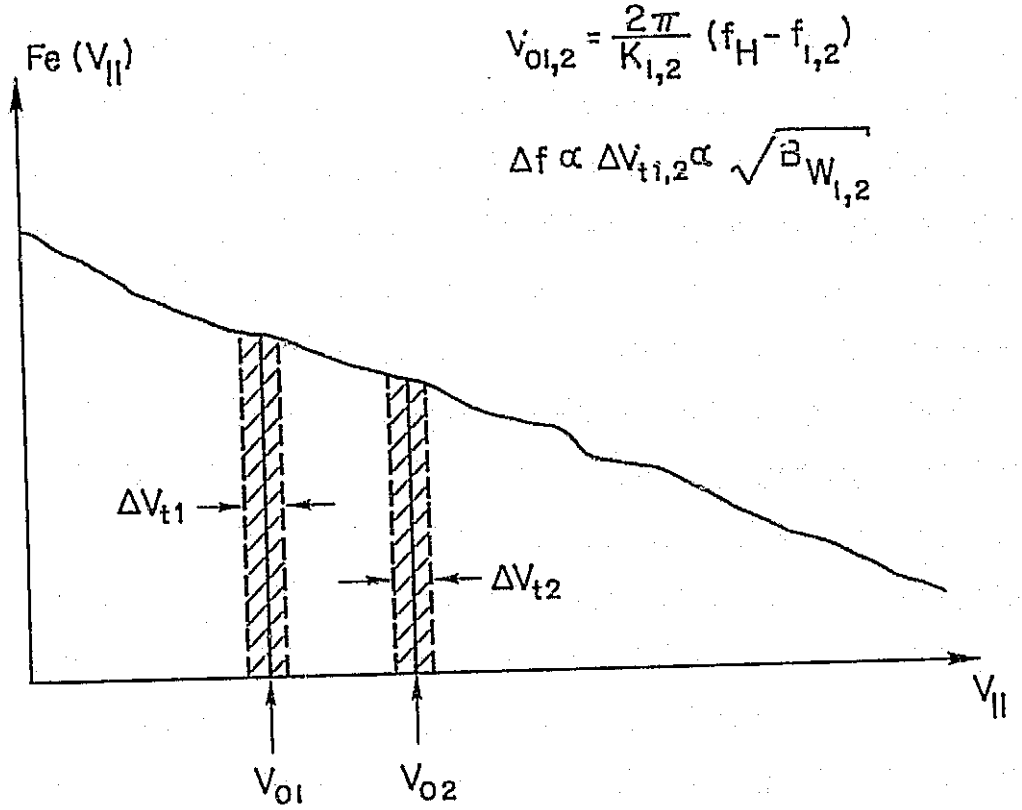

Fig. 4.11. DEMONSTRATION OF THE RANGES OF V_{ll} OVER WHICH THE ELECTRONS ARE ORGANIZED BY TWO WAVES WITH A LARGE FREQUENCY DIFFERENCE. The purturbed V_{ll} ranges are not overlapped. There shall be no interaction between these two waves.

From Eq. (4.9a), it can be shown that there is a factor of 4 in the estimated intensity of wave 1, B_{w1}, between the cases in which $B_{w1} = B_{w2}$ and the ones in which $B_{w1} \gg B_{w2}$. Since we are only interested in the order of magnitudes of the wave intensities in the IR, Eq. (4.8) appears to be suitable for our purpose. We shall bear in mind, however, that the estimated value could be off by a factor as large as 4.

The excursion range $\Delta V_{\parallel}$ for various electrons in resonance with a wave are different. It seems reasonable to average these excursion ranges. It can be shown by Eq. (B.4b) that

$$\Delta V_{\parallel} = 2\left[2\,\frac{\Omega_w V_{\perp}}{k}\,(1 - \cos\,\psi_R)\right]^{1/2} \tag{4.10}$$

where ψ_R is the instantaneous phase angle between the wave and an electron when $V_{\parallel}$ exactly equals V_o. Using the approximation for trapped electrons

$$V_{\perp} \simeq V_o \tan\,\alpha \tag{4.11}$$

we have

$$k\Delta V_{\parallel} = 4(k\Omega_w V_o \tan\,\alpha)^{1/2}\,\left|\sin\,\frac{\psi_R}{2}\right| \tag{4.12}$$

Assuming that electrons initially are uniformly distributed in the phase angle, we can show that $\Delta V_{\parallel}$ averaged over ψ_R is

$$\overline{k\Delta V_{\parallel}}\Big|_{\psi_R} = \frac{8}{\pi}\,(k\Omega_w V_o)^{1/2}\,\tan^{1/2}\,\alpha \tag{4.13}$$

Thus, we have an averaged coherence bandwidth (over the phase angle)

$$\left.\overline{\Delta f_{CB}}\right|_{\psi_R} = \frac{4}{\pi^2} (k\Omega_w V_o)^{1/2} \tan^{1/2} \alpha \qquad (4.14)$$

Equation (4.14) reveals that $\left.\overline{\Delta f_{CB}}\right|_{\psi_R}$ is dependent on the electron pitch angles. In the magnetosphere, waves can interact with electrons at various pitch angles. The electron distribution as a function of energy and pitch angle in the magnetosphere can be chosen as [e.g., Liemohn, 1967]

$$f(W,\alpha) \propto W^{-p} \sin^m \alpha \qquad (4.15)$$

This model has several advantages. It is mathematically simple. The energy variation is reasonable and can be fitted into the particle data [Schield and Frank, 1970].

Equation (4.15) can be written as

$$f(V_\perp, V_\parallel, \alpha) \propto \frac{\sin^m \alpha}{\left(V_\parallel^2 + V_\perp^2\right)^p} \propto \frac{\sin^m \alpha}{V_o^{2p} \sec^{2p} \alpha} \qquad (4.16)$$

i.e.,

$$f(\alpha) \propto \sin^m \alpha \cos^{2p} \alpha \qquad (4.17)$$

We have used the resonance condition $V_\parallel \approx V_o$ and $V_\perp \approx V_o \tan \alpha$. Figure 4.12 shows the distribution function $f(\alpha)$ for various values of m and p. It is noticed that the peak tends to move to high pitch angles as m increases and tends to move to low pitch angles as p increases. The condition $m = 0$ implies an isotropic pitch angle distribution at a given energy level. It does not imply uniform distribution at a given $V_\parallel$.

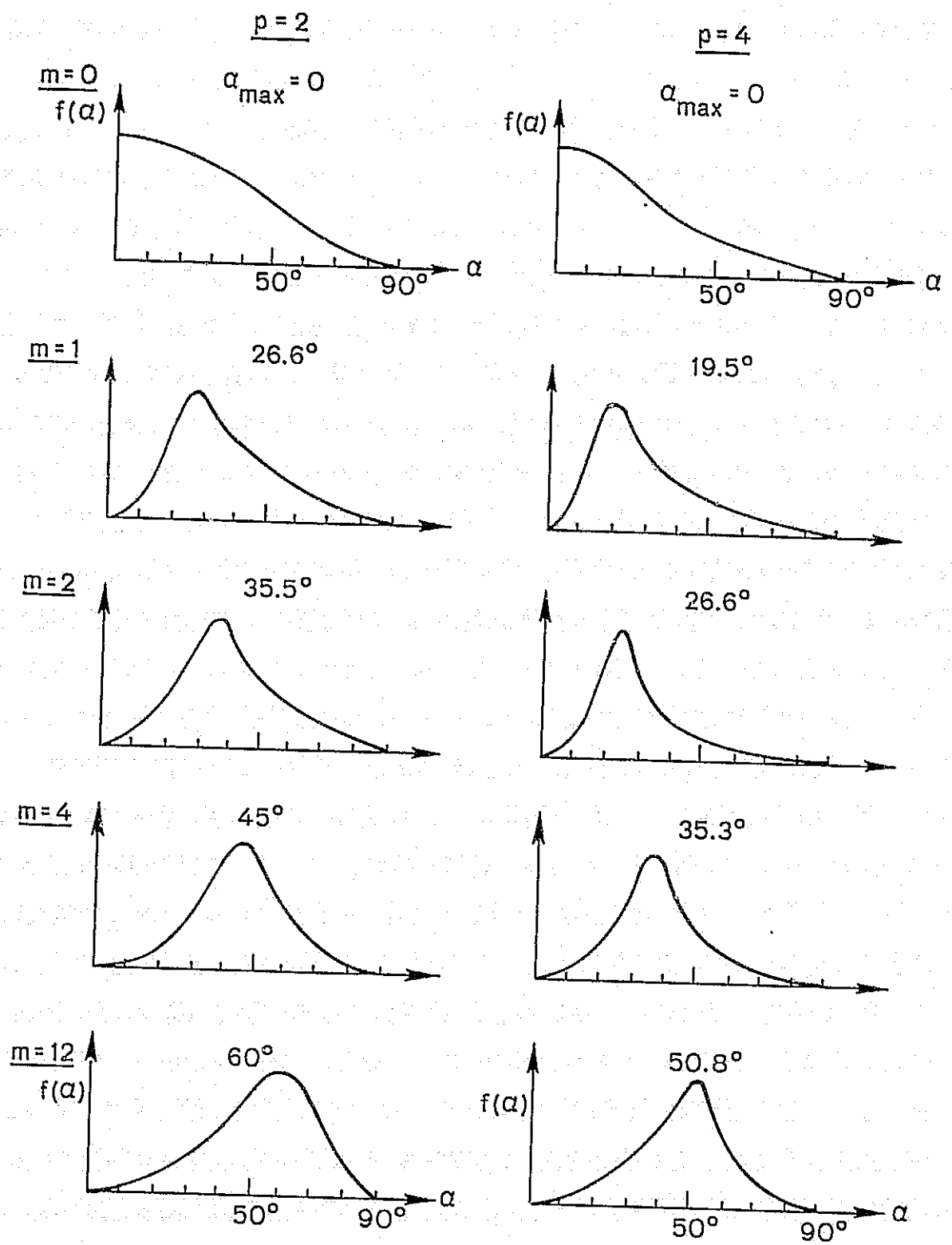

Fig. 4.12. PLOTS OF $f(\alpha) = \sin^m \alpha \cos^{2p} \alpha$ AS A FUNCTION OF α FOR VARIOUS VALUES OF m AND p. The α_{max} at which $f(\alpha)$ has a maximum value is at $\alpha = \tan^{-1} m/2p$.

We shall average the coherence bandwidth again over a pitch angle distribution. From Eq. (4.14),

$$CB \triangleq \overline{\Delta f_{CB}}\Big|_{\psi_R,\alpha} = \frac{4}{\pi^2} k\Omega_w V_o \Gamma(m,p) \tag{4.18}$$

where

$$\Gamma(m,p) = \int_{\alpha_L}^{\alpha_U} \tan^{1/2} \alpha \; g(\alpha) \; d\alpha$$

$$g(\alpha) = \frac{\sin^m \alpha \cos^{2p} \alpha}{\int_{\alpha_L}^{\alpha_U} \sin^m \alpha \cos^{2p} \alpha \; d\alpha}$$

$$\alpha_L \triangleq \text{loss cone}$$

$$\alpha_U \triangleq \cos^{-1} \frac{V_o}{c}$$

Figure 4.13 shows the values of Γ as functions of m and p for a case in which $\alpha_L = 7°$ and $\alpha_U = 85°$. It is on the order of unity.

Equation (4.18) is the relationship between the coherence bandwidth and the wave intensity in the magnetosphere. We have a qualitative criteria for deciding whether two waves with a frequency difference Δf can mutually interact or not. When $\Delta f > CB$, there is no mutual interaction. When $\Delta f < CB$, they will interact. Thus, by estimating the critical frequency difference Δf_c within which two waves interact and using Eq. (4.18) and the condition

$$\Delta f_c = CB$$

we have been able to measure the average wave intensity in IR. For simplicity, we shall refer to CB as "coherence bandwidth" hereafter.

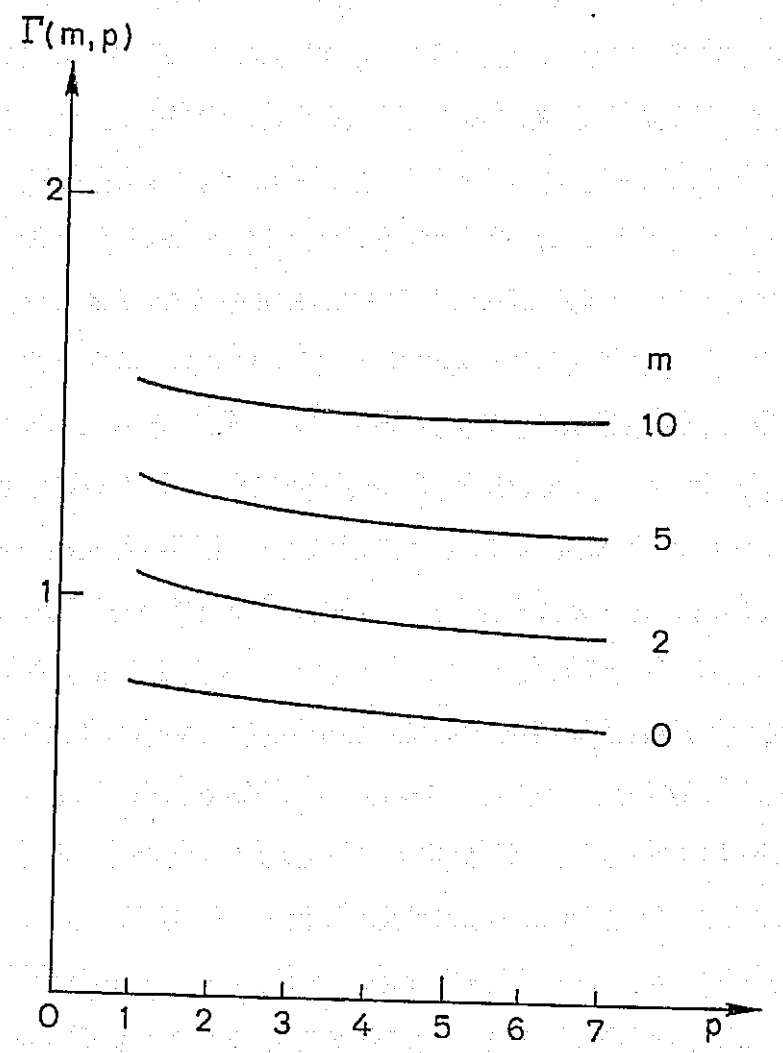

Fig. 4.13. PLOTS OF $\Gamma(m,p)$ FOR THE CASE WHERE $\alpha_L = 7°$ AND $\alpha_U = 87°$.

F. LISP Program

From Section C, we have found that sidebands with frequency difference less than 50 Hz can mutually interact. We have also found in many occasions that sidebands with a 50 Hz frequency difference can grow and trigger emissions independently. It appears that 50 Hz could be a good measure of coherence bandwidth.

There are several transmitter programs designed specifically to measure the coherence bandwidth. One such program is the Line Spectrum (LISP) Program. The LISP program, shown in Fig. 4.14, consists of FSK waves with τ_s = 10 msec. The frequency difference between the pulse train at the upper frequency and the one at lower frequency is switched between 100 and 200 Hz every minute. The upper frequency f_{HI} remains the same during the transitions. As a result of this modulation, the spectrum of the wave is switched between the two shown in Fig. 4.15. The sidebands are spaced at multiples of 50 Hz. It is noticed that the sideband at f_{HI} is always at the same amplitude and continuous in phase, while its nearby sidebands change either amplitudes or phases during the transition.

If the coherence bandwidth of the sideband at f_{HI} is less than 50 Hz, then its behavior is independent of the changes in nearby sidebands. On the other hand, if its coherence bandwidth is greater than 50 Hz, it interacts with other sidebands at nearby frequencies. Therefore, altering the nearby sidebands should affect its growth. By examining the amplitude of the sideband at f_{HI} during transitions, we can determine whether the CB is greater than 50 Hz or not.

Figure 4.16 shows an example of this program. The upper panel shows the spectrogram in which the time and the frequency resolutions are about

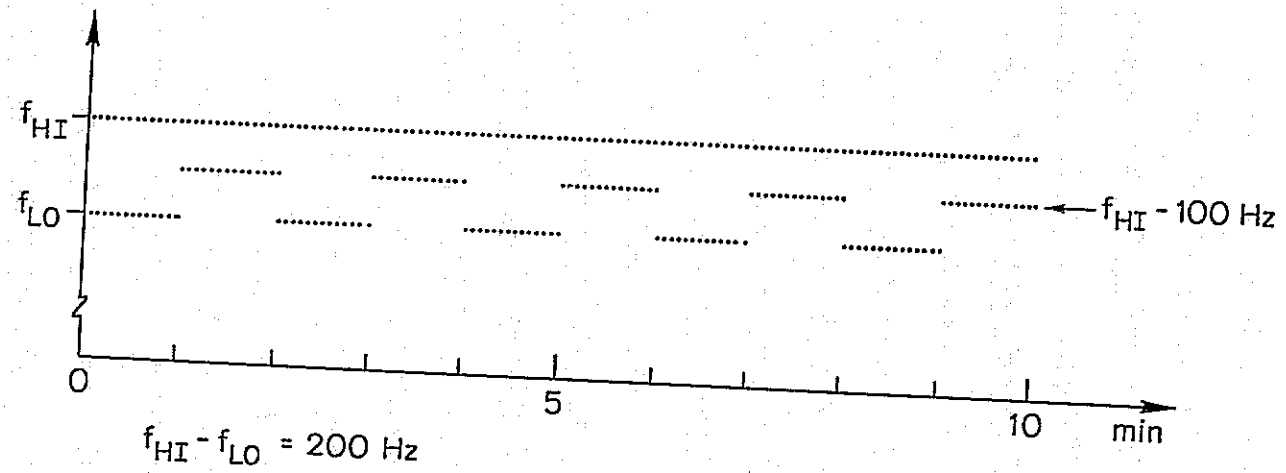

Fig. 4.14. A SKETCH OF THE LISP PROGRAM THAT CONSISTS OF FSK WAVES WITH τ_s = 10 ms. The upper frequency f_{HI} remains the same, while the lower frequency alternates between 100 and 200 Hz below f_{HI} regularly every minute.

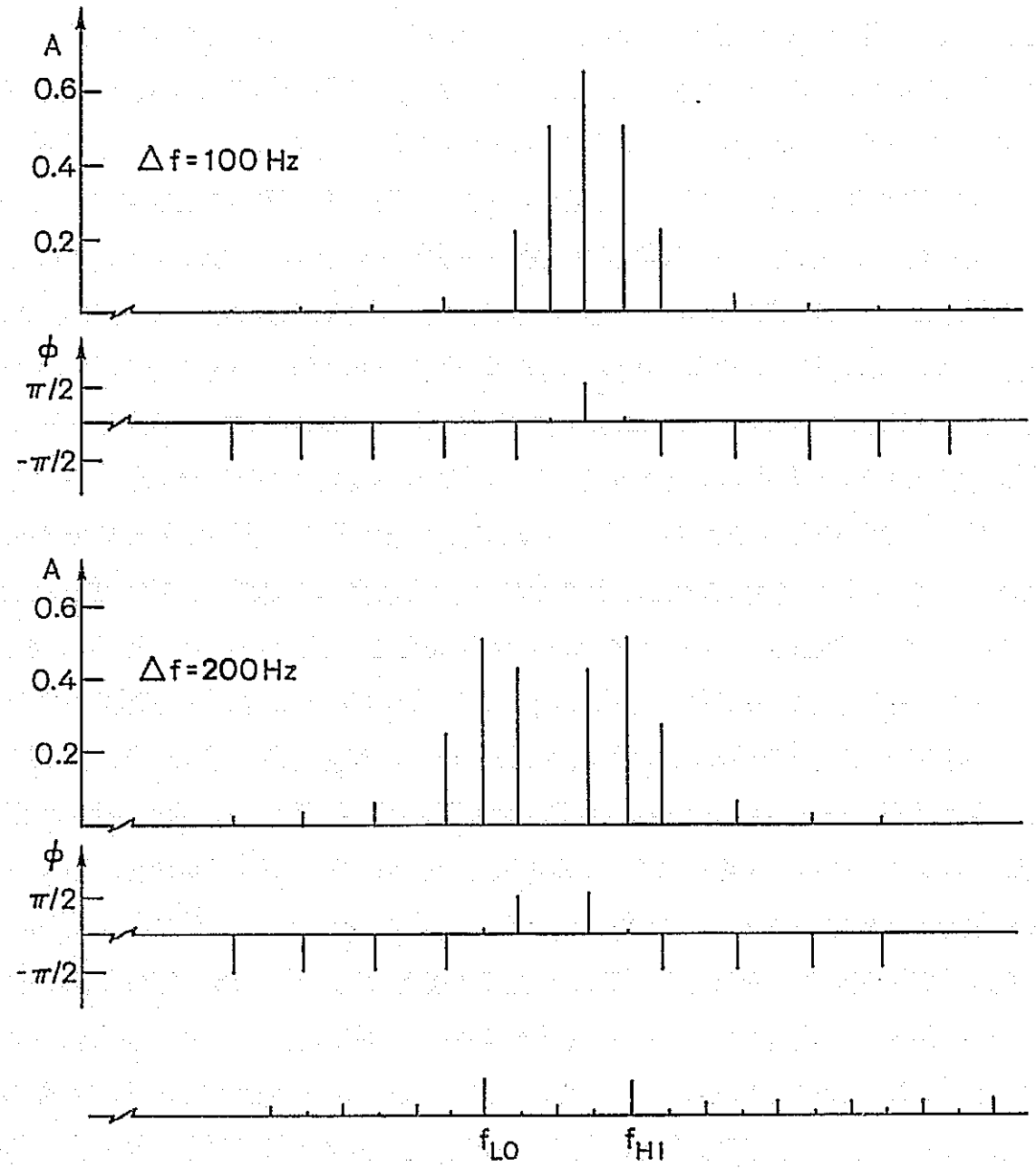

Fig. 4.15. THE SPECTRUM OF AN FSK WAVE WITH Δf = 100 Hz AND τ_s = 10 ms AND THAT WITH Δf = 200 Hz AND τ_s = 10 ms. The spike at f_{HI} in both spectra have the same amplitude and phase. ϕ is the phase of the spectrum.

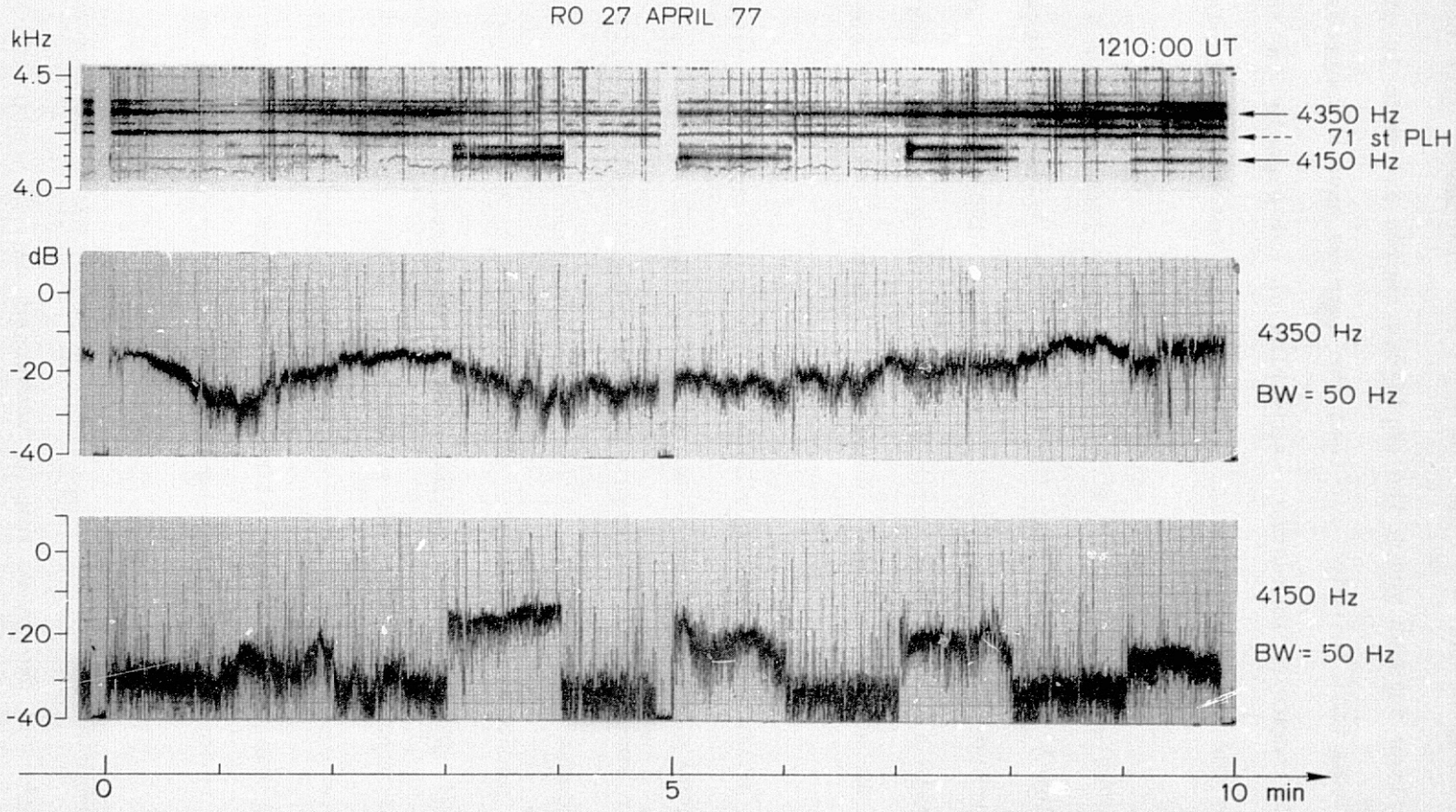

Fig. 4.16. AN FXAMPLE OF THE LISP PROGRAM. The dynamic spectrum has high frequency resolution (~2 Hz). The stimulated sidebands have been resolved.

350 msec and 3 Hz, respectively. The middle and lower panels depict the amplitude variations of the 4.35 and the 4.15 kHz sidebands. The bandwidth of the filter through which the amplitude charts are made is about 50 Hz. It is important to point out that the records have a compressed time scale. The regular fluctuations appearing on the signals in the spectrogram are due to asynchronization between the recording and playback recorders.

There are PLH's on the spectrogram. The strong signal around 4.26 kHz drifting slowly in frequency at the rate of a few hertz per minute is a local induction line (71st PLH). The 4.25 kHz sideband appearing every other minute is observable, with difficulty, only in the first, the third, and the seventh minute, where the induction line is above 4.255 kHz.

There are "stimulated sidebands" about 7 Hz away from the parent sidebands. A good example can be observed in the eighth minute. The expanded dynamic spectrum of the eighth minute is shown on Fig. 4.17. The 4.20 kHz sideband has stimulated two sidebands spaced at about 7 Hz above and below the parent sideband. The 4.15 and 4.35 kHz sidebands also stimulate sidebands in this period. It is observed that the stimulated sidebands occur only when the parent signals are strong. It has been reported previously that a constant frequency signal can trigger sidebands [Chang and Park, 1977]. Stimulated sidebands are believed to be a phenomenon caused by nonlinear wave-particle interactions in the magnetosphere.

The 4.35 kHz sideband is at f_{HI}, the frequency at which both the sideband amplitude and the phase remain unchanged at the transitions. The slow changes in amplitude shown on the middle panel are due to the

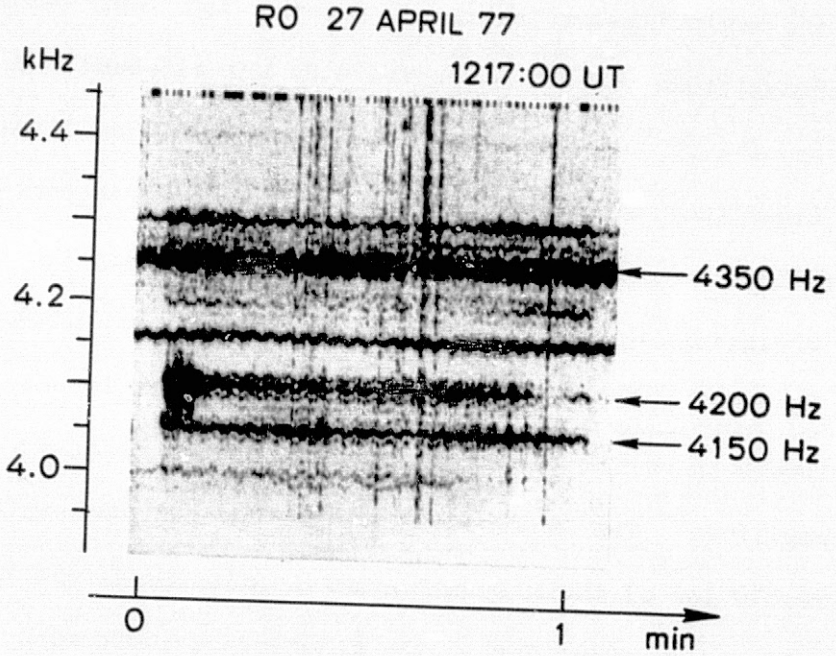

Fig. 4.17. EXPANDED DISPLAY OF THE DYNAMIC SPECTRUM IN THE EIGHTH MINUTE IN FIG. 4.16.

slow temporal variations in the magnetospheric conditions. The transitions occur at ~2.3 seconds after the minute marks. From such compressed time-scale records, it is hard to locate precisely the time of transitions. However, the lower panel, showing the amplitude of the 4.15 kHz sideband that is "switched on" every other minute, provides definite indications of the time of the transitions. It is noticed that, at the transitions at the beginnings of the third, fourth, and tenth minute, there are sudden amplitude variations on the 4.35 kHz sideband. The variations can be as large as 3 dB. From the studies of the expanded records, it is clear that there are no sudden amplitude variations during the rest of the transitions. The expanded records during the transitions at the beginnings of the second, fourth, eighth, and tenth minutes are shown in Figs. 4.18, 4.19, 4.20, and 4.21, respectively. Note that the 0-dB levels in various amplitude records do not refer to the same absolute amplitude. The arrows indicate the time of transitions. The frequency resolution of these spectrograms is different from the one shown on Fig. 4.16 and is about 7 Hz. The sidebands stimulated by the 4.35 kHz sideband cannot be resolved.

It is observed from Fig. 4.16 that only when the 4.35 kHz sideband is at high intensity can the transitions affect its amplitude. This suggests that the intensity of the 4.35 kHz sideband in the IR is such that its coherence bandwidth is about 50 Hz and varies slowly with time. Using the available whistler data, we have found that the path is at $L \simeq 4$ and $N_{eq} \simeq 400\ cm^{-3}$. Assuming that $p = 4$ and $m = 1$ for the electron distribution in the magnetosphere and a CB equal to 50 Hz, we have calculated the wave intensity in the IR by Eq. (4.18) to be on the order of 2.5 mγ. From the argument given in the previous section, there could be

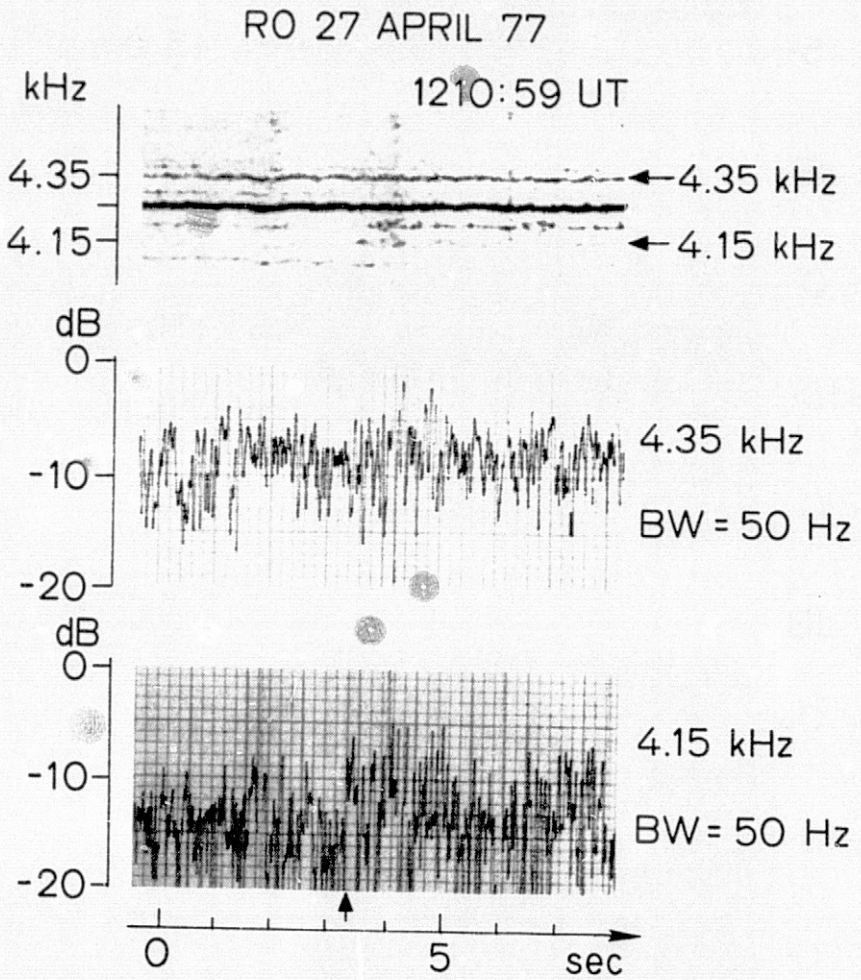

Fig. 4.18. EXPANDED TIME SCALE OF THE TRANSITION AT THE SECOND MINUTE IN FIG. 4.16. 0-dB levels are not the same as shown in Fig. 4.16.

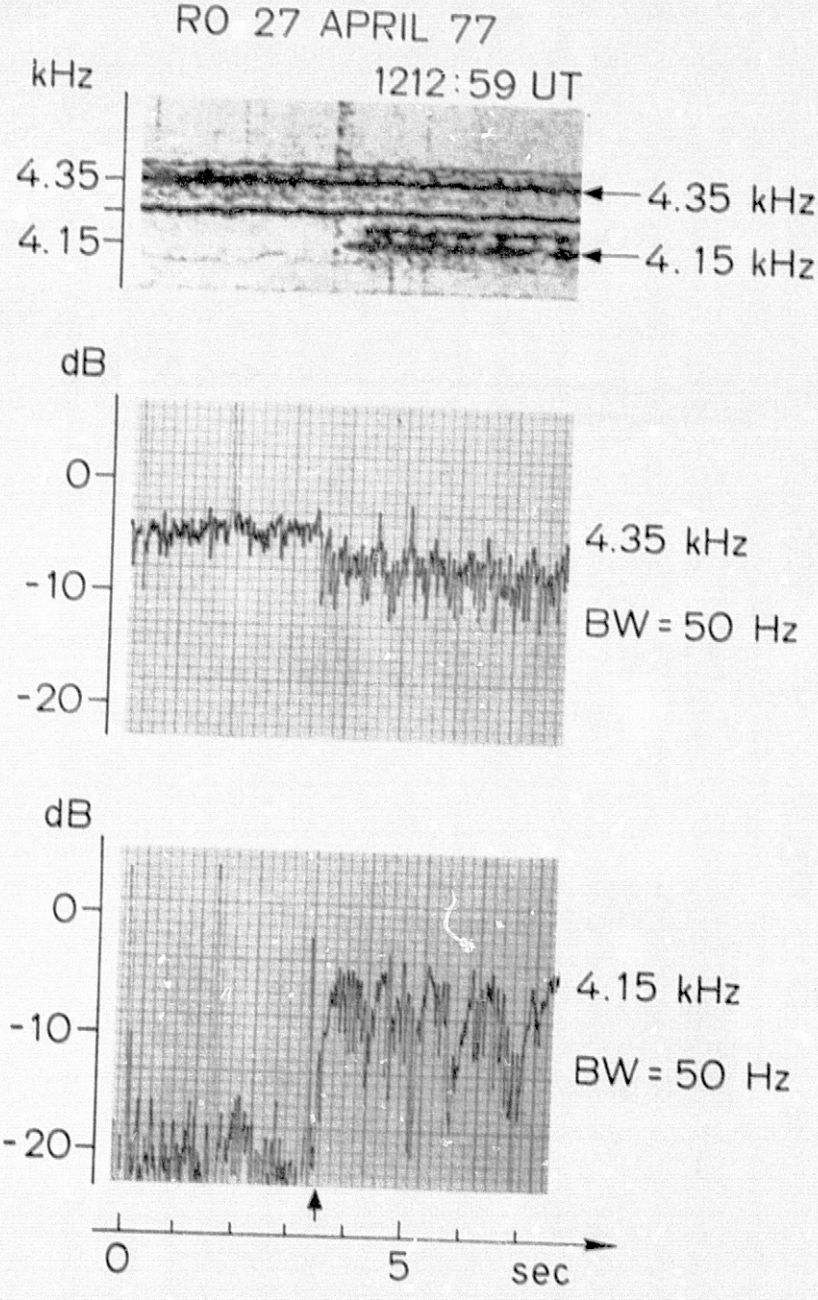

Fig. 4.19. EXPANDED TIME SCALE OF THE TRANSITION AT THE FOURTH MINUTE IN FIG. 4.16. 0-dB levels are not the same as shown in Fig. 4.16.

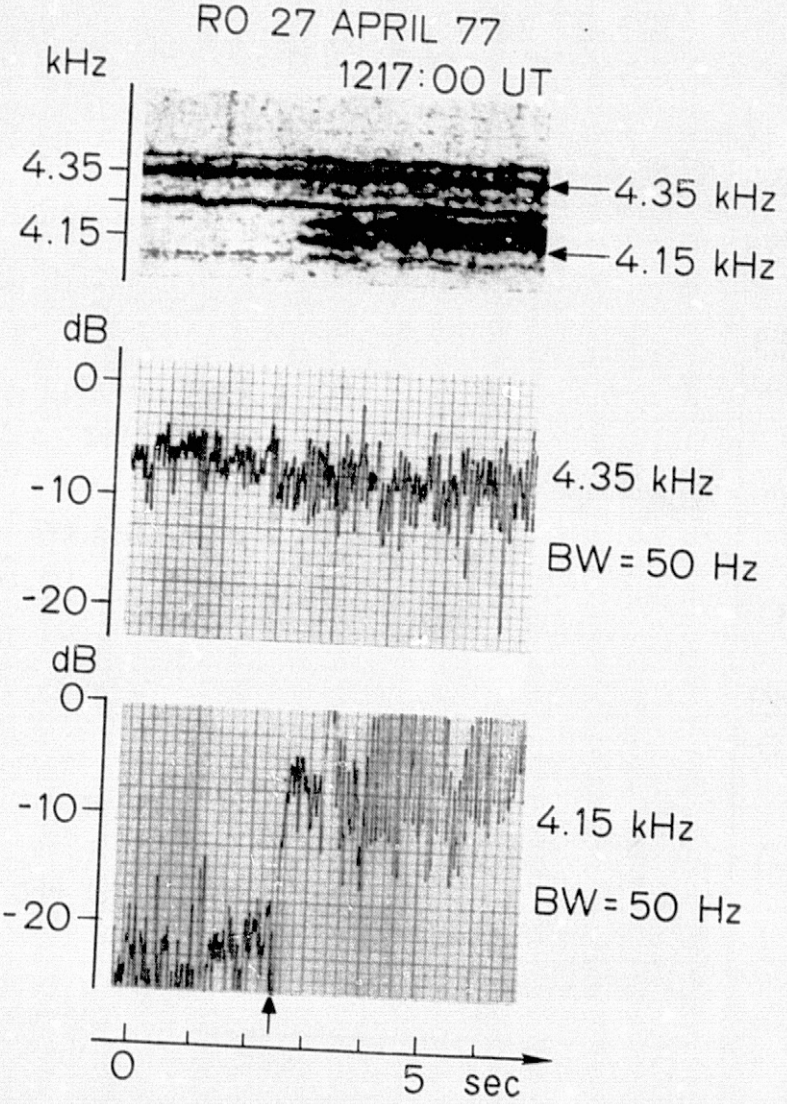

Fig. 4.20. EXPANDED TIME SCALE OF THE TRANSITION AT THE EIGHTH MINUTE IN FIG. 4.16. 0-dB levels are not the same as shown in Fig. 4.16.

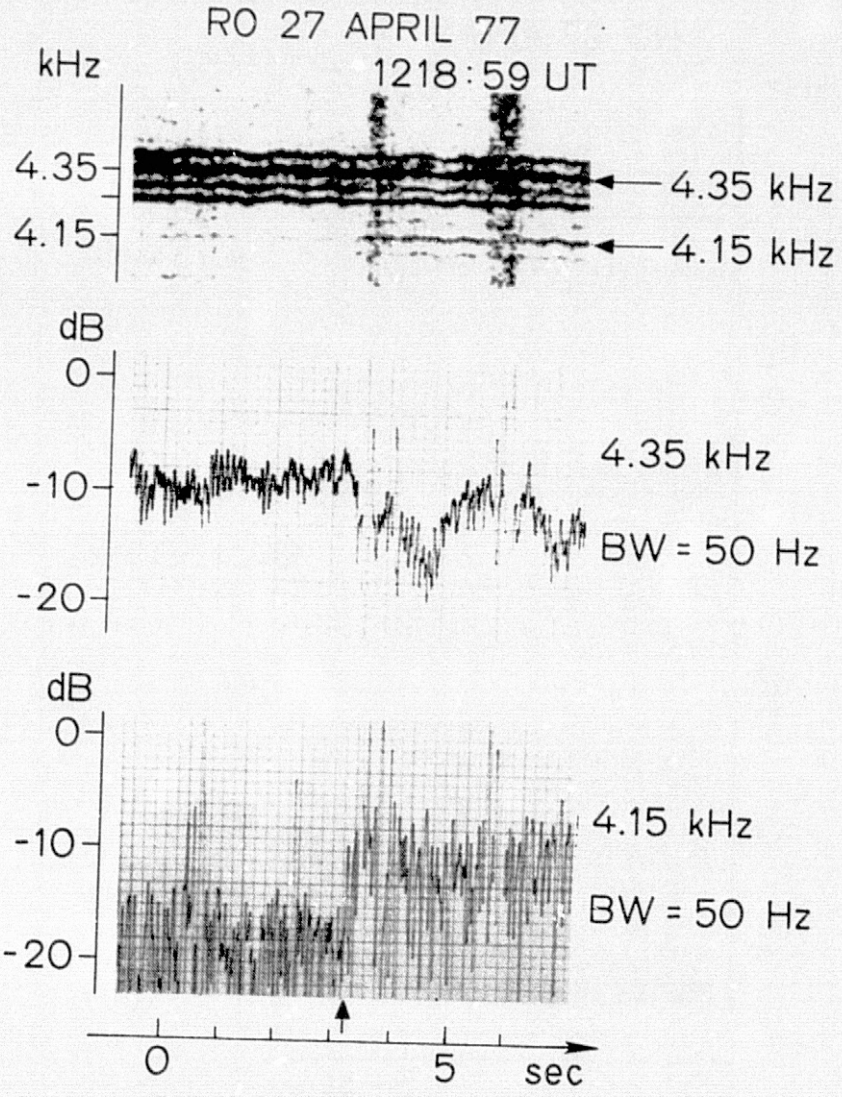

Fig. 4.21. EXPANDED TIME SCALE OF THE TRANSITION AT THE TENTH MINUTE IN FIG. 4.16. 0-dB levels are not the same as shown in Fig. 4.16.

an error as large as a factor of 4 in the estimated wave intensity. Thus, the estimated wave intensity is somewhere between 2.5 to 10 mγ, in good agreement with satellite measurements [Heyborne, 1966; Burtis, 1974; Inan et al, 1977]. This estimation is based on the assumption that the interaction occurs at the equator. If the interaction occurs off equator where the inhomogeneity of the geomagnetic field becomes important, the estimated wave intensity would be larger.

It is interesting to note that the intensity of the 4.35 kHz sideband increases at the transitions in the third and ninth minutes where the 4.15 kHz sideband is turned off. On the other hand, the intensity of the 4.35 kHz sideband decreases at the transition in the fourth minute where the 4.15 kHz sideband is turned on. It is suggested by Helliwell [private communication, 1978] that the 4.4 kHz sideband (f_{HI} + 50 Hz in Fig. 4.15) may couple energy to the 4.35 kHz sideband at the transitions where the intensity of the 4.35 kHz sideband is high. The dynamic spectrum in Fig. 4.16 indicates that the 4.30 kHz (f_{HI} - 50 Hz) sideband has not been amplified significantly in the magnetosphere. At the transitions where the 4.15 kHz (f_{LO}) sideband is turned off, the input intensity of the 4.4 kHz sideband is reduced by 10 percent. It should therefore be amplified less, and the corresponding coherence bandwidth should decrease. Therefore, the intensity of the 4.35 kHz sideband increases, consistent with the observation.

G. Summary and Conclusion

In this chapter, we have shown that the FSK waves can be viewed as several constant frequency signals. In the magnetosphere, electrons can resolve these sidebands when the modulation period in the signal is small

compared to the interaction time between the wave and the electrons. Otherwise, the electrons can only resolve pulses of the FSK waves. This is the basis of the method we used in estimating the length of the interaction region (IR). It has been found that the IR lies between 2000 and 4000 km.

Transmitting FSK waves is equivalent to injecting multiple waves into the magnetosphere. The frequency difference is controllable by varying the pulse length. We have found that waves with frequency spacing less than 50 Hz often show mutual interactions. Suppression and coupling among sidebands are often observed. We have identified two different features of energy couplings. In the first feature, energy of a sideband transfers to another sideband by a discrete jump in frequency. In the second feature, the energy coupling is accomplished by "small" emissions that link one sideband to another.

The interaction between two forced mode signals is attributed to the electrons that can exchange energy with both waves. Assuming that the trapping width is the width of $V_{\parallel}$ within which electrons can be organized effectively by a wave, we have established the relationship of wave intensity and the critical frequency spacing within which two waves can interact. This critical frequency spacing is called the coherence bandwidth and is determined by averaging over both the phase angle as well as the pitch angle. It is found that the coherence bandwidth is on the order of 50 Hz for the sidebands. The corresponding wave intensity is somewhere between 2.5 to 10 mγ in a homogeneous model and could be larger in inhomogeneous models.

Chapter V

SUMMARY AND RECOMMENDATIONS

A. Introduction

The purpose of this report has been to present an experimental investigation of VLF wave-wave interaction in the magnetosphere. In this chapter, we shall summarize the contributions of this report and make suggestions for further investigation. The contributions in the study of pulse distortion, due to propagation in the magnetosphere, in the area of interaction between gap-induced emission and post-gap signal and in the field of sideband mutual interaction will be covered. The suggestions for further work will include the same three areas.

B. Summary of the Present Work

1. Pulse Propagation in the Magnetosphere

We have been performing experiments to investigate VLF wave-particle and wave-wave interactions in the magnetosphere by injecting VLF pulses from the Siple transmitter. These pulses are distorted before arriving at the interaction region which is believed to be near the equator. The distortion caused by propagation through the dispersive medium may have stretched the pulses enough to alter the details of WPI in the magnetosphere. It is therefore essential to know how the pulse is distorted due to propagation in the magnetosphere.

As far as we know, the distortion of a VLF pulse propagating in the magnetosphere has not been calculated previously.

In Chapter II, we have described the method of analysis. Study of pulse propagation in the magnetosphere has provided the following results:

(1) The group velocity calculated at the carrier frequency can accurately predict the arrival time of a pulse only when the time delay refers to the "centers," not to the leading edges of the pulses.

(2) The frequency of a distorted pulse is not constant over the duration of the pulse. The largest deviations occur at the front and/or the rear ends of the pulse.

(3) The frequency at which a pulse has minimum distortion at the equator is the "nose" frequency.

(4) A discontinuity in the phase of a fixed amplitude sine wave introduced on the ground can develop into an amplitude gap when the wave arrives at the equator. The gap can be as large as 20 msec as a wave at 3 kHz propagating through a duct at $L = 4$.

(5) A digital equalizer has been designed to compensate for the phase distortion. Computer simulations show that the equalizer can completely cancel the phase distortion. This device could be used either as a pre- or post-processor to remove the distortion developed in the magnetosphere.

2. Gap-Induced Emissions

The phenomenon of gap-induced emissions has been reported for the first time. A 10 msec gap in a triggering wave can induce emissions which may then interact with the post-gap signal, causing suppression and entrainment effects. The interaction involves a natural mode and a

forced mode signal, and this is termed forced mode/natural mode wave-wave interaction (FNWWI).

Among the results of this study are the following:

(1) This phenomenon suggests that the tail-end emissions start to develop within a time period less than 10 ms.

(2) Experimental data show that, as the gap is opened up in time, we can "scan" the development of emissions. One of the results confirms an earlier observation that emissions always start with a small rise in frequency.

(3) A 70 msec gap is long enough to permit a falling tone to fully develop.

(4) A new feature of FNWWI has been discovered. The post-gap signal can "capture" a falling emission that is 90 Hz below the transmitter signal, causing the emission to overshoot toward the positive frequency direction. The frequency difference between these two signals appears to be an important factor in determining whether or not the interaction can occur.

3. Sideband Triggering

Sideband triggering has been reported for the first time. It was an unexpected result from the studies of a transmitter program designed for other purposes. This discovery enabled us to study sideband interactions. Suppressions and couplings between sidebands are commonly observed. We call this interaction SIDEBAND MUTUAL INTERACTION (SMI).

From modulation theories, we know that discrete sidebands are created by periodic modulations on the signals. However, in the

magnetosphere, the energetic electrons respond only to certain sidebands. The electrons can interact with the sidebands of the waves with small modulation periods but not with those generated by long modulation periods. We have shown in Chapter IV that this observation enables us to estimate the length of the interaction region.

Study of sideband triggerings has provided the following results.

(1) The length of the interaction region has been estimated to lie between 2000 and 4000 km.

(2) Sidebands, like any other constant frequency signals, can trigger emissions.

(3) 50 Hz appears to be the critical frequency spacing within which sidebands mutually interact.

(4) The coupling is attributed to the electrons that can interact with both waves. It is believed that a wave can only organize electrons within a finite range of $V_{\parallel}$ centered at the resonance velocity. Thus, the interaction must come from the electrons in the overlapped $V_{\parallel}$ range.

(5) The LISP program suggests that 50 Hz is the order of the coherence bandwidth of sidebands. The sideband intensity in the interaction region has been estimated to be on the order of 2.5 ~ 10 mγ according to a homogeneous model, in reasonable agreement with satellite measurements [Heyborne, 1966; Burtis, 1974; Inan et al, 1977].

C. Suggestions for Future Work

1. Pulse Propagation in the Magnetosphere

The work can be extended to nonducted signals by combining a ray tracing program and the algorithm discussed in Chapter II. It is generally true that the dispersions for nonducted signals are greater than for ducted signals. Therefore, the propagation distortion shall be even more important in the nonducted case.

It is necessary to use a pre-processor, or equalizer, on the transmitter end to compensate for the phase distortion developed from the path between the transmitter and the interaction region. Realization of this device appears to be feasible.

2. FNWWI

It seems feasible to design a transmitter program to study the "capture" feature of the FNWWI in a somewhat controllable way. The slopes of the frequency of the gap-induced emissions can not be controlled easily. But the frequency and phase of the post-gap signal can be changed. Thus, studies of this interaction for various conditions on the frequency and phase differences between the falling emissions and the post-gap signals can be carried out.

3. SMI

More VLF wave injection experiments are needed to establish a relationship between the input wave intensity and the size of the coherence bandwidth. At present, we only have qualitative evidence,

suggesting that coherence bandwidth increases as the wave intensity becomes stronger.

It will be very useful to inject only two WM waves into the magnetosphere. The frequency difference will be varied from a few hertz to 200 Hz for various wave intensities. This experiment will give us quantitative information on the coherence bandwidth versus the input wave intensity. It may also tell us when the mutual suppressions occur and when the mutual couplings become predominant. A refined model of wave-wave interaction in the magnetosphere can then be constructed from this information.

In the theoretical area, it is necessary to develop the studies of two-wave interactions, either by analytical methods or by computer simulations. Understanding the electron motions in two WM waves in a homogeneous model appears to be the first step in the solution to this problem.

Appendix A

A COMPUTER CODE SIMULATING VLF PROPAGATION IN THE MAGNETOSPHERE

This appendix lists one of the computer programs that simulate VLF pulse propagations in a duct in the magnetosphere.

```
C
C THE PROGRAM CALCULATES THE DISTORTIONS OF A PULSE PROPAGATING THROUGH
C A DUCT IN THE MAGNETOSPHERE.  THE B FIELD IS A DIPOLE FIELD
C THE DISTORTED PULSED IS TRANSLATED TO 500 HZ FOR DISPLAY
C THE FIRST DATA CARD INCLUDES L,DE,NEQ,PULSE LENGTH IN MS,
C THE CARRIER FREQUENCY AND THE STARTING TIME OF THE PULSE
C THE SECOND DATA CARD INCLUDES THE NO. OF CARRIER FREQUENCY TO BE USED
C AND THE INCREMENT OF THE CARRIER FREQUENCY
C THERE ARE 6 DISPLAY OF THE PULSE SHAPE ALONG THE PATH FOR EACH FREQUENCY.
C
C
      COMMON B(1026),BI(1026),CR(512),CI(512),PD(512)
      REAL BI,CR,CI,PD,SI(126),CT (1025)
      REAL L,F0,DPH,DDFP,NEQ
      INTEGER NF,SA,DE,NP,NL,IN(65) ,NFR
      INTEGER N3
      EQUIVALENCE (BI(1),CT(1))
      CALL TPLTR
      CALL PIOCS(20)
      WRITE (1,11)
11    FORMAT ('NO. OF FILES TO BE SKIPPED IN TAPE 82')
      NF=0
      READ (1,*)  NF
      CALL SKIPF(82,NF)
      READ (5 ,*)L,DE,NEQ,NP,F0,NT
      N=512
      WRITE (6,60) L,DE,NEQ
60    FORMAT (1X,'L=', F5.1,2X, 'DE=',I1,2X,'NEQ =',F10.2,'PER CC')
      NI=2*NT+1
      NL=2*(NT+NP)
      READ (5,*) NFR,DF
      DO 110 I=1,1026
110   B(I)=0
      DO 111 I=NI,NL,4
      B(I)=0
      B(I+1)=1
      B(I+2)=0
111   B(I+3)=-1
      CALL CTA (10,B,IN,SI,0)
      CALL CTA (10,B,IN,SI,3)
      DO 1011 K=1,NFR
      INT =17
      WRITE (6,61) F0,NP
61    FORMAT (/1X,'THE CARRIER FREQUENCY='F10.2,' HZ',2X,
     1    'THE PULSE LENGTH =',I3,' MS')
      DO 112 I=1,1026
      MM=1
112   BI(I)=B(I)
      CALL CTA (10,BI,IN,SI,-3)
      BI(1025)=BI(1)
      N3=1
      CALL PDIPO(L,F0,NEQ,DE,NP)
      CALL PLOPS (CT,N3)
      DO 1010 KI=1,5
      N3=N3+1
      CALL PDELY(L,DE,NEQ,INT,DPH,N,F0,MM)
```

```
      NM=NN+1
      DDFP=(INT-1)*DPH*180/3.14159
      WRITE (6,62) DDFP
62    FORMAT(1X,'THE PULSE HAS TRAVELED FROM THE BOTTOM OF THE DUCT UP',
     4 'TO THE POSITION AWAY FROM THE EQUATOR BY ',F10.2,' DEGREE')
      CALL CTA (10,BI,IN,SI,-3)
      BI(1025)=BI(1)
      CALL PLOPS (CT,N3)
1010  INT=INT-4
1011  FO=FO+DF
      CALL TPLTX
      STOP
      END
C
C
      SUBROUTINE PDELY(L,DE,NEQ,INT,DPH,N ,FO,MM)
C
C
C THIS SUBROUTINE CALCULATES THE PHASE DELAY OF EACH FREQUENCY COMPONENTS
C FOR A PULSE PROPAGATING IN A DUCT.
C
C
      COMMON B(1026),BI(1026),CR(512),CI(512),PD(512)
      REAL TY(21),FI(512)
      REAL P1(21),FP(21), FH(21),SF,CF,NEQ,OM,L,LM,KE,MH,LM1
      INTEGER INT, IST2,IST3,N,M1,JR,JI,DE
      R1=6500
      RO=6400
      G1=9.8E-03 *(RO/R1)**2
      OM=2*3.14159/(24*3600)
C CALCULATING FP,FH,AND P1=RO*L*COS(LM)*SQRT(1+3*SIN(LM)**2)
C FOR EACH POINT ALONG THE PATH
C THERE ARE 21 POINTS FROM THE BOTTOM OF THE MAGNETOSPHERE UP
C TO THE EQUATER
      REQ=RO*L
      FPEQ=9E03 *SQRT(NEQ)
      RT= SQRT ((RO*L-R1)/R1)
      FAI1= ATAN(RT)
      SF1= SIN(FAI1)
      CF1= COS(FAI1)
      IF (DE .EQ.1) GO TO 100
      IF (DE .EQ.2) GO TO 101
      IF (DE .EQ.3) GO TO 102
      IF (DE .EQ.4) GO TO 103
100   CH=0.08
      CO=0.9
      CHE=0.02
      T=1600
      GO TO 200
101   CH=0.08
      CO=0.9
      CHE=0.02
      T=3200
      GO TO 200
102   CH=0.4
      CO=0.5
      CHE=0.1
      T=1600
      GO TO 200
103   CH=0.4
```

```
      CO=0.5
      CHE=0.1
      T=800
200   FAI=0
      KE=1.38E-23
      MH=1.673 E-27
      HH= KE*T/(MH*G1)*1.E-06
      HO=HH/16
      HHE=HH/4
      ZEQ=R1-(R1**2)/REQ-(OM**2/(2*G1))*(REQ**2-(R1*CF1)**2)
      EHEQ= EXP(-ZEQ/HH)
      EOEQ=EXP(-ZEQ/HO)
      EHEEQ= EXP(-ZEQ/HHE)
      VDE=CH*EHEQ+CO*EOEQ+CHE*EHEEQ
      LM1= SQRT(1/VDE)
      TEMP1= SQRT(1+3*SF1*SF1)
      P1(21)= RO*L*CF1*TEMP1
      FP(21)=SQRT(LM1)*FPEQ
      FH(21)= 8.736E05*(1/L/CF1/CF1)**3*TEMP1
      DPH=FAI1/20
      DO 1000 I=1,20
      SF = SIN(FAI)
      CF=COS(FAI)
      R=RO*L*CF*CF
      Z=R1-(R1**2)/R-(OM**2/(2*G1))*((R*CF)**2-(R1*CF1)**2)
      EH=EXP(-Z/HH)
      EO= EXP(-Z/HO)
      EHE=EXP(-Z/HHE)
      VNU=CH*EH+CO*EO+CHE*EHE
      LM= SQRT(VNU/VDE)
      TEMP = SQRT(1+3*SF*SF)
      P1(I)= RO*L*CF*TEMP
      FP(I)= SQRT(LM)*FPEQ
      FH(I)= 8.736E05*(1/L/CF/CF)**3*TEMP
1000  FAI=FAI+DPH
      IF (MM .GT. 1) GO TO 608
      DFAI1=FAI1*180/3.14159
      DDPH=DPH*180/3.14159
      PRINT 60,DFAI1,DDPH
60    FORMAT (1X,'DFAI1=',F7.2,'DEGREE', 2X, 'INCRE.=',F7.2,'DEGREE')
      WRITE (6,61) (FP(I),FH(I),P1(I),I=1,21)
61    FORMAT (3F12.4)
608   CONTINUE
      IF (INT .LE. 17) GO TO 700
      WRITE (6,69)
69    FORMAT('  INT IS TOO LARGE. INT SHOULD BE 1,3,5,  UPTO 17')
      STOP
700   IST2=INT+1
      IST3=INT+2
      RIC2= FP(INT)**2/FO/(FH(INT)-FO)
      DO 900 J=1,N
      FW=1000
      FI(J)=FO-FW/2+FW*J/N
      F=FI(J)
      RI2= FP(INT)**2/F/(FH(INT)-F)
      RRI= SQRT(RI2/RIC2)
      FRI=SQRT(RRI)
      DO 890 I= INT,21
      GT=F*(FH(I)-F)
      G=FP(I)/SQRT(GT)*P1(I)/3E05
```

```
  890   TY(I)=DPH*G/3
        TT=TY(INT)+TY(21)
        DO 891 I=IST2,20,2
  891   TT=TT+4*TY(I)
        DO 892 I=IST3,19,2
  892   TT=TT+2*TY(I)
        TYL=TT
        CYL=F*TYL
        M1=CYL
        DIF=CYL-M1
        IF (DIF .LE. 0.5) GO TO 895
        DIF=DIF-1
  895   FASE=DIF*2*3.14159
        PD(J)=360*DIF
        SN=SIN(FASE)
        CS=COS(FASE)
        JR=2*J+1
        JI=2*J+2
        ARE=B(JR)
        AIM=B(JI)
        BI(JI)=(-ARE*SN+AIM*CS)/FRI
        BI(JR)=(ARE*CS+AIM*SN )/FRI
        CR(J)= BI(JR)
  900   CI(J)=BI(JI)
        BI(1)=B(1)
        BI(2)= B(2)
        RETURN
        END
C
C
        SUBROUTINE PLOPS(CT,NCL)
C
C
C THIS SUBROUTINE PLOTS SIX VLF PULSES AS FUNCTIONS OF TIME
C
C
        REAL CT(1025)
        INTEGER NCL
        IF(NCL .GT. 1)  GO TO 690
        CALL RAML
        X0=-250
        Y0=2
        GO TO 691
  690   X0=0
        Y0=3
  691   CONTINUE
        CALL SCALE(0.01,0.5,X0,Y0)
        CALL GRID (1,0.,0.,1.,1)
        CALL GRID (3,0.,0.,1.,1)
        CALL GRID (1,-20.,0.,0.2,5)
        CALL GRID (3,-20.,0.,0.2,5)
        IA=-1
        DO 701 I=1,3
        YS=IA-(3-I)*0.1
        CALL CHAR (-50.,YS,0.1,0.1,0.)
        WRITE (20,700) IA
  700   FORMAT(I2)
  701   IA=IA+1
        CALL PLOT (1,0.,0.)
        DO 710 I=1,1025
```

```
      X=I
      CALL PLOT (2,X,CT(I))
710   CONTINUE
      CALL GRID (1,1025.,0.,1.,1)
      CALL GRID (3,1025.,0.,1.,1)
      CALL CHAR (1050.,0.,0.25,0.25,0.)
      WRITE (20,720) NCL
720   FORMAT ('(',I2,' )')
      CALL GRID (2,1000.,0.,100.,10)
      IF (NCL .LT. 6) GO TO 730
      CALL CHAR (1050.,-1.75,0.1,0.1,0.)
      WRITE (20,721)
721   FORMAT ('MS')
      CALL GRID (2,1000.,-1.5,100.,10)
      TIME =0
      X1= -50
      DO 725 J=1,6
      CALL CHAR (X1,-1.75,0.1,0.1,0.)
      WRITE (20,723) TIME
723   FORMAT (F5.0)
      TIME = TIME +100
725   X1=X1+200
      CALL PLOT (1,1500.,0.)
      GO TO 750
730   CALL PLOT (1,0.,0.)
750   CONTINUE
      RETURN
      END
C
C
      SUBROUTINE PDIPO(L, F0,NEQ,DE,NP)
C
C
C THIS SUBROUTINE PLOTS THE GEOMAGNETIC FIELD LINE THROUGH WHICH THE
C VLF PULSES PROPAGATE
C
C
      REAL L,F0,NEQ,XC(49),YC(49),XD(21),YD(21),AN(11)
      INTEGER DE,NP
      PAI=3.14159
C CALCULATE A CIRCLE
      DO 600 I=1,24
      XC(I)= COS(PAI*(I-1)/24)
600   YC(I)= SIN(PAI*(I-1)/24)
      DO 601 I=25,48
      I1=I-24
      XC(I)=-XC(I1)
601   YC(I)=-YC(I1)
      XC(49)=1
      YC(49)=0
C CALCULATE A DIPOLE FIELD LINE
      RT=SQRT(6400*L/6500-1)
      FAI1=ATAN(RT)
      DFP=FAI1/10
      PA =-FAI1
      DO 610 I=1,11
      SI=SIN(PA)
      CI=COS(PA)
      AN(I)=PA*180/PAI
      R=L*CI**2
```

```
      PA=PA+DFP
      XD(I)=R*CI
610   YD(I)=R*SI
      DO 611 I=12,21
      I4=22-I
      XD(I)=XD(I4)
611   YD(I)=-YD(I4)
      CALL RAML
      CALL SCALE (1.,1.,-1., 2.)
      CALL PLOT (-2,1.,0.)
      DO 620 I=1,49
620   CALL PLOT (0,XC(I),YC(I))
      CALL PLOT (1,XD(1),YD(1))
      DO 630 I=2,21
630   CALL PLOT (2,XD(I),YD(I))
      DO 632 I=1,11,2
      CALL PLOT (1,XD(I),YD(I))
      CALL POINT(2)
      I5=(I+1)/2
      X1=XD(I)+I5*0.04-0.2
      Y1=YD(I)-0.5+I5*0.05
      CALL CHAR (X1,Y1,0.15,0.15,0.)
      WRITE (20,631) I5
631   FORMAT ('(',I1,')')
632   CONTINUE
      CALL GRID(0,0.,0.,1.,5)
      CALL CHAR(-1.,-3.,0.15,0.15,0.)
      WRITE (20,633) L,DE,NEQ
633    FORMAT('L= ',F5.2,3X,'DE',I1,' MODEL',2X,'NEQ= ',F7.2,
     1    ' PER C.C.')
      YD1=-3.5
      DO 640 I=1,6
      I6=I*2-1
      AG=AN(I6)
      CALL CHAR(-1.,YD1,0.15,0.15,0.)
      WRITE (20,635) I,AG
635   FORMAT ('LAT. OF LOCATION ',I1,' IS ',F6.2,' DEG')
640   YD1=YD1-0.5
      CALL CHAR(-1.,-6.5,0.15,0.15,0.)
      WRITE (20,641) F0,NP
641   FORMAT ('CARRIER FREQ.= ',F6.1,' HZ',2X,' PULSE LENGTH= ',
     2  I3,' MS')
      RETURN
      END
```

Appendix B

VLF WAVE-PARTICLE INTERACTION IN THE MAGNETOSPHERE

In this appendix, we shall discuss VLF wave particle interaction (WPI) processes in the magnetosphere. It is not our intention to give a complete theory for VLF wave amplification and triggering but, rather, to give the background and rationale for the VLF wave injection experiments related to this report.

The WM wave is assumed to propagate along a static magnetic field line. The electrons travel in the opposite direction. The motion of an electron in a WM wave embedded in a uniform magnetoplasma is studied first. We shall use a simple model to illustrate phase bunching and phase trapping mechanisms, as well as the relationship between bunching time and coherence bandwidth. Phase bunched currents due to $q(V_\perp \times B_w)$ forces will be illustrated schematically. Then, electron motion in a WM wave in the magnetosphere is discussed. We then discuss debunching mechanisms.

According to the Lorentz force law, the electron motion in a WM wave embedded in a homogeneous magnetoplasma is

$$m\dot{\vec{V}} = \vec{F} = -e(\vec{E}_w + \bar{V} \times \bar{B}_w) \tag{B.1}$$

This can be written as [e.g., Bell, 1965; Dysthe, 1971; Matsumoto, 1972]

$$\dot{V}_\parallel = V_\perp \frac{eB_w}{m} \sin \psi \tag{B.2a}$$

$$\dot{V}_\perp = -\left(V_\parallel + \frac{\omega}{k}\right) \frac{eB_w}{m} \sin \psi \tag{B.2b}$$

$$\dot{\psi} = \Omega_o - k\left(V_{\parallel} + \frac{\omega}{k}\right) - \frac{eB_w}{m}\frac{V_{\parallel} + \frac{\omega}{k}}{V_{\perp}} \cos\psi \qquad \text{(B.2c)}$$

where

$\Omega_o = eB_o/m$: electron angular gyrofrequency.

ω = WM wave angular frequency

k = wave number

ψ = angle between $-B_w$ and $V_{\perp}$

We have used the relationship

$$\frac{E_w}{B_w} = \frac{\omega}{k} \qquad \text{(B.3)}$$

The geometry of B_o, $V_{\perp}$, $V_{\parallel}$, k, B_w, and E_w is shown in Fig. B.1.

From Eq. (B.2), we can obtain two constants of motion [Bell, 1965; Dysthe, 1971; Matsumoto, 1972]

$$U^2 = \left(V_{\parallel} - \frac{\omega}{k}\right)^2 + V_{\perp}^2 \qquad \text{(B.4a)}$$

$$X = (V_{\parallel} - V_o)^2 - 2\Omega_w\left(\frac{V_{\perp}}{k}\right) \cos\psi \qquad \text{(B.4b)}$$

where

$$\Omega_w \equiv \frac{eB_w}{m}$$

$V_o = \dfrac{\Omega_o - \omega}{k}$ is called the cyclotron resonance velocity

Equation (B.4a) implies that electron energy is conserved in the frame moving with the wave phase velocity ω/k. It is important to emphasize that wave and electron are traveling in the opposite directions.

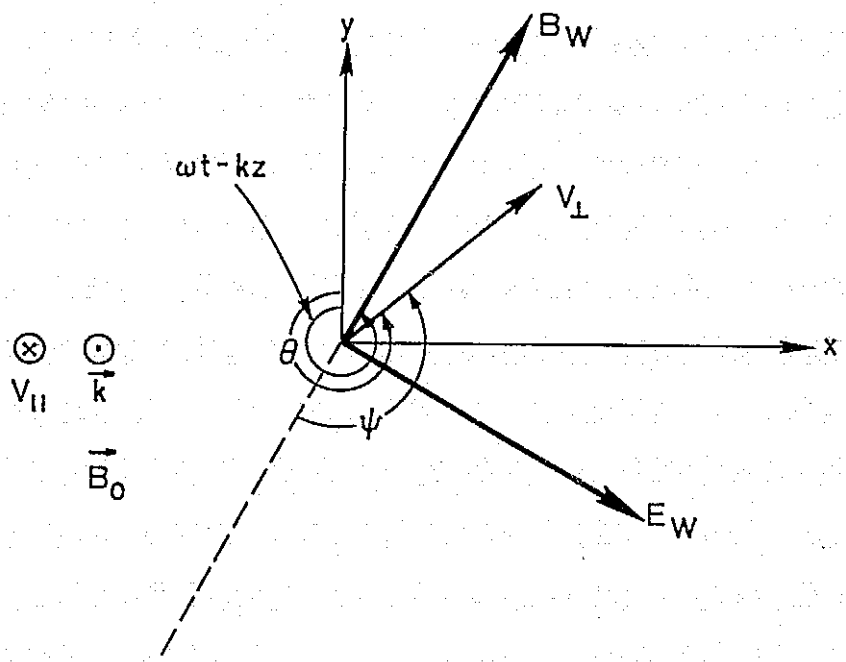

Fig. B.1. CONFIGURATION OF E AND B FIELDS OF A WHISTLER MODE WAVE AND VELOCITY COMPONENTS $V_{||}$ AND $V_\perp$ OF AN ELECTRON IN THE LAB FRAME. The wave and the electron travel in the $\hat{a}_z$ and $-\hat{a}_z$ directions, respectively. ψ is the angle between $-B_W$ and $V_\perp$. $\vec{B}_o$, a constant magnetic field, aligns in the $\hat{a}_z$ direction.

In that frame, there exists only static magnetic fields. The forces applied to electrons are always in directions perpendicular to the electron motions. There is no energy exchange between the wave and the electrons.

The second constant of motion X has been called the "inner Hamiltonian" [Liemohn and Duane, 1976].

In the 3-D phase space where $V_{\parallel}$, $V_{\perp}$, and ψ are chosen as the three orthogonal coordinates, the two constants, U^2 and X, represent two surfaces. A constant U^2 describes a cylindrical surface of radius U, where $U > 0$, centered at $V_{\parallel} = \omega/k$ and $V_{\perp} = 0$. The axis is parallel to the ψ-direction.

A constant X represents a rather complex surface in the phase plane. The cross section of the surface in a plane with constant ψ is a parabola with the axis parallel to the $V_{\perp}$ axis. The vertex is at $[V_o, -(kX/2\Omega_w \cos \psi), \psi]$, and the length of the latus rectum, the chord drawn through the focus and perpendicular to the axis of the parabola, equals $2\Omega_w |\cos \psi|$. The parabola is open towards the positive $V_{\perp}$ direction when $-\pi/2 < \psi < \pi/2$ and towards the negative $V_{\perp}$ direction otherwise. We are interested in the portions of the surface on which $V_{\perp} \geq 0$. Figure B.2 illustrates the loci of the vertices of the parabolas in the phase plane for three cases: $X > 0$, $X = 0$, and $X < 0$. The corresponding surfaces are shown in Fig. B.3.

Given the values of $V_{\parallel}$, $V_{\perp}$, and ψ of an electron at an instant, U^2 and X are defined thereafter. The trajectory of the electron in phase space is the intersection of the two surfaces defined by the values of U^2 and X. Figure B.4 shows several electron trajectories in which we use the same $V_{\perp}$, $V_{\parallel}$ but various ψ for the electrons at an instant to calculate the values of U^2 and X of the electrons. It turns out

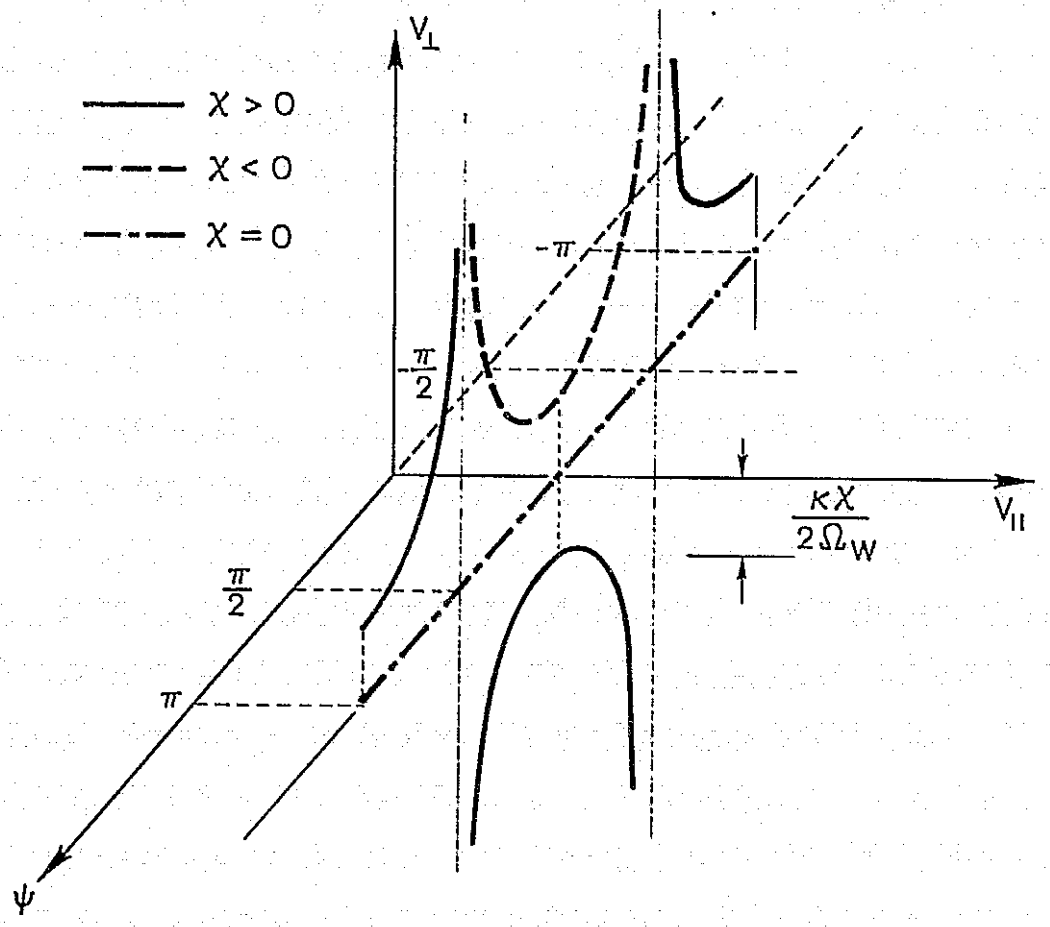

Fig. B.2. THE PHASE-PLANE LOCI OF THE VERTICES OF THE PARABOLAS DEFINED BY EQ. (B.4b).

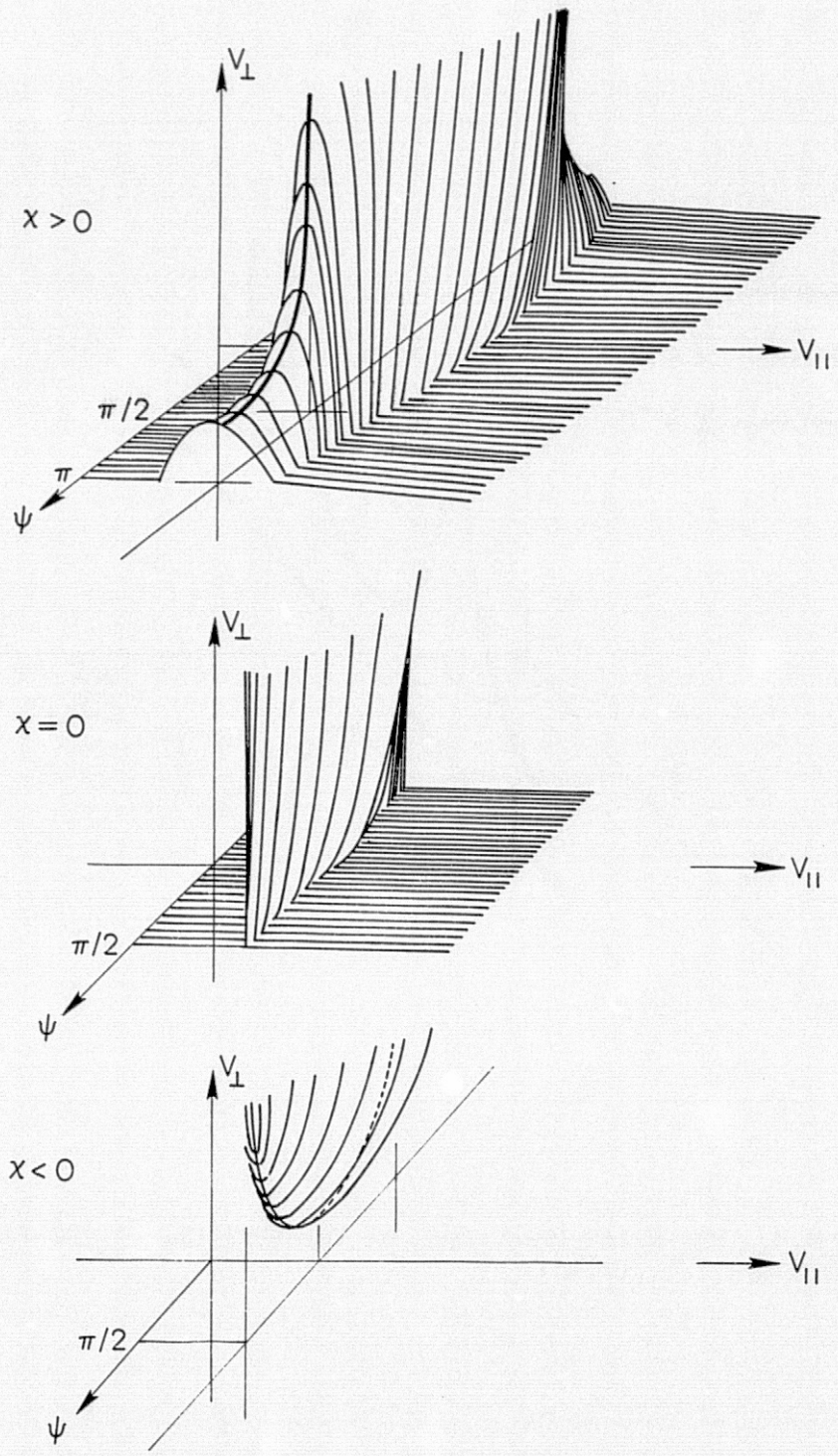

Fig. B.3. THREE SURFACES IN THE PHASE PLANE SPECIFIED RESPECTIVELY BY THREE CONSTANTS X; $X > 0$, $X = 0$, AND $X < 0$.

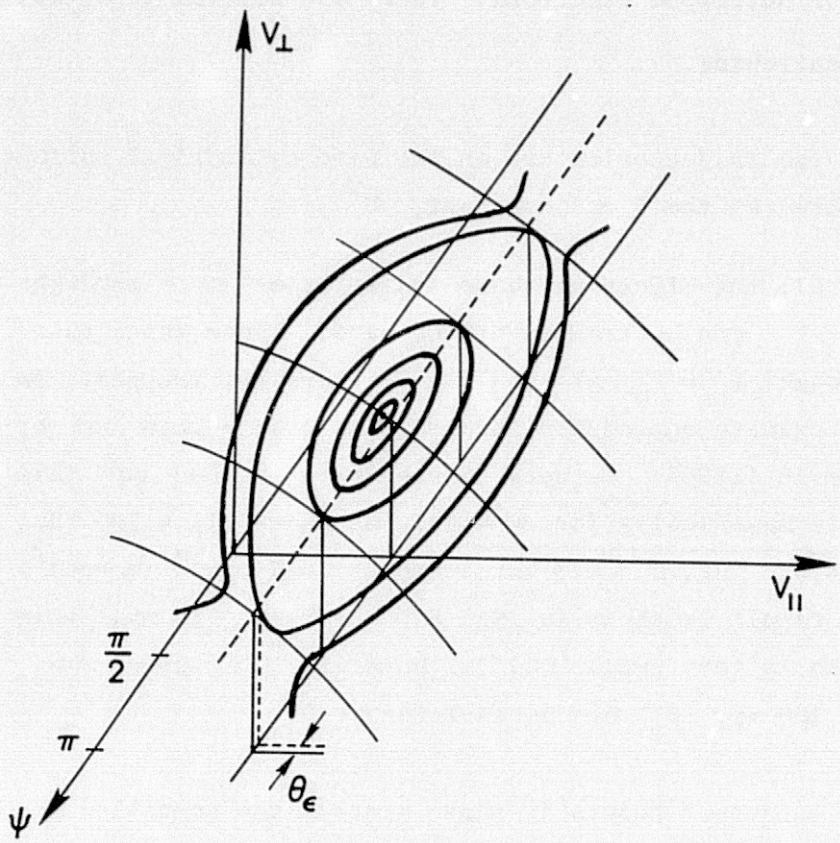

Fig. B.4. TRAPPING CONTOURS IN THE 3-D PHASE SPACE. θ_ϵ is the small angle such that electrons with $V_{||} = V_o$ at $|\psi| > \pi - \theta_\epsilon$ can not be trapped by the wave.

that the value of U^2 is the same but that X has various values. There are two kinds of trajectories. Those with closed contours correspond to the trapped electrons. The others with open contours are the trajectories of untrapped electrons. There are several important features worth mentioning.

(1) All the trajectories are on the same cylindrical surface defined by the first constant, U^2.

(2) Not all the electrons whose trajectories pass through $V_{\parallel} = V_o$ can be trapped by the wave. Those which pass through $V_{\parallel} = V_o$ at $|\psi| > \pi - \theta_\epsilon$ are not trapped. An approximate expression for θ_ϵ has been worked out by Gendrin [1974]. We have independently worked out this angle numerically for a model in which $f_p = 100$ kHz, $f_H = 9.8$ kHz, $f = 4.5$ kHz, and $U^2 = 7 \times 10^{14}$ $(m/sec)^2$. The result is shown in Fig. B.5. For $B_w < 10$ mγ, this angle is very small ($<1°$). However, for waves with $B \sim 100$ mγ, θ_ϵ can be as large as 5°.

There are two important points in phase space: the so-called resonance point at

$$\psi = 0 \quad \text{and} \quad V_{\parallel} = V_r \triangleq V_o - \frac{\Omega_o}{k}\left(\frac{\Omega_w/kV_\perp}{1 + \Omega_w/kV_\perp}\right) \tag{B.5a}$$

and the anti-resonance point at

$$\psi = \pm\pi \quad \text{and} \quad V_{\parallel} = V_{ar} \triangleq V_o + \frac{\Omega_o}{k}\left(\frac{\Omega_w/kV_\perp}{1 - \Omega_w/kV_\perp}\right) \tag{B.5b}$$

They are the solutions of Eq. (B.2) when $\dot{V}_{\parallel} = \dot{V}_\perp = \dot{\psi} = 0$. Furthermore, the resonance point is a stable point and the anti-resonance point is

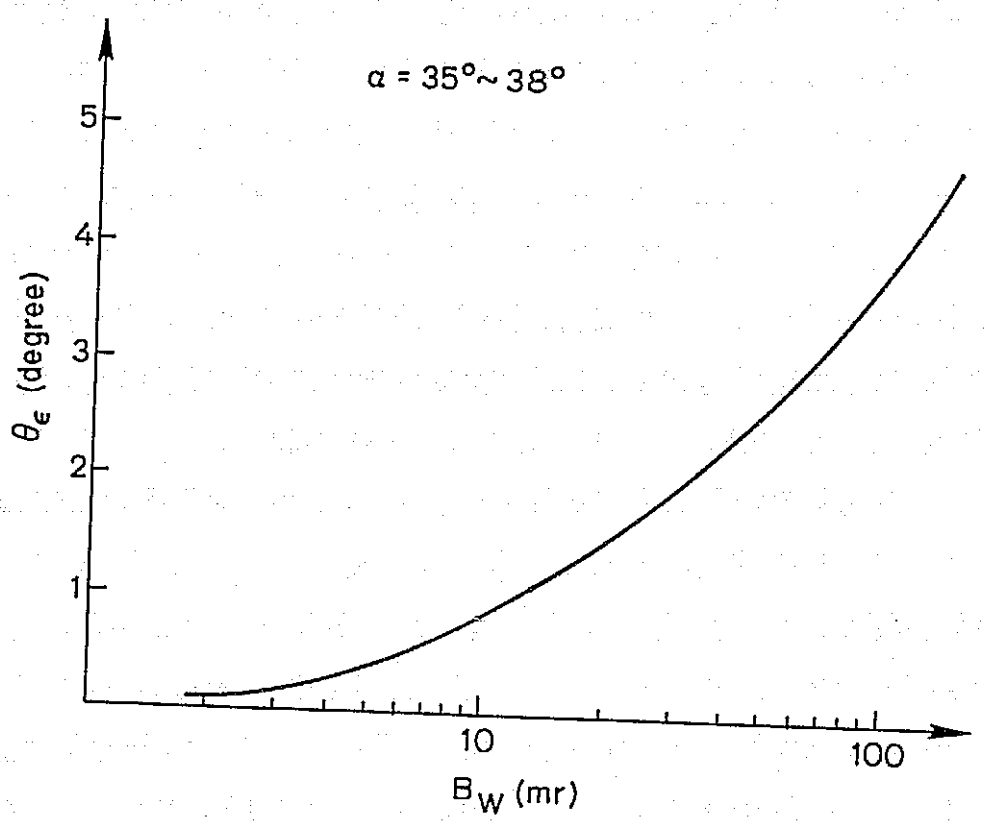

Fig. B.5. THE ANGLE θ_ϵ VS WAVE AMPLITUDE, ASSUMING ELECTRON PITCH ANGLE TO BE ABOUT 35° TO 38°. This angle becomes greater than 4° when the wave is stronger than 100 mγ.

generally an unstable point. The projection of these points, as well as that of electron trajectories on a $V_{\parallel} - \psi$ plane, are shown in Fig. B.6.

It is interesting to point out that an electron which passes through $V_{\parallel} = V_{ar}$, regardless of the value of ψ, is always trapped by the wave. The deviation of V_{ar} from V_o is proportional to B_w for small B_w.

At two extreme conditions, the two resonance velocities V_r and V_{ar} are identical. When $\Omega_w/k \gg V_\perp$,

$$V_r = V_{ar} = -\frac{\omega}{k} = -V_{ph} \tag{B.6}$$

By recollecting that $V_{\parallel}$ and V_{ph} in our convention are in the opposite directions, we realize that Eq. (B.6) is a longitudinal resonance condition similar to (but not) the Landau resonance. When $V_\perp \gg \Omega_w/k$,

$$V_r = V_{ar} = V_o \tag{B.7}$$

Under this condition, V_o is the "real" cyclotron resonance velocity.

The trapping width in $V_{\parallel}$ is not symmetrical about $V_{\parallel} = V_o$. The lower boundary extends further in $V_{\parallel}$ than the upper boundary. But the difference is very small. Figure B.7 shows the difference $\Delta V_{tL} - \Delta V_{tU}$ and the total width $\Delta V_{tL} + \Delta V_{tU}$ for a model in which $f_p = 100$ kHz, $f_H = 9.8$ kHz, $f = 4.5$ kHz, electron pitch angle $\alpha_p \approx 35°$, and $U^2 = 7 \times 10^{14}$ $(m/sec)^2$. When $B_w < 10$ mγ, the ratio of the difference to the total range is less than 1 percent.

A way to obtain an approximate formula for the trapping width is to assume a constant $V_\perp$ instead of using the first constant of motion U^2. From Eq. (B.4b), we can find the value of X for the electrons whose trajectories are on the boundary of the trapping width by setting $V_{\parallel} = V_o$ at $\psi = \pm\pi$, i.e.,

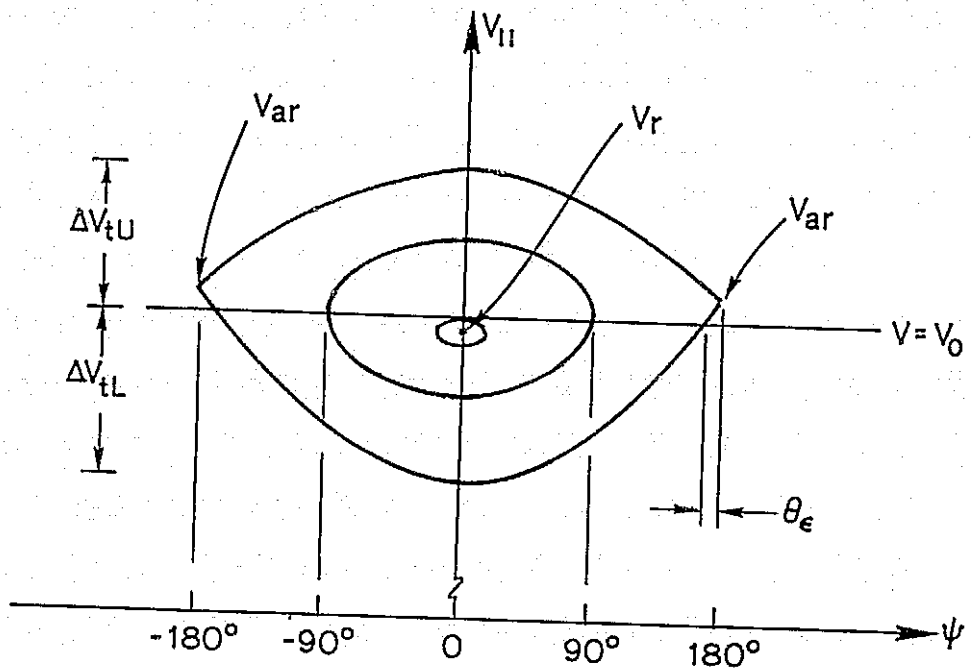

Fig. B.6. THE PROJECTION OF THE 3-D TRAPPING CONTOURS SHOWN IN FIG. B.4 ONTO A $(V_{||} - \psi)$ PLANE. The untrapped contours are not shown. ΔV_{tL} is larger than ΔV_{tU}. The contour passing through the location $V_{||} = V_o$ and $\psi = \pm 90°$ is symmetrical about the line $V_{||} = V_o$.

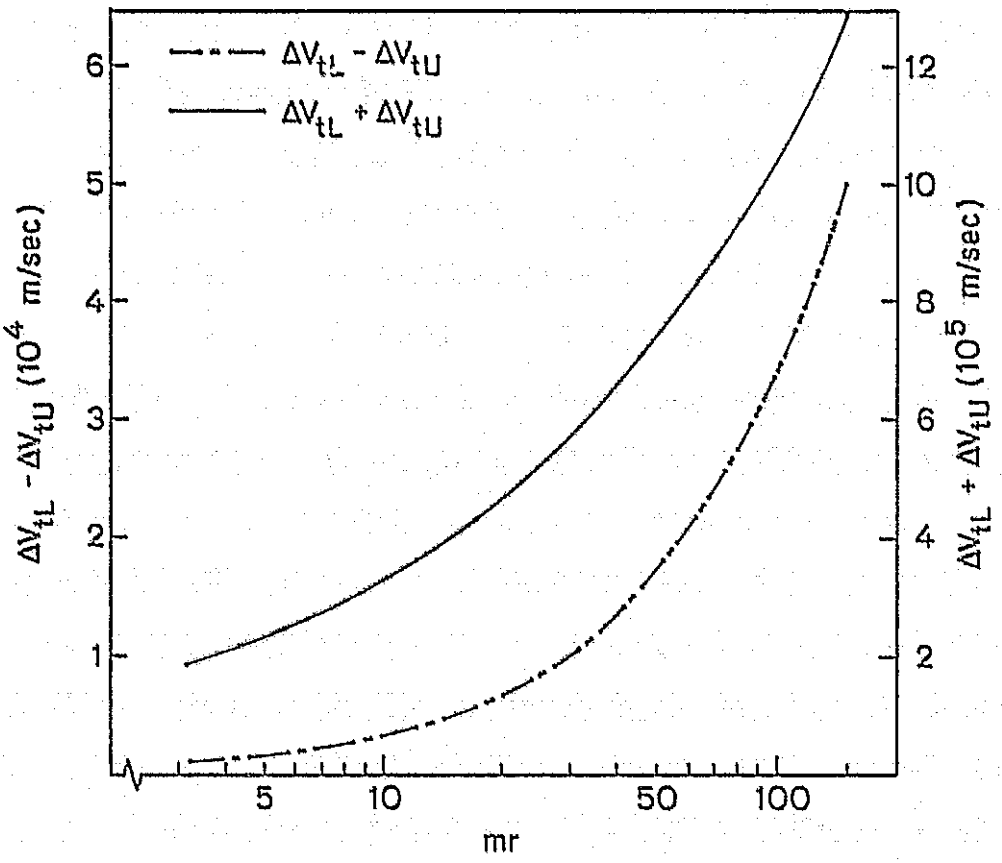

Fig. B.7. THE TOTAL TRAPPING WIDTH $\Delta V_{tU} + \Delta V_{tL}$ AND THE VALUE OF $\Delta V_{tL} - \Delta V_{tU}$ VS WAVE INTENSITY.

$$X_b = 2\Omega_w\left(\frac{V_\perp}{k}\right) \tag{B.8}$$

The values of $V_\parallel$ at $\psi = 0$ under the condition $X = X_b$ are

$$V_\parallel = V_o \pm 2\left(\frac{\Omega_w V_\perp}{k}\right)^{1/2} \tag{B.9}$$

The trapping width in $V_\parallel$ is therefore

$$\Delta V_t = 4\left(\frac{\Omega_w V_\perp}{k}\right)^{1/2} \tag{B.10}$$

Using the same model as the one in Fig. B.7, we plot both ΔV_t of Eq. (B.10) and the "exact" trapping width $\Delta V_{tL} + \Delta V_{tU}$ on Fig. B.8. It is noticed that the discrepancy is very small even for $B_w = 150$ mγ. In general, Eq. (B.10) is a good approximation of the trapping width for electrons with pitch angle greater than 10 degrees and wave intensities less than 150 mγ.

So far, we have discussed only electron motion in a WM wave in a phase space in which the temporal variations are not explicitly shown. It would be beneficial to illustrate the electron motions in a WM wave in the time domain.

We shall start with a brief discussion of the importance of the terms on the right-hand side (RHS) of Eq. (B.2). The first terms in Eqs. (B.2a) and (B.2b) are due to $V_\perp \times B_w$ and $V_\parallel \times B_w$ forces, respectively. The second term in Eq. (B.2b), $(-\omega/k)(eB_w/m)\sin\psi$, is due to the E_w force. In Eq. (B.2c), the first term Ω_o and the second term $k(V_\parallel + \omega/k)$ represent the $V_\perp \times B_o$ (gyration) force and the doppler shift to the wave, respectively. The third term comes from $V_\parallel \times B_w$ and E_w forces.

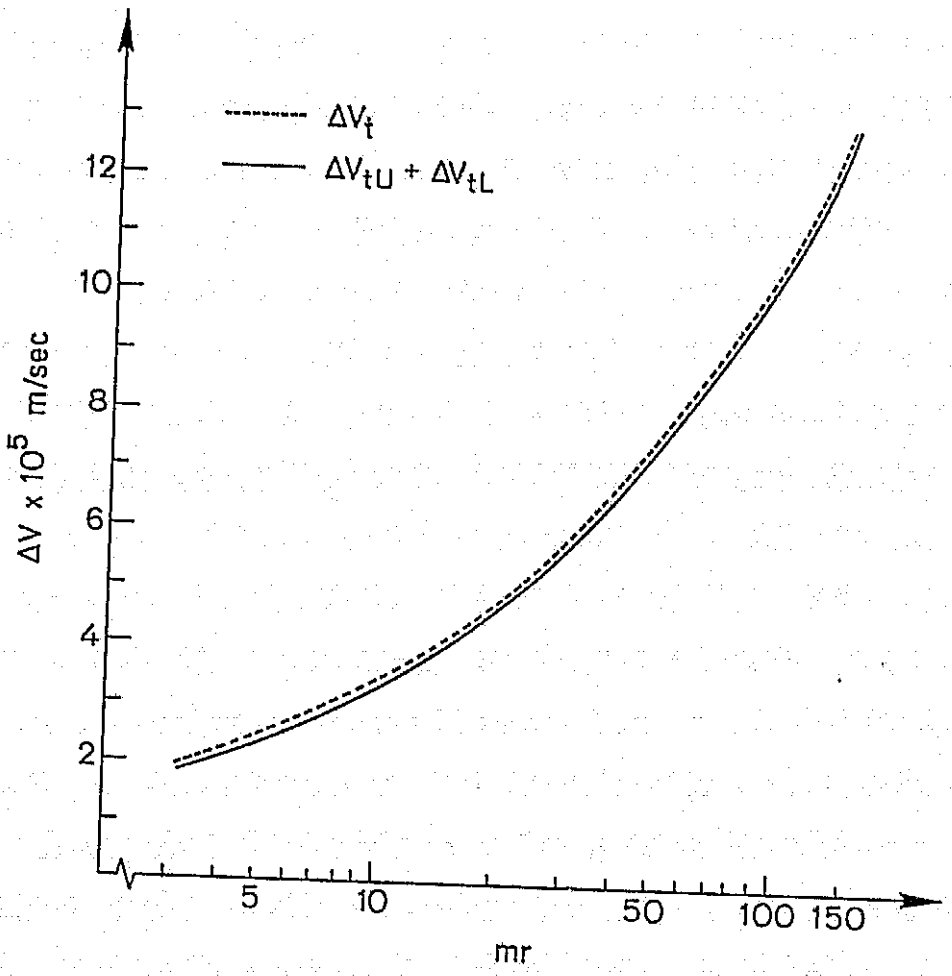

Fig. B.8. THE CALCULATED TRAPPING WIDTH ΔV_t BY EQ. (B.10) AND THE VALUE OF $\Delta V_{tU} + \Delta V_{tL}$ VS WAVE INTENSITY.

Equation (B.2c) can be written as

$$\dot{\psi} = k(V_o - V_{\parallel}) - \frac{eB_w}{m} \frac{V_{\parallel} + \frac{\omega}{k}}{V_{\perp}} \cos \psi \qquad (B.11)$$

The last term is, in fact, the very term that causes V_r and V_{ar} to deviate from V_o. The effect of this term on the trapping region becomes more pronounced near $\psi = 0$ and $\pm\pi$. We have shown earlier that this effect is relatively small for $B_w < 10$ mγ and electron pitch angle >10°. This term will become important when electron pitch angle is small [Dysthe, 1971; Inan, 1977] even in a weak field.

By neglecting the last term in Eq. (B.11), we have

$$\dot{\psi} = k(V_o - V_{\parallel}) \qquad (B.12)$$

We can lump Eqs. (B.2a) and (B.12) together into

$$\ddot{\psi} + \left(\frac{kV_{\perp} eB_w}{m}\right) \sin \psi = 0 \qquad (B.13)$$

This is a pendulum equation with B_w analogous to the gravitation force g and with $m/(ekV_{\perp})$ analogous to the length of the pendulum ℓ. A change in $V_{\perp}$ implies a variation in ℓ. For the purpose of illustration of the $V_{\perp} \times B_w$ phase bunching mechanisms, let us assume a constant $V_{\perp}$. This analogy is illustrated in Fig. B.9. The period of this oscillation for a small angle approximation is T_t, where

$$T_t = \frac{2\pi}{\left(kV_{\perp} \frac{eB_w}{m}\right)^{1/2}} \qquad (B.14a)$$

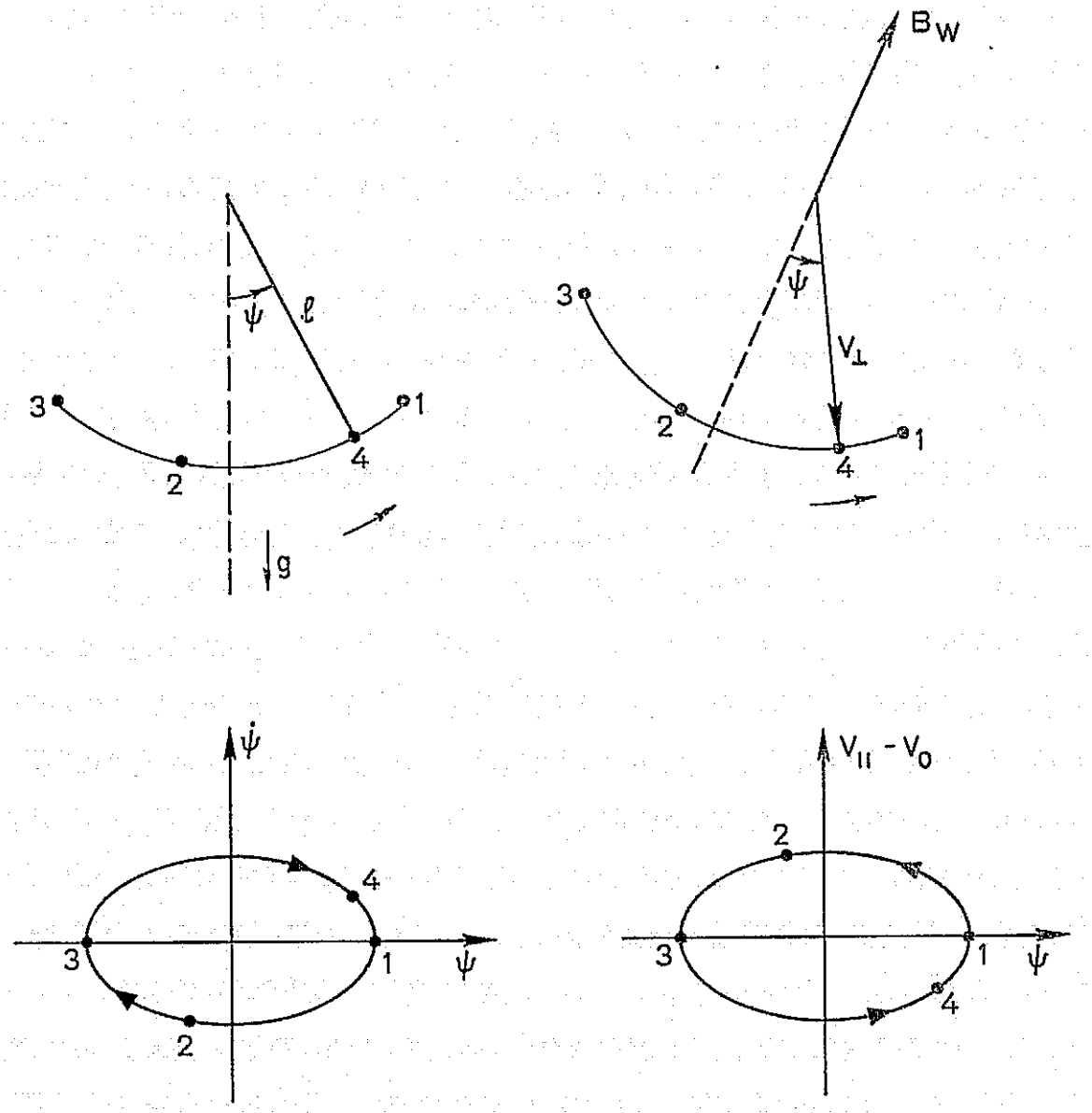

Fig. B.9. AN ANALOG OF AN ELECTRON MOTION IN A WM WAVE TO A PENDULUM MOTION IN THE GRAVITATIONAL FIELD. The time domain motions are shown in the upper panel, and the corresponding phase domain motions are in the lower panels.

T_t is the trapping period for small phase angle electrons.

As the pendulum swings from Locations 1, 2, 3, to 4, it executes a trajectory in the phase plane $(\dot{\psi},\psi)$ as indicated by 1, 2, 3, and 4. Similarly, as an electron in a WM wave with a phase angle ψ changes from positions 1, 2, 3, to 4 in the time domain, its position in the phase plane $(V_{\parallel},\psi)$ is moving from 1, 2, 3, to 4, as indicated in Fig. B.9. The condition $V_{\parallel} = V_o$ implies $\dot{\psi} = 0$ and occurs only at the two locations where $|\psi|$ = maximum. In this example, $V_{\parallel} = V_o$ occurs only at Locations 1 and 3.

Without any other external force, the pendulum will exercise a periodic (but not sinusoidal) oscillation in time if the condition $\dot{\psi} = 0$ occurs within $-180° < \psi < 180°$. Otherwise, it will rotate. Similarly, the electron is oscillating or rotating if the condition $V_{\parallel} = V_o$ can or cannot be met within $-180° < \psi < 180°$. The electron oscillating in time has a closed contour in the phase plane and hence is trapped by the WM wave. The one rotating in time has an open contour and hence is untrapped by the wave.

For those trapped electrons with large phase angle ψ_R at $V_{\parallel} = V_o$, the trapping period depends on the value of ψ_R and is [e.g., Matsumoto, 1972]

$$T_t(\psi_R) = \frac{4}{(kV_{\perp}\Omega_w)^{1/2}} K\left(\sin\frac{\psi_R}{2}\right) \qquad \text{(B.14b)}$$

where

$$K(X) = \int_0^{\pi/2} \frac{d\theta}{\sqrt{1 - x^2 \sin^2\theta}}$$

$K(X)$ is the complete elliptic integral of the first kind. $K(\sin \psi_R/2)$, as a function of ψ_R, is plotted in Fig. B.10. For electrons with $\psi_R = \pm\pi$ at $V_{\parallel} = V_o$, the trapping period is infinite.

We shall recall that the period of a pendulum is almost constant at the value $2\pi\sqrt{\ell/g}$ for reasonably small angles ψ (say, 15°). This is the key to understanding the phase bunching mechanisms. Suppose there are many electrons initially at $V_{\parallel} = V_o$ but at various phase angles. Their $V_{\perp}$'s are the same. Initially, there is no transverse current, as shown in Fig. B.11. Corresponding to the analogy of pendulums, the pendulums are identical and are at various locations but at rest $(\dot{\psi} = 0)$ initially. As time goes on, all the pendulums converge towards $\psi = 0$. At one quarter of the period, $\pi/2\sqrt{\ell/g}$, the pendulums initially a small ψ are in alignment with each other at $\psi = 0$. In the wave-electron system, this phase angle convergence mechanism is called phase bunching. It is this process that creates a transverse current in the direction of B_w, as shown in Fig. B.11. The bunching time T_b is defined as a quarter of T_t.

$$T_b = \frac{\pi}{2}\left(\frac{m}{eB_w kV_{\perp}}\right)^{1/2} \tag{B.15}$$

It is interesting to show that T_b^{-1} is the corresponding frequency range of the trapping width, which we shall call the coherence bandwidth

$$\Delta f_{CB} \triangleq \frac{k}{2\pi}\Delta V_t = \frac{2}{\pi}(kV_{\perp}\Omega_w)^{1/2} = T_b^{-1} \tag{B.16}$$

It is important to point out that these electrons at the same location in space initially will not arrive at another location later simultaneously because their $V_{\parallel}$'s are not identical (due to different $V_{\perp} \times B$

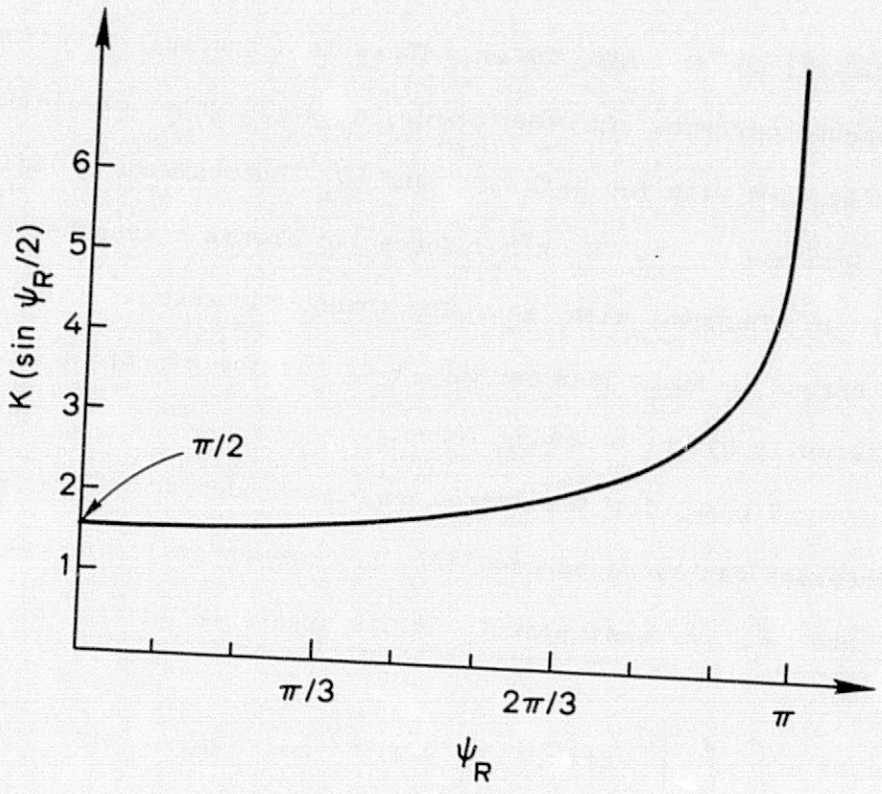

Fig. B.10. PLOT OF THE VALUE OF K(sin $\psi_R/2$) IN EQ. (B.14b) VS ψ_R.

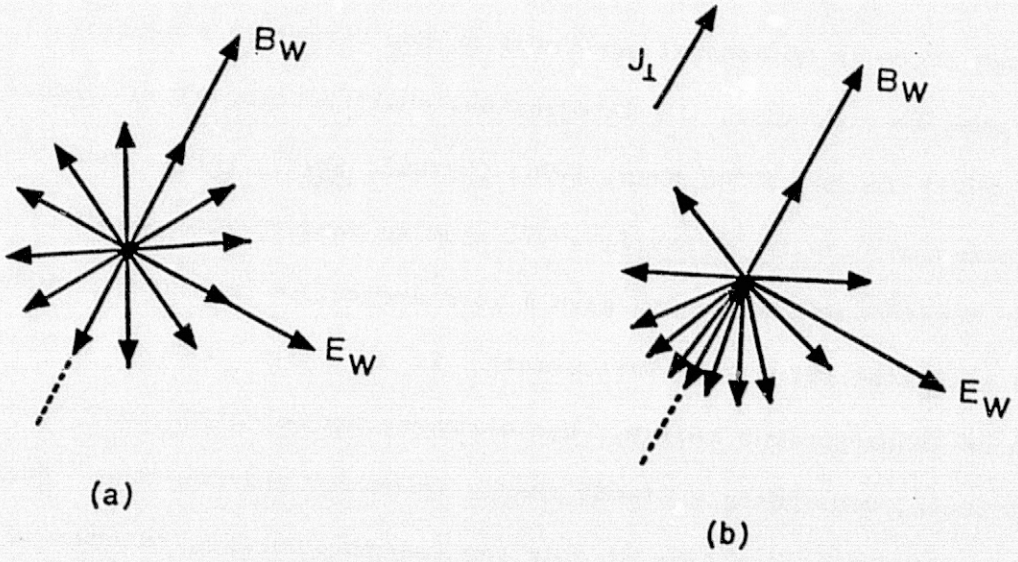

Fig. B.11. ILLUSTRATION OF PHASE BUNCHING MECHANISM. See text.

forces) [Helliwell and Crystal, 1973]. There is a spatial spreading in the phase-bunched current. In other words, a single sheet of electrons at the same location with the same $V_{\parallel}$ and $V_{\perp}$ but various ψ initially can be phase-bunched by the $V_{\perp} \times B_w$ forces to create a transverse current which is in alignment with B_w. The transverse current is not localized but spread in space because the $V_{\parallel}$'s of the electrons have been altered differently by the bunching forces.

For a general case, the transverse current produced by the phase-bunching processes can be decomposed into two components: J_1 parallel to the B_w and J_2 perpendicular to it, as indicated in Fig. B.12.

$$J_1(\bar{x},t) = \int_{V_{\parallel}} \int_{V_{\perp}} \int_{-\pi}^{\pi} qf(\bar{x},V_{\parallel},V_{\perp},\psi,t)\, V_{\perp}^2 \cos\psi\, d\psi\, dV_{\perp}\, dV_{\parallel} \qquad \text{(B.17a)}$$

$$J_2(\bar{x},t) = \int_{V_{\parallel}} \int_{V_{\perp}} \int_{-\pi}^{\pi} qf(\bar{x},V_{\parallel},V_{\perp},\psi,t)\, V_{\perp}^2 \sin\psi\, d\psi\, dV_{\perp}\, dV_{\parallel} \qquad \text{(B.17b)}$$

Even though there is no general agreement on how large the ranges of $V_{\parallel}$ and $V_{\perp}$ must be over which the integrations shall be carried out [Sudan and Ott, 1971; Dysthe, 1971; Nunn, 1974; Crystal, 1974], the latest computer simulation results [Crystal, 1977] seem to confirm that integrating only over the trapping width can give a good indication of the magnitude of these simulated currents. Furthermore, it is shown in Nunn [1971] that, in an inhomogeneous medium, "cyclotron resonant electrons may become stably trapped, undergoing a steady change in energy and momentum. Where wave-particle-interaction time exceeds one trapping period, bunches of stably trapped particles completely dominate interaction with the wave."

We believe that both trapped and nearly-trapped electrons are important to the wave growth. However, since trapping is such a simple idea that can give us good indications of the stimulated currents and, since we are interested in a qualitative answer at the moment, we shall consider the trapped electrons only from now on.

As to how these currents contribute to wave amplification, there are different opinions, too. In the model of Helliwell and Crystal [1973], the current J_1 is treated as a source current which radiates a new field. The new field combines with the old wave, resulting in net wave growth. Frequency variations come from the inhomogeneity in the geomagnetic field lines. In Dysthe [1971] and Nunn [1974], a gradient in electron $V_{\parallel}$ distributions is required to produce J_2. Since J_2 is aligned with E_w, there is energy exchange $(J_2 \cdot E_w)$ between the wave and the electrons. J_1 serves as the source of frequency variations in both homogeneous and inhomogeneous cases.

The inhomogeneity of the geomagnetic field in the magnetosphere is important in WPI processes. For instance, the inhomogeneity acts on the electrons like an external torque, pushing the stable point in ψ from $\psi_o = 0°$ to other values, deforming electron trajectories in phase spaces, and reducing the trapping width. Far away from the equator, the inhomogeneity is so large that trapping becomes impossible [Dysthe, 1971; Nunn, 1974] for CW waves with reasonable amplitudes. More quantitative arguments on when trapping is possible will be discussed later in this section.

The inhomogeneity forces in the equations of motion are modeled [e.g., Dysthe, 1971] as

$$\bar{F}_{\parallel} = \frac{mV_{\perp}^2}{2B} \frac{\partial B}{\partial z} \tag{B.18a}$$

$$\bar{F}_{\parallel} = -\frac{mV_{\perp} V_{\parallel}}{2B} \frac{\partial B}{\partial z} \tag{B.18b}$$

They are derived from the first adiabatic constant and the Gauss law $\nabla \cdot \bar{B} = 0$. It has been assumed that the spatial variations in B are very small over a distance of the order of the electron gyro-radius. The forces have been averaged over a gyro-radius. This is a widely-used model [Dysthe, 1971; Nunn, 1971; Inan, 1977].

Electron motion in a WM wave in the magnetosphere, therefore, can be modeled as [e.g., Dysthe, 1970]

$$\dot{V}_{\parallel} = V_{\perp} \frac{eB_w}{m} \sin \psi + \frac{V_{\perp}^2}{2B} \frac{\partial B}{\partial z} \tag{B.19a}$$

$$\dot{V}_{\perp} = -\left(V_{\parallel} + \frac{\omega}{k}\right) \frac{eB_w}{m} \sin \psi - \frac{V_{\perp} V_{\parallel}}{2B} \frac{\partial B}{\partial z} \tag{B.19b}$$

$$\dot{\psi} = \Omega - k\left(V_{\parallel} + \frac{\omega}{k}\right) - \frac{eB_w}{m} \frac{V_{\parallel} + \frac{\omega}{k}}{V_{\perp}} \cos \psi \tag{B.19c}$$

where

$\Omega = eB/m$

R_E = earth radius

L = McIlwain's L parameter

We have assumed that $z = 0$ is at the equator and that the wave and electrons travel in $+z$ and $-z$ directions, respectively. The curvature of the geomagnetic fields is not included in the formulation. The geomagnetic field near the equator can be assumed as

$$B = B_o\left[1 + \frac{9}{2}\left(\frac{z}{LR_E}\right)^2\right]\hat{a}_z \qquad (B.20)$$

Numerical solutions of these equations have been calculated [Inan, 1977] for various values of B_w.

Equation (B.19c) is the same as Eq. (B.2c). By the same argument given before, for electrons with a pitch angle greater than, say, 10 degrees, the pendulum type of equation is obtained as follows:

$$\dot{\psi} \approx \Omega - k\left(V_{\parallel} + \frac{\omega}{k}\right) \qquad (B.21)$$

By differentiating Eq. (B.21), we have

$$\ddot{\psi} = \dot{\Omega} - \dot{k}V_{\parallel} - k\dot{V}_{\parallel} \qquad (B.22)$$

We have assumed a constant frequency signal so that $\dot{\omega} = 0$. From the WM dispersion relation, it can be shown that

$$\dot{k} = \frac{k\dot{\Omega}}{2(\Omega - \omega)} \qquad (B.23)$$

Substituting (B.19a) and (B.23) into (B.22), we have

$$\ddot{\psi} + kV_{\perp}\frac{eB_w}{m}\sin\psi = -\left[\frac{kV_{\perp}}{2\Omega} + V_{\parallel}\left(1 + \frac{kV_{\parallel}}{2(\Omega - \omega)}\right)\right]\frac{\partial\Omega}{\partial z} \qquad (B.24)$$

We have used

$$\frac{1}{B}\frac{\partial B}{\partial z} = \frac{1}{\Omega}\frac{\partial\Omega}{\partial z} \qquad (B.25)$$

and

$$\dot{\Omega} \cong -V_{\parallel}\frac{\partial\Omega}{\partial z} \qquad (B.26)$$

Let us define the RHS of (B.24) as τ/m, i.e.,

$$\tau/m \triangleq -\left[\frac{kV_\perp^2}{2\Omega} + V_\parallel\left(1 + \frac{kV_\parallel}{2(\Omega - \omega)}\right)\right]\frac{\partial\Omega}{\partial z} \tag{B.27}$$

The inhomogeneity works as an external torque τ which is a function of position. When $|\tau| \leq eB_w kV_\perp$, we can define an angle ψ_o so that

$$\sin\psi_o = \tau/eB_w kV_\perp \tag{B.28}$$

Equation (2.22) can then be written as

$$\ddot{\psi} + \frac{kV_\perp eB_w}{m}[\sin\psi - \sin\psi_o] = 0 \tag{B.29}$$

At $\psi = \psi_o$, $\ddot{\psi} = 0$. The inhomogeneity force has shifted the stable point of the pendulum from $\psi = 0$ to ψ_o. Electrons are still trapped by the wave but they oscillate about $\psi = \psi_o$ instead of about $\psi = 0$ when τ varies sufficiently slowly for a distance of the order of $V_\parallel \cdot T_t$, where T_t is the trapping period. The trapping width is reduced, too [Dysthe, 1971; Nunn, 1974]. On the other hand, when $|\tau| > eB_w kV_\perp$, trapping is impossible.

At the end of the triggering wave, assuming that the stimulated currents are not strong enough to maintain a self-sustained system, the organized electrons will undergo a phase-mixing process which reduces transverse currents. In a homogeneous model, this process occurs because of a finite $V_\parallel$ spreading in the organized electrons. Let us assume that only trapped electrons are important in the bunching processes. At the end of a wave train where $t = 0$, B_w disappears. From Eq. (B.13) for $t \geq 0$,

$$\ddot{\psi} = 0 \tag{B.30}$$

Integrating twice, we have

$$\psi = At + B \tag{B.31}$$

where A, B are constants to be determined by the initial values of $\dot{\psi}$ and ψ at $t = 0$.

From Eq. (B.12),

$$\dot{\psi} = k(V_o - V_{||}) \tag{B.32}$$

Thus,

$$\psi = K(V_o - V_{||})\ t + B \tag{B.33}$$

The trapping range in the phase plane is deformed, as shown in Fig. B.13. Note, the $V_{||}$'s do not change but the ψ's do. The electrons eventually will be totally phase-mixed. The drift in ψ is a linear function $(V_o - V_{||})t$. The further away from V_o, the larger the drift in ψ. The largest difference in ψ-drift is between the electrons with $V_{||} = V_o \pm \Delta V_t/2$ and can be written as

$$\Delta\phi_m(t) = -2\pi\Delta f_{CB}\, t \tag{B.34}$$

The debunching time is defined as the time required to randomize the organized electron. It can be shown, when $\Delta\phi_m(t) = \pm 2\pi$, the transverse currents totally disappear in this case. Thus, the debunching time T_D can be obtained as

$$T_D = \frac{1}{\Delta f_{CB}} = T_b \tag{B.35}$$

In an inhomogeneous model, in addition to this finite spread of $V_{||}$'s that causes phase-mixing, there is another adiabatic force which helps

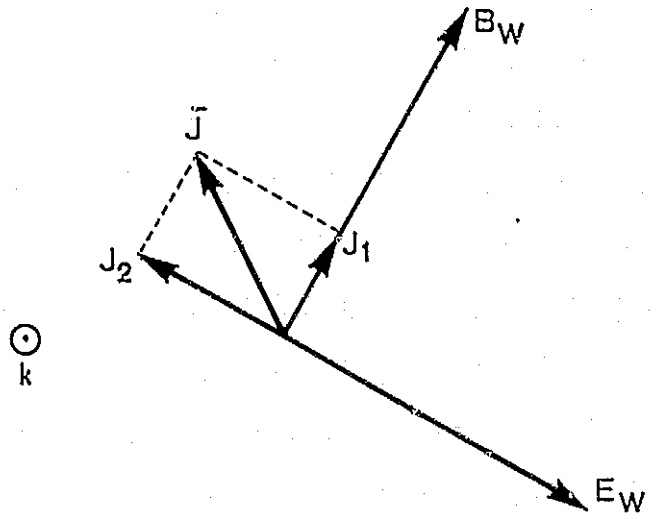

Fig. B.12. CONFIGURATION OF J_1, J_2 OF EQS. (B.17a) AND (B.17b).

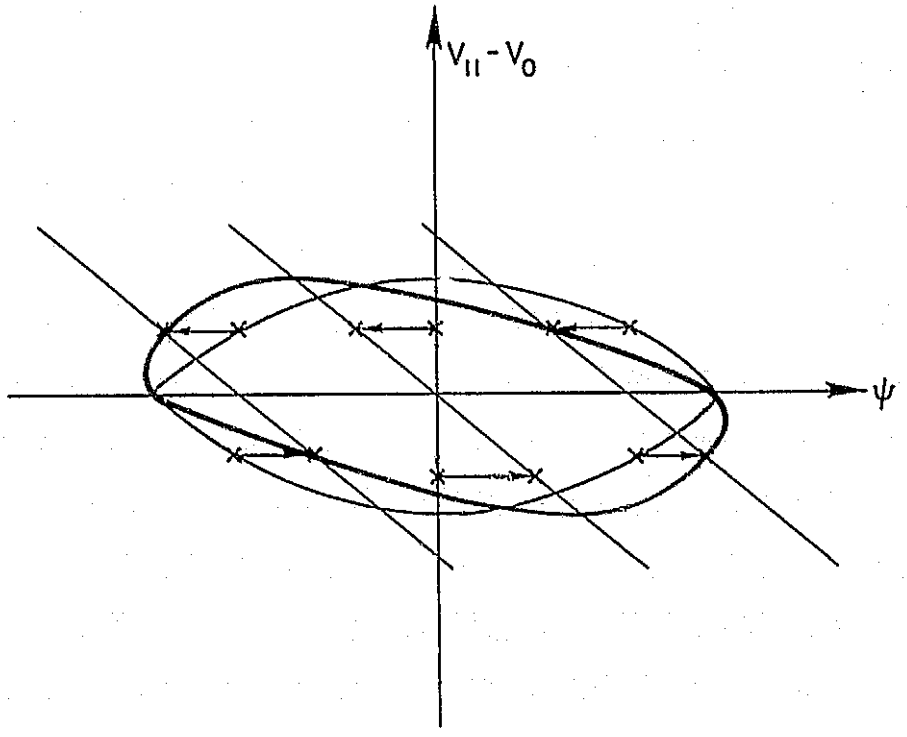

Fig. B.13. VARIATION OF A TRAPPED REGION AT THE END OF TRIGGERING WAVE IN A HOMOGENEOUS MAGNETOPLASMA.

the phase mixing. As can be seen from Eq. (B.24), various values of either $V_\perp$ or $V_\parallel$ will produce different external torque τ. This causes differential drifts in ψ to produce phase-mixing. Thus, in an inhomogeneous media, the debunching time should be smaller than T_D.

Appendix C

DERIVATION OF SIDEBAND REPRESENTATION OF FSK WAVES

In this appendix, we shall derive the sideband representations of the FSK waves analytically. The sideband amplitudes, frequencies, and phases will be given quantitatively.

An FSK wave (except the calibration wave) consists of a sequence of RF pulses, each lasting τ_s msec, alternating between two carriers separated by Δf. It can be viewed as two pulse trains: one at the carrier f_1 and the other at $f_2 = f_1 - \Delta f$. Each of the pulse trains is a square-wave modulated sine wave consisting of a sequence of RF pulses and gaps in between. All the pulses and the gaps have the same duration τ_s. The phase difference between two successive pulses $\Delta\phi_w$ equals $2\pi\Delta f\tau_s$ which creates either an in-phase or an anti-phase condition.

Analytically, the FSK wave can be written as

$$W'_{o,\pi}(t) = C\prod\left(t - \frac{1}{2}\right)\left[M_{o,\pi}(t)\sin(2\pi f_1 t + \phi_o) + \beta M_{o,\pi}(t)\sin(2\pi f_2 t + \phi_i + \phi_o)\right] \qquad (C.1)$$

where $M_{o,\pi}(t)$ are the square wave trains shown in Fig. C.1. The subscripts o and π denote the 0- and π-conditions, respectively. $M_{o,\pi}(t)$ extends from $t = -\infty$ to $+\infty$. C and $C\beta$ are the wave intensities of f_1 and f_2, respectively. The inherent limitations on the transmitting system at Siple cause β to be different from unity and $\beta < 1$. The deviation usually is small when $\Delta f \ll f_1$. $\prod(t)$ is a square pulse with a unit height and one-s duration centered at $t = 0$. ϕ_o is the initial phase angle of the carrier at f_1 and is constant. ϕ_i equals $2\pi\Delta f\tau_s$.

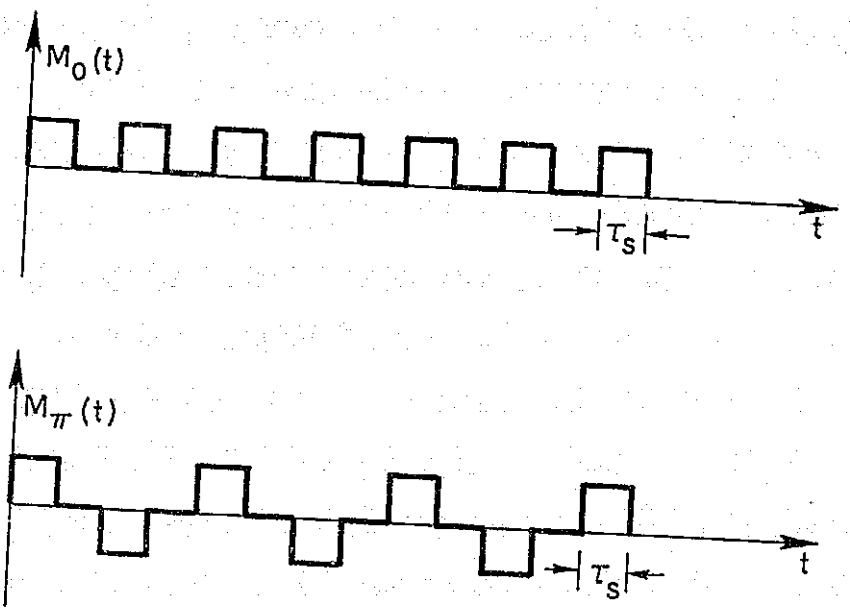

Fig. C.1. PLOT OF THE FUNCTIONS $M_o(t)$, $M_\pi(t)$ OF EQ. (C.2b) VS TIME. τ_s is the small pulse length.

Without losing generality, we can assume $\phi_o = 0$ and $C = 1$. Then, Eq. (C.1) can be written as

$$W'_{o,\pi}(t) = \prod\left(t - \frac{1}{2}\right) W_{o,\pi}(t) \qquad \text{(C.2a)}$$

where

$$W_{o,\pi}(t) = M_{o,\pi}(t) \sin 2\pi f_1 t + \beta M_{o,\pi}(t - \tau_s) \sin (2\pi f_2 t + \phi_i) \qquad \text{(C.2b)}$$

The Fourier transform of $W_{o,\pi}(t)$ is defined as

$$A_{o,\pi}(f) \triangleq \mathcal{F}\left[W_{o,\pi}(t)\right] = \int_{-\infty}^{\infty} W_{o,\pi}(t)\, e^{-i2\pi ft}\, dt \qquad \text{(C.3a)}$$

$$W_{o,\pi}(t) \triangleq \mathcal{F}^{-1}\left[A_{o,\pi}(f)\right] = \int_{-\infty}^{\infty} A_{o,\pi}(f)\, e^{i2\pi ft}\, df \qquad \text{(C.3b)}$$

$A_{o,\pi}(f)$ can be written as [e.g., Bracewell, 1965]

$$A_{o,\pi}(f) = m_{o,\pi}(f) * \frac{1}{2i}\left[\delta(f - f_1) - \delta(f + f_1)\right]$$

$$+ \beta e^{-i2\pi f\tau_s}\, m_{o,\pi}(f) * \frac{e^{-i\phi_i}}{2i}\left[\delta(f - f_2) - \delta(f + f_2)\right] \qquad \text{(C.4)}$$

where

$$m_{o,\pi}(f) = \int_{-\infty}^{\infty} M_{o,\pi}(t)\, e^{-i2\pi ft}\, dt$$

$\delta(\cdot)$ = Dirac delta function

$*$ = convolution

The amplitudes and phases of $m_{o,\pi}(f)$ and $m_{o,\pi}\, e^{-i2\pi f\tau_s}$ are shown in Figs. C.2 and C.3. They are the base-band spectrum of $W_{o,\pi}(t)$ consisting of discrete spikes separated at multiples of $(2\tau_s)^{-1}$. For example, the spacings are at multiples of 50 Hz when $\tau_s = 10$ msec.

The delta functions shift the whole base-band spectrum to the appropriate frequency bands centered at $\pm f_1$ and $\pm f_2$. In general, f_1 and f_2 are in kHz ranges; the spikes shifted from the base-band toward the positive, and those towards the negative frequency ranges do not interfere with each other. Furthermore, because the transmitted signals are real signals, the part of the spectrum on the positive and that on the negative frequencies are conjugate to each other.

That is,

$$A(f) = A_+(f) + A_-(f) \tag{C.5a}$$

and

$$A_-(f) = A_+^*(-f) \tag{C.5b}$$

where

$$A_+(f) = m_{o,\pi}(f) * \frac{1}{2i}\,\delta(f - f_1) + \beta e^{-i2\pi f\tau_s}\, m_{o,\pi}(f) * \frac{1}{2i}\, e^{-i\phi_i}\,\delta(f - f_2) \tag{C.5c}$$

Figure C.4 shows the amplitudes and phases of $A_+(f)$ for the following two cases: (a) $\tau_s = 10$ msec and $\Delta f = 100$ Hz, and (b) $\tau_s = 20$ ms and $\Delta f = 100$ Hz. Both are 0-waves. Figure C.5 shows the following two: (a) $\tau_s = 10$ ms and $\Delta f = 150$ Hz, and (b) $\tau_s = 20$ ms and $\Delta f = 125$ Hz. Both are π-waves. β has been assumed to be unity for simplicity. The frequency spacing between the spikes for the signals with $\tau_s = 10$ and 20 ms are multiples of 50 and 25 Hz, respectively. The spectrum $A_+(f)$ is symmetrical about the frequency at $(f_1 + f_2)/2$.

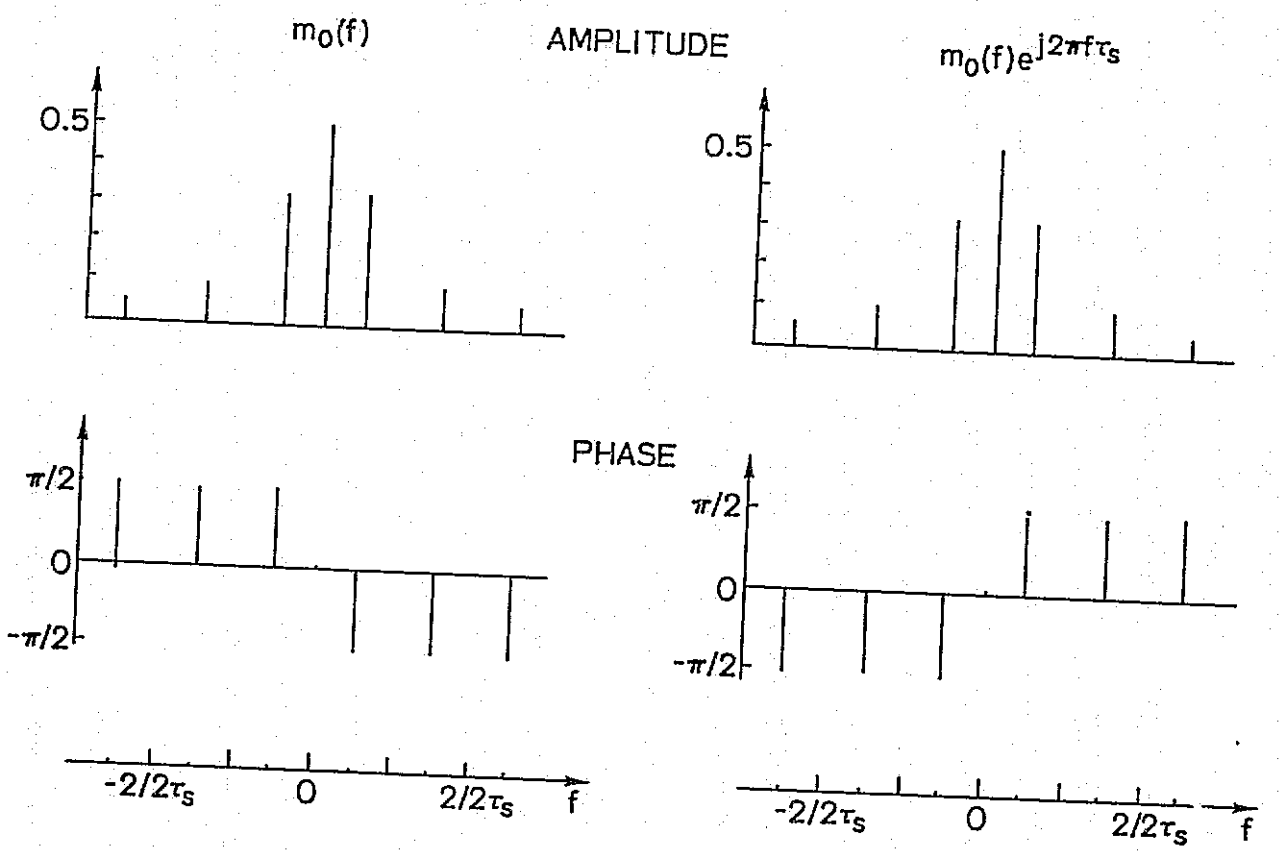

Fig. C.2. THE CORRESPONDING SPECTRUM $m_o(f)$ OF $M_o(t)$ AND $m_o(f)\, e^{i2\pi f\tau_s}$ IN THE FREQUENCY DOMAIN.

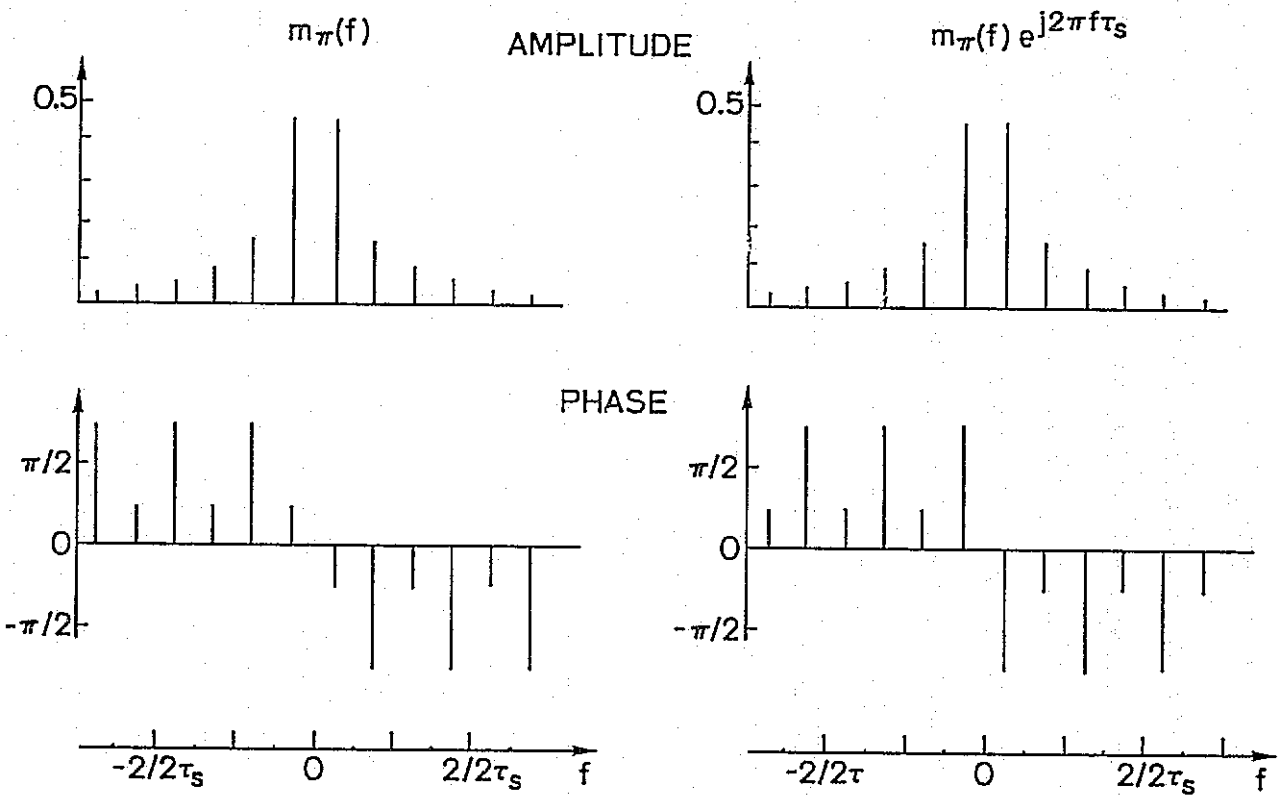

Fig. C.3. THE CORRESPONDING SPECTRUM $m_\pi(f)$ OF $M_\pi(t)$ AND $m_\pi(f)\, e^{i2\pi f\tau_s}$ IN THE FREQUENCY DOMAIN.

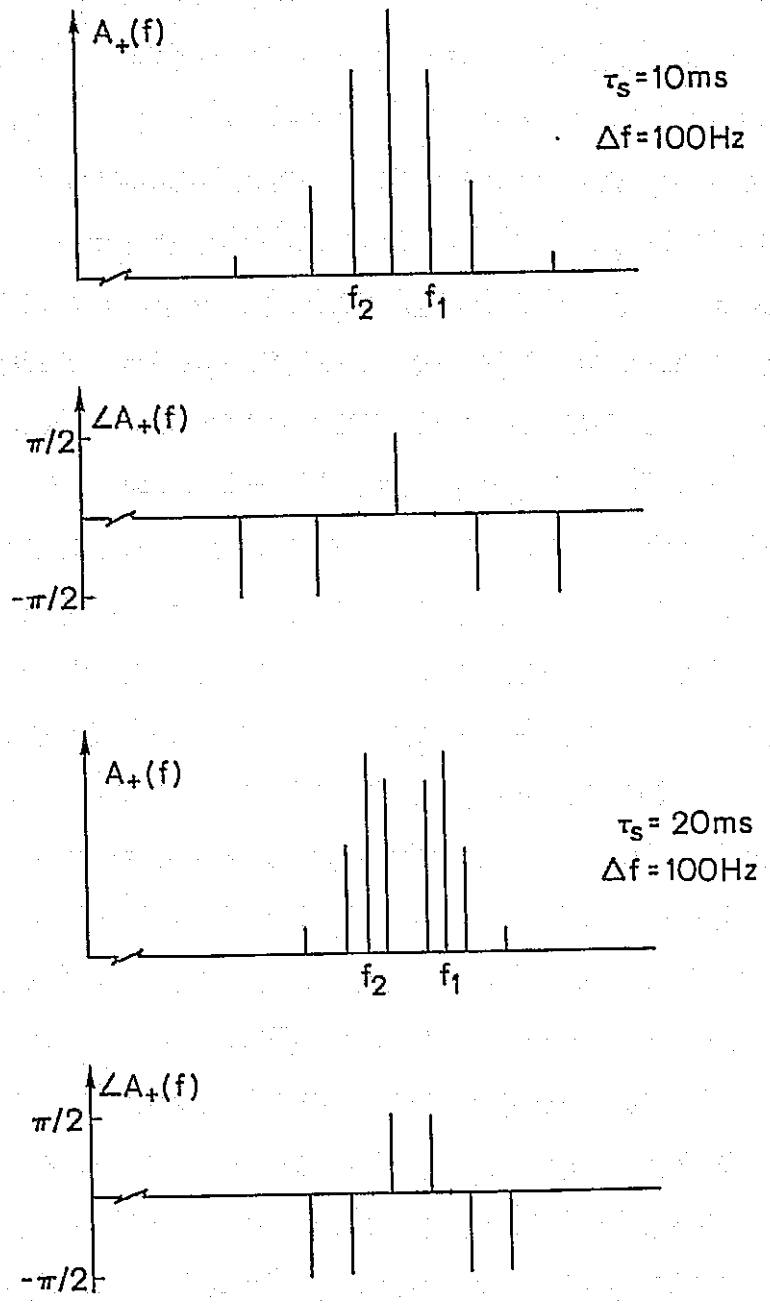

Fig. C.4. PLOTS OF $A_+(f)$ OF EQ. (C.5c) FOR TWO O-WAVE CASES: τ_s = 10 ms, Δf = 100 Hz AND τ_s = 20 ms, Δf = 100 Hz.

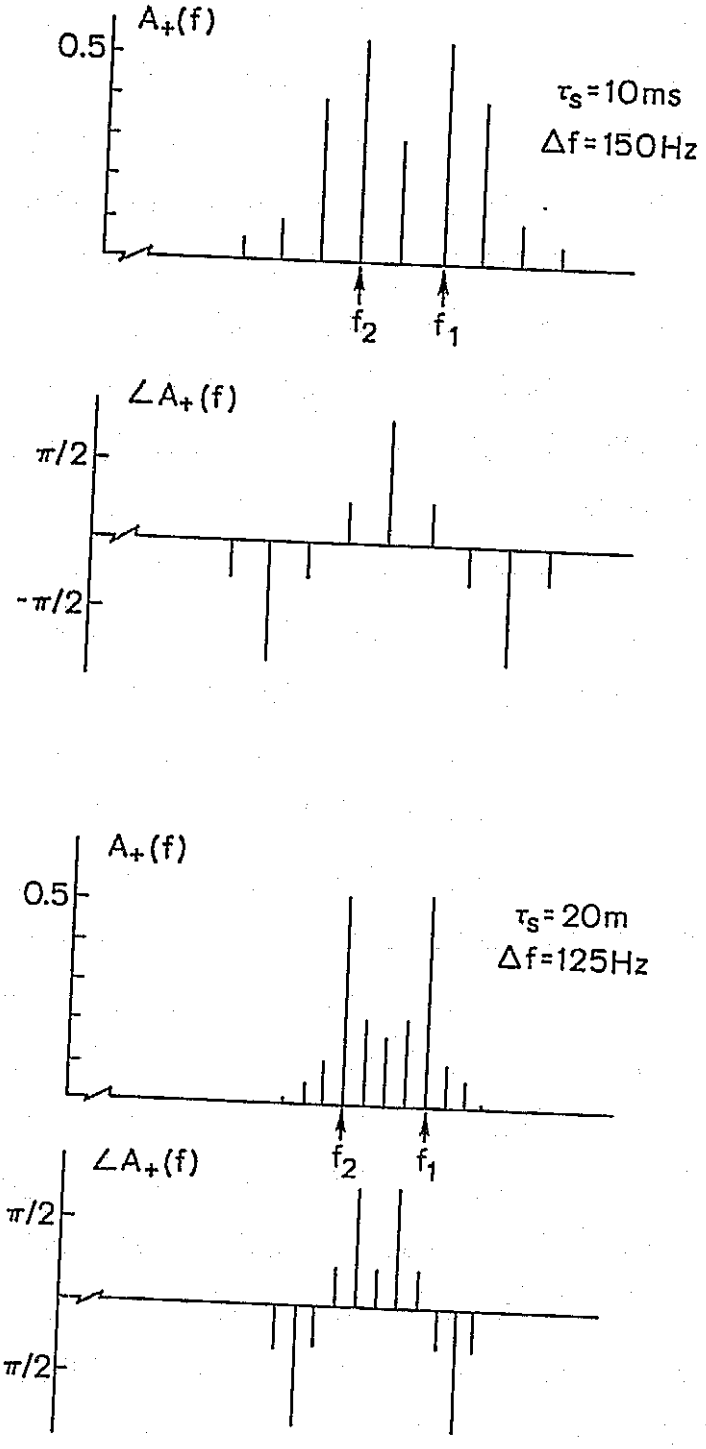

Fig. C.5. PLOTS OF $A_+(f)$ OF EQ. (C.5c) FOR TWO π-WAVE CASES: τ_s = 10 ms, Δf = 150 Hz AND τ_s = 20 ms, Δf = 125 Hz.

It is noticed that there are no spikes at f_1 and f_2, the carrier frequencies, when the signals are π-waves. This is understandable. The odd multiples of π-radian phase shifts between successive pulses in a carrier have cancelled the signal intensity completely in the carrier frequencies. It is a kind of carrier suppression transmission. Therefore, there is no energy at the carrier frequencies.

$A_{o,\pi}(f)$ consists of discrete spikes in frequency. From Eq. (C.3b), we have

$$W_{o,\pi}(t) = \sum_J P_J \sin (2\pi f_J t + \phi_J) \qquad (C.6)$$

Each spike corresponds to a sinusoidal wave in time domain. The FSK wave $W'_{o,\pi}(t)$ can be represented as

$$W'_{o,\pi}(t) = \prod\left(t - \frac{1}{2}\right) \sum_J P_J \sin (2\pi f_J t + \phi_J) \qquad (C.7)$$

It consists of several sinusoidal waves at various frequencies. Each of the sinusoidal waves last for one second, exactly the same duration as the FSKed wave. These sinusoidal waves, or spikes in the spectrum, shall be called sidebands.

Appendix D

MISCELLANEOUS EXAMPLES

The purpose of this section is to show a collection of interesting VLF wave phenomena related to "coherence bandwidth." We shall present some of the experimental results from two of the VLF wave injection experiments.

1. COBA Program

There are two kinds of signals in the coherence bandwidth (COBA) program. The first kind involves stepping up or down in frequency in a one-s pulse at the τth msec. The frequency offset Δf ranges from -25 to 25 Hz. The first τ msec of the pulse organizes electrons in a range $\Delta V_{\parallel}$ centered on the corresponding resonance velocity. When the frequency offset Δf is greater than the coherence bandwidth, most of the electrons organized by the pre-offset section of pulse become "free." They may radiate a field in a natural mode. Thus, triggered emissions may be developed at the offset. On the other hand, when Δf is less than the coherence bandwidth, most of the electrons organized by the pre-offset section can interact with the post-offset section. We may only expect to see a small amplitude perturbation at the transition.

The second kind is the so-called "rake-spectrum" signal. A pulse at f_o is transmitted for 400 msec, followed by an FSK wave with τ_s = 10 ms alternating between $f_o \pm 75$ Hz for 1.1 sec. The rake-spectrum signal is illustrated schematically in Fig. D.1 for both the high time resolution and the high frequency resolution displays. The intensity of the sideband at f_o is about one-third that of the pulse. The phase

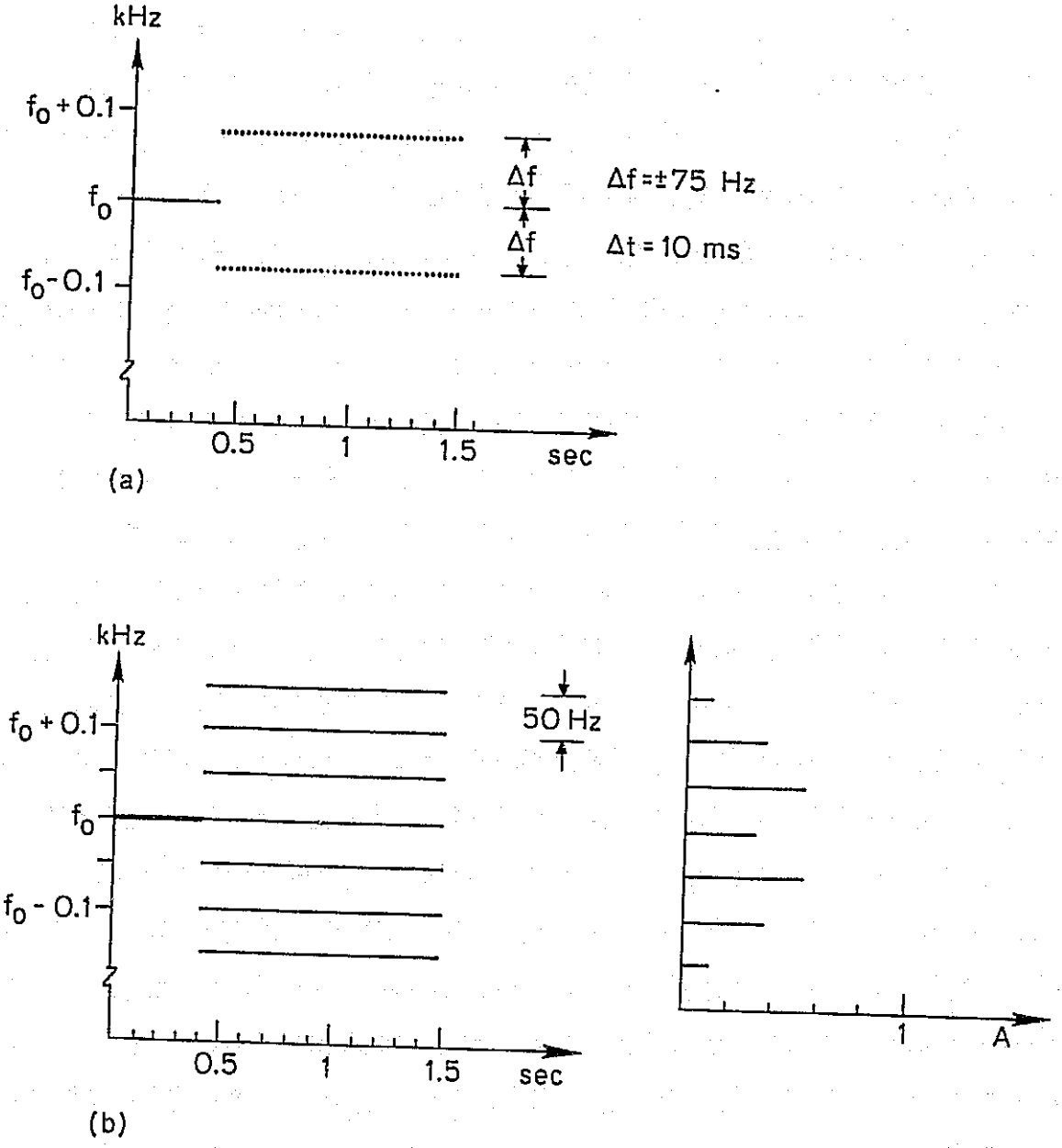

Fig. D.1. DISPLAY OF A "RAKE-SPECTRUM" WAVE AT A HIGH TIME RESOLUTION AND THAT AT A HIGH FREQUENCY RESOLUTION.

is not continuous at f_o during the transition. There is a difference of $3\pi/4$ radians between the phase of the key down pulse and that of the sideband at f_o. It is important to point out that the transition in the rake-spectrum is not smooth, because an electron can not resolve the sidebands in the interaction region until it encounters more than four 10 msec pulses. Thus, the key down pulse may trigger emissions that may then be entrained by the sidebands.

This program produces a variety of interesting phenomena, but it has not been possible to provide conclusive evidence regarding the size of the coherence bandwidth because of the lack of a large set of data samples. Two of the most interesting phenomena occur around the vernal equinox and will be discussed in this section.

Multiple triggering of rising emissions as shown in Fig. D.2 are among the typical features of wave activity during the equinox periods. The triggering signal is a one-s long pulse. It triggers a rising emission at about the 420th msec. The emission starts to develop around the 300th msec. We shall call this kind of emission "pre-termination emissions." The pulse triggers another rising emission at the end.

Figure D.3 shows four one-second waves in the COBA program. The frequency offset in each wave occurs at the 400th msec. The offset frequency Δf is +5, -5, +25, and -25 Hz, as indicated. The ramps indicate that there are two paths and that the one with the longer delay is the stronger. The ramps also serve as a barrier to prevent the emission triggered by one wave from contaminating the following wave. The times of offset are indicated by vertical bars on the top of the panel; the short bar for the first path and the long one for the second (a stronger) path. It is observed that the negative offset in frequency has inhibited

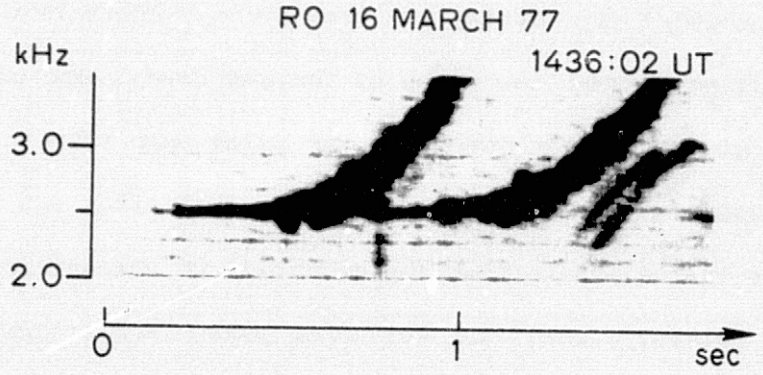

Fig. D.2. AN EXAMPLE OF MULTIPLE TRIGGERING; A TYPICAL FEATURE OF TRIGGERING AT EQUINOX.

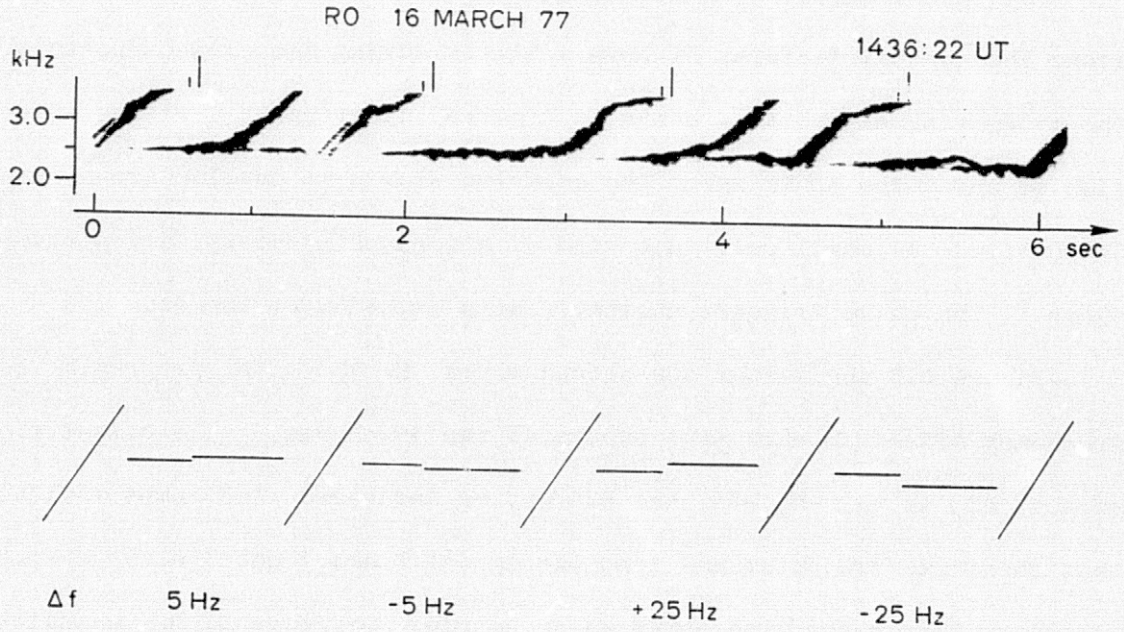

Fig. D.3. DEMONSTRATION OF A PART OF THE COBA PROGRAM TRANSMITTED AROUND EQUINOX. The pre-termination emissions are observable when the triggering waves have a positive frequency offset and disappear when the waves have a negative frequency offset.

or delayed the pre-termination emissions, while the positive offset in frequency does not affect the development of this emission. This indicates that a 25 Hz offset in frequency of a signal is not large enough to allow the two sections before and following the transition to become independent. Thus, 25 Hz is less than the coherence bandwidth of the signal in the pre-offset section in the interaction region.

The mechanisms that change the form of the pre-termination emissions due to negative offset in frequency have not been identified yet. However, it is believed that the timing of the offset is an important factor. In all the cases shown in Fig. D.3, the offset time is at the 400th msec, the time when the rising emission would have been developing, had there been no offset. A positive frequency offset appears to favor the development of a rising emission. A negative frequency offset seems to inhibit the development of rising emission.

Figure D.4 shows an example of "rake-spectrums." There were two paths, but the second path is the more pronounced. The 400-msec long pulse has been amplified. It may have triggered a BLI type of emission [Helliwell, 1978] that appears to feed energy to the 2.45, 2.55, and 2.5 kHz sidebands. The sideband amplitudes appear to decrease and finally reach the steady state levels. The total amplitude has dropped by about 10 dB from the peak value to the steady-state value, as indicated by the amplitude chart. The transient period is about 250 msec.

One more example is shown in Fig. D.5. There is only one observable path in this period. The emission triggered by the initial constant frequency pulse is entrained by the 2.55 kHz sideband and appears to fluctuate in between the two nearby sidebands at 2.5 and 2.6 kHz. The intensity of the emission forms a plateau for about 300 msec and is then quenched to a steady state level.

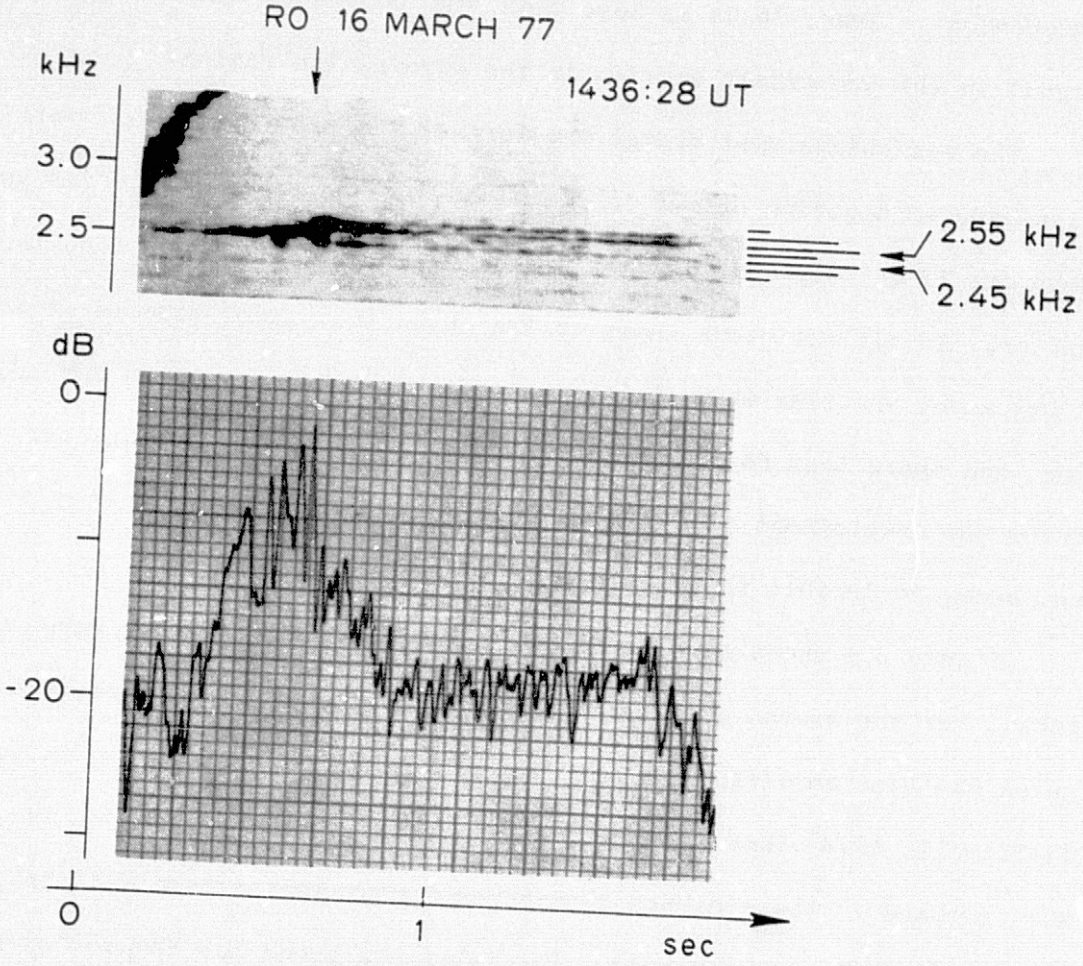

Fig. D.4. AN EXAMPLE OF A "RAKE-SPECTRUM" WAVE. The emission triggered by the 400 ms key down pulse appears to feed energy to the 2.45, 2.55, and 2.6 kHz sidebands. The total intensity decreases at a rate of ~30 dB/sec, and transient lasts for about 250 ms.

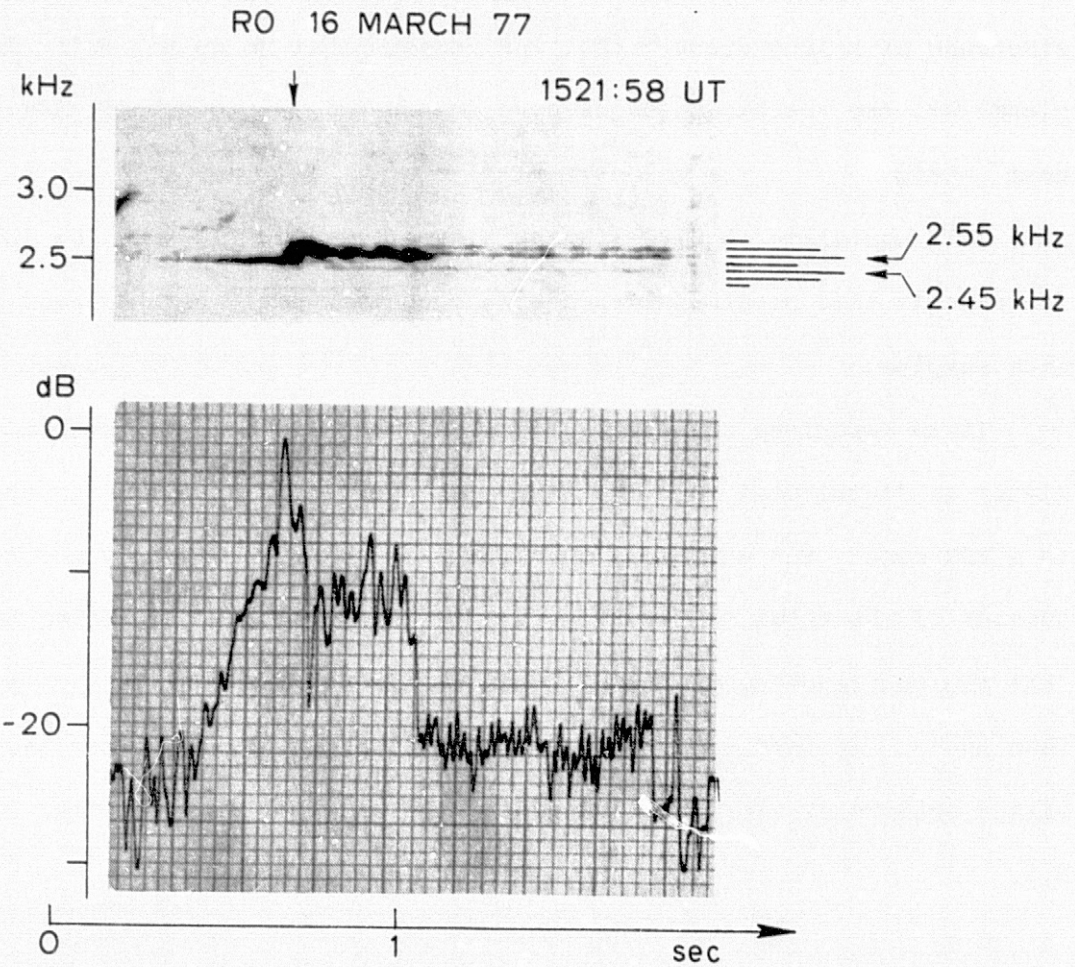

Fig. D.5. ANOTHER EXAMPLE OF A "RAKE-SPECTRUM" WAVE. The emission triggered by the 400 ms pulse is entrained by the 2.55 kHz sideband and wiggles in between two nearby sidebands at 2.5 and 2.6 kHz. The intensity is almost constant for 200 msec and then drops 10 dB to the "normal" steady state level.

It is postulated that this phenomenon is a suppression effect. The 50 Hz frequency spacing between the sidebands has imposed limitations on the steady state levels of the amplified sidebands. When the amplitude of a sideband is beyond its steady state level, it interacts with other sidebands at nearby frequencies. For reasons that we do not fully understand yet, the nearby sidebands have suppressed the sideband with "excess" energy.

This postulate requires further investigation. It will be useful to transmit this program again near the equinox periods to collect more data samples.

It is important to point out that the radiated energy from the transmitter is distributed into the sidebands when the transmitter is operated in a FSK mode. For example, the 2.55 kHz sideband has only about one-quarter of the total radiated energy. It shall not be surprising to find that the coherence bandwidth of a single frequency signal is much greater than 50 Hz. In fact, the coherence bandwidth of the pulse near the transition appears greater than 100 Hz for the examples in both Figs. D.4 and D.5.

2. CBT Program

The coherence bandwidth trap (CBT) program is a complicated and long program. One cycle of the program lasts for four minutes and sixteen seconds. Its purpose is to study the effect on wave growth of shifting the frequency regularly in the one-s triggering waves by a small amount. We intend to present only a small portion of this program. In that portion, a signal is shifted between two frequencies f_o and $f_o - \Delta f$ at regular intervals of 10 msec. The phase is continuous during the transitions.

The frequency shifts are 1, 5, 10, 20, 30, 50, 100, and 150 Hz for various signals. There is a one second "off" period between two successive signals in the frequency range (between f_o and $f_o - 150$ Hz).

Figure D.6 illustrates the amplitudes of these waves of which f_o is at 3 kHz. It is obtained by band-passing the signals through a filter at 3 kHz with a bandwidth of 170 Hz. The first two spikes correspond to the signals with $\Delta f = 0$ Hz, the second two to the signals with $\Delta f = 1$ Hz, the third two to the signals with $\Delta f = 5$ Hz, and so on. It is observed that, as Δf increases, the wave saturation levels drop. Figure D.7 shows the plot of the saturation levels vs Δf. Even a 1 Hz offset can cause a $\sim$4 dB reduction in the saturation levels. This reduction becomes greater than 10 dB as Δf increases beyond 50 Hz.

The electrons cannot resolve the sidebands of these signals with Δf less than 50 Hz in the interaction region because the modulation periods of these signals are greater than 100 ms. The electrons can only resolve segment-features of these signals. It can be shown that one hertz frequency difference can produce more than a π radian phase difference between two pure sine waves at $\sim$3 kHz traveling from the ground through a duct at $L = 4$ to the equator. Thus, the propagation path between the transmitter site and the interaction region can introduce large amplitude distortions at the junctions of successive pulses, creating regular amplitude depressions or enhancements before the signals arriving at the interaction region. The received signals show the effects of both the amplitude variation and frequency switching on the wave-particle interaction in the magnetosphere.

Contrary to the previous cases, electrons can resolve the sidebands of the signals with $\Delta f = 50$, 100, and 150 Hz because of the relatively

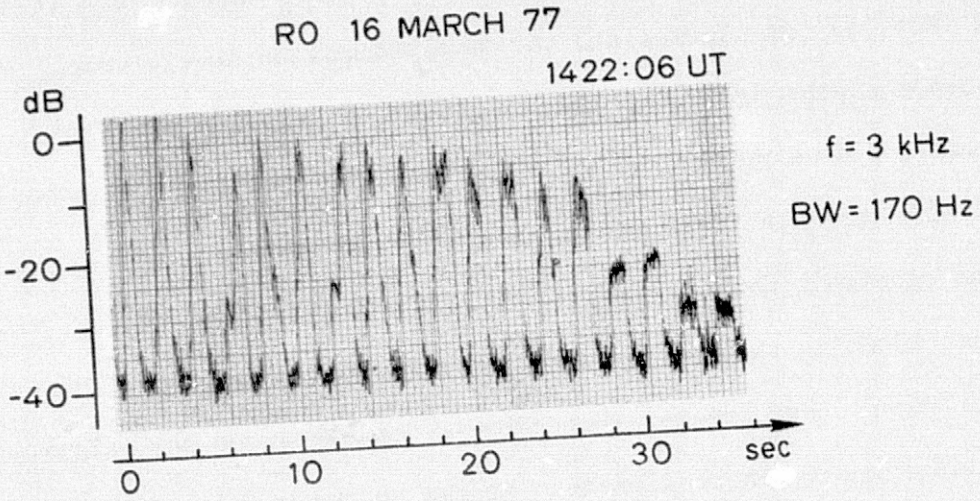

Fig. D.6. AN EXAMPLE OF THE VARIATIONS OF THE SATURATION AMPLITUDE OF FSK WAVES AS Δf INCREASES. It is part of a CBT program. The τ_s of FSK waves is 10 msec. The first two spikes correspond to the two waves with Δf = 0 Hz, the second two to those with Δf = 1 Hz, the third two to those with Δf = 5 Hz, then 10, 20, 30, 50, 100, and 150 Hz.

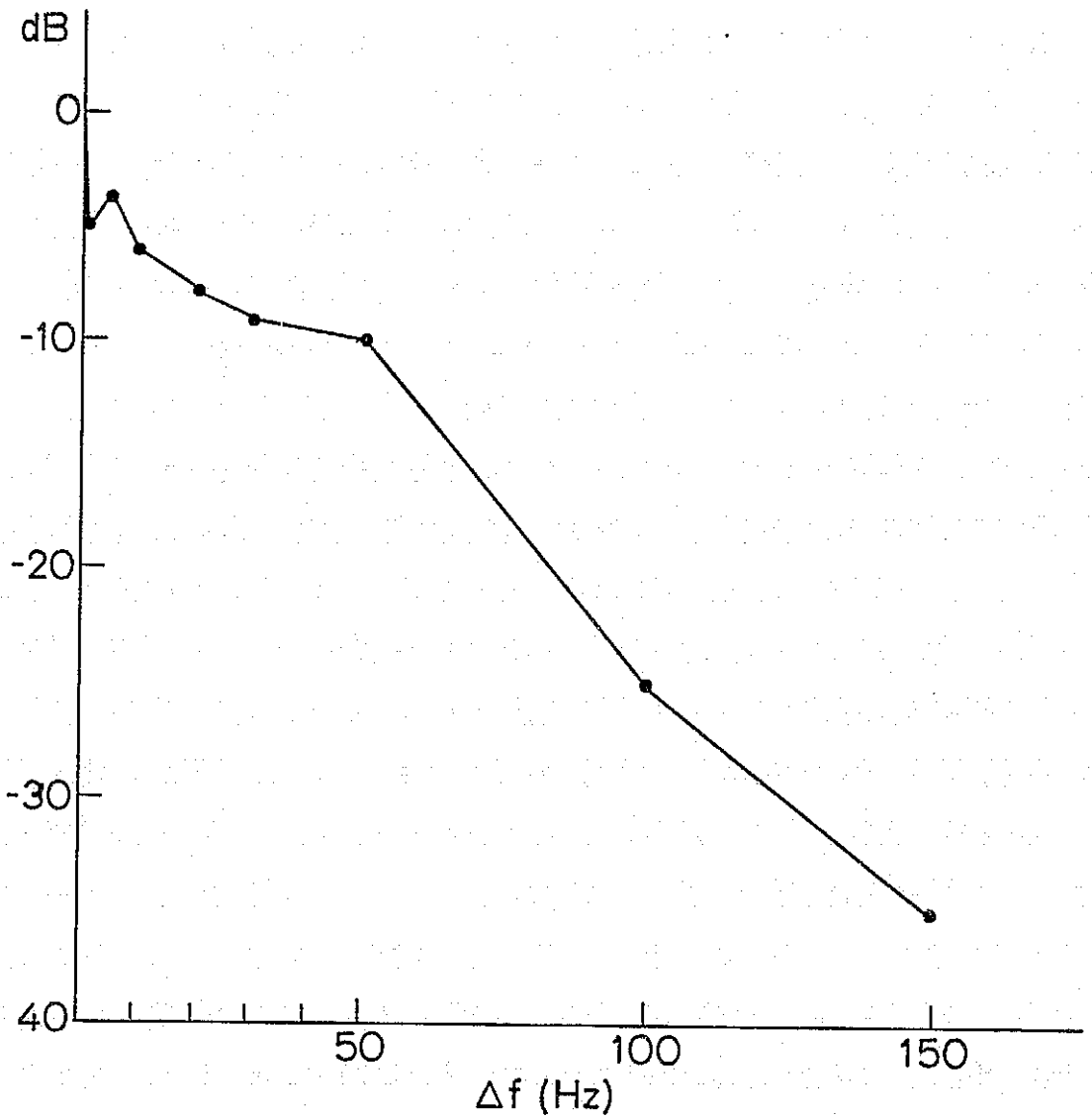

Fig. D.7. THE PLOT OF THE AMPLITUDE VS Δf OF THE FSK WAVES ILLUSTRATED IN FIG. D.6.

small modulation periods on the signals ($\leq$40 ms). The propagation path introduces phase differences among the sidebands. Sidebands are constant frequency signals with a duration of one second (see Appendix C). The absolute phase of a sideband is not important to its ability to interact with energetic electrons. Thus, the propagation distortion will have no effect on sideband growth.

The sidebands are spaced at multiples of 50 Hz and extend in frequency more than the bandwidth of the filter (170 Hz). It is therefore essential to see the signal strength over a larger bandwidth. Figure D.8 depicts the amplitudes of the signals over a 680 Hz bandwidth vs Δf. Comparing this with Fig. D.7, it is noticed that the most significant change comes at the point of Δf = 150 Hz. This is understandable because the 170 Hz band-pass filter leaves out a significant amount of sidebands for the FSK wave with Δf = 150 Hz.

Figure D.9 shows the averaged wave intensities over four sets of data samples obtained within an hour. The bandwidth of the band-pass filter is set to 680 Hz. It appears that the wave intensity drops as Δf increases for $\Delta f \leq$ 100 Hz.

For $\Delta f \geq$ 100 Hz, sidebands have been resolved by the electrons in the magnetosphere. Detailed studies reveal (not shown) that these sidebands are not amplified significantly and that there are no triggered emission.

The 2.975 kHz sideband of the signal with Δf = 50 Hz is about 1.4 times stronger than that of the signal with Δf = 150 Hz. The former can trigger emissions four out of five times, while the latter does not even show growth most of the time. This suggests that there is an amplitude threshold level above which waves can be amplified and trigger emissions.

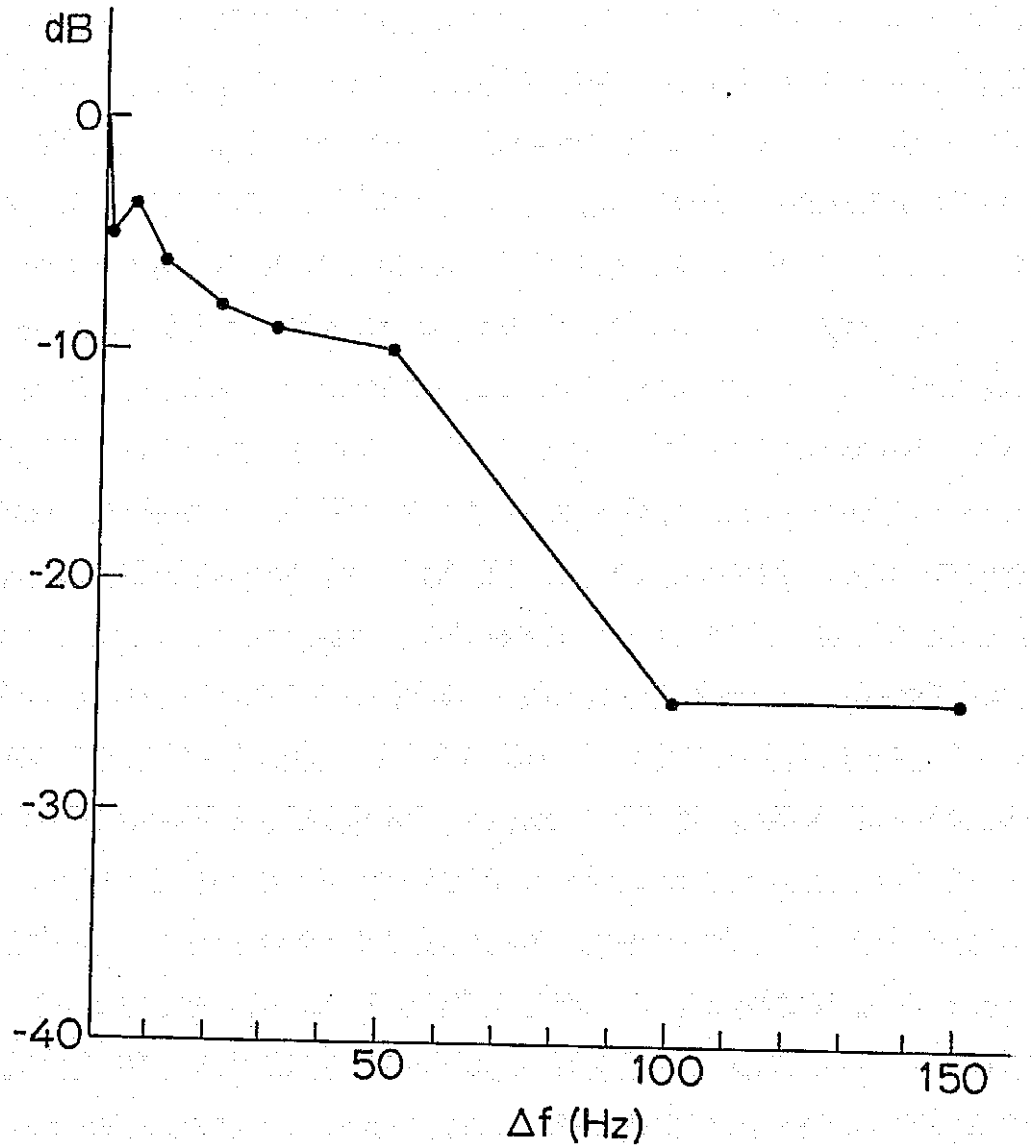

Fig. D.8. THE PLOT OF THE AMPLITUDE VS Δf OF THE SAME DATA AS THAT IN FIG. D.7 BUT FROM A FILTER WITH A WIDER BANDWIDTH, 680 Hz.

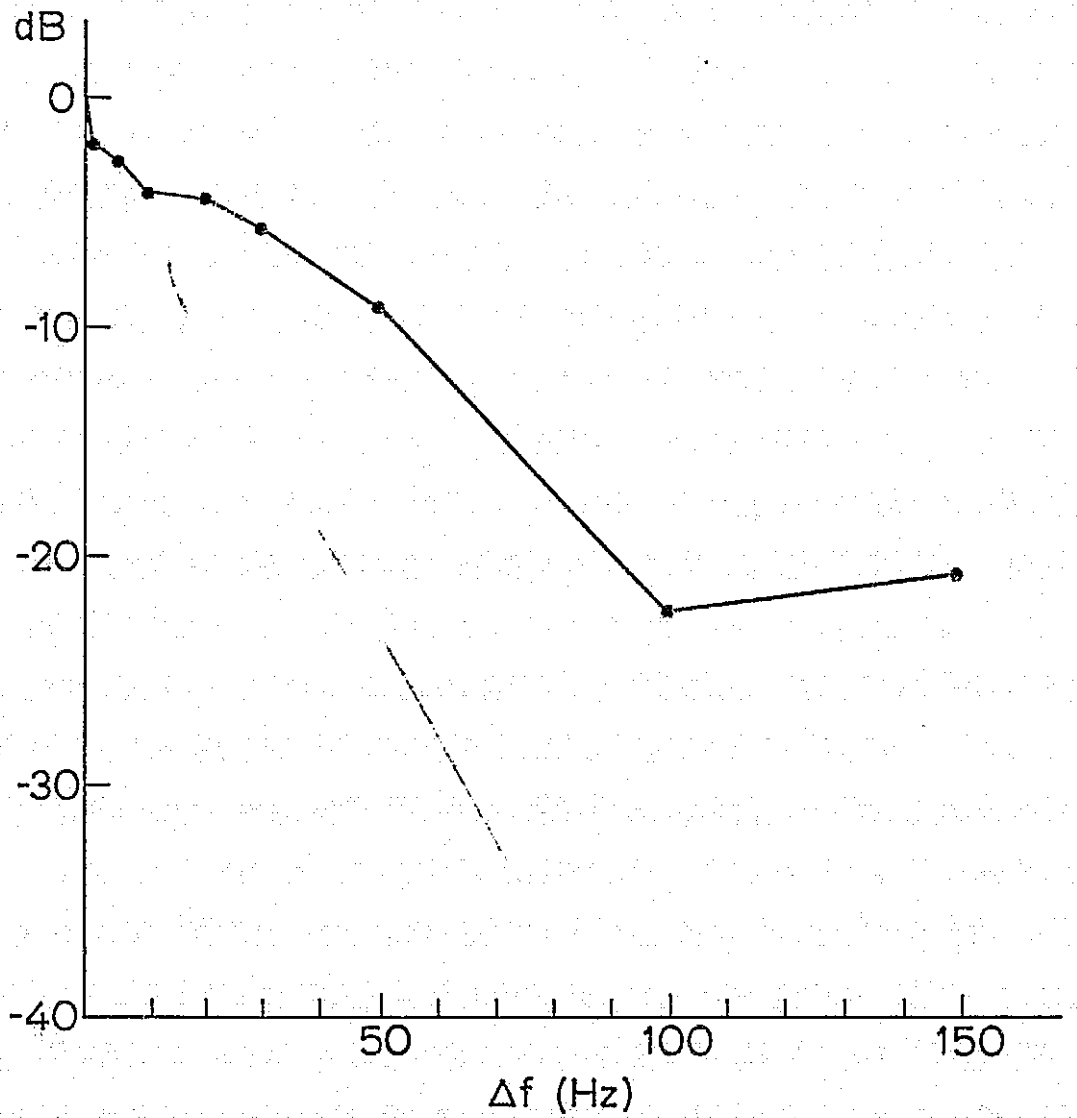

Fig. D.9. THE PLOT OF AVERAGED AMPLITUDE VS Δf OF THE FSK WAVES OVER FOUR SETS OF DATA SAMPLES TAKEN WITHIN AN HOUR.

When $\Delta f < 50$ Hz, there are effects in the data due to frequency offsets as well as amplitude variation introduced by propagation distortion. Frequency offset effects are small when Δf is 1 Hz. Thus, a drop of a few dB caused by a 1 Hz offset most likely is due to the amplitude variations in the triggering signals introduced by the propagation distortions.

Changing the frequency of a wave corresponds to altering the ψ of the electrons interacting with the waves (see Appendix B). Thus, some of the electrons trapped by a pulse at f_o may become untrapped by the following one at $f_o \pm \Delta f$. But there are electrons which can effectively interact with signals at both frequencies. As Δf increases, the number of these electrons which interact with signals at both frequencies is reduced. The ability of the wave to organize electrons is reduced and, hence, the growth is less. This effect should be small when the frequency change is small and shall become pronounced if the frequency shift increases.

A way to eliminate the propagation distortion has been discussed in the previous chapters. In order to study the effects on wave growth due to a small shift in frequency, it is necessary to reduce the propagation distortion by implementing a pre- and a post-processor on the transmitting and receiving sites, respectively.

BIBLIOGRAPHY

Akasofu, S. I. and S. Chapman, Solar Terrestrial Physics, Oxford at the Clarendon Press, 1972.

Angerami, J. J., "A Whistler Study of the Distribution of Thermal Electrons in the Magnetosphere," Technical Report No. SEL-66-017, Radioscience Lab., Stanford Electronics Labs., Stanford University, Stanford, Calif., May 1966.

Bell, T. F. and O. Buneman, "Plasma Instability in the Whistler Mode Caused by a Gyrating Electron Stream," The Phys. Rev., 133, A1300, 1964.

Bell, T. F., "Nonlinear Alfven Waves in a Vlasov Plasma," The Phys. of Fluids, 8, 1829, 1965.

Bell, T. F., "ULF Wave Generation through Particle Precipitation Induced by VLF Transmitters," J. Geophys. Res., 81, 3316, 1976.

Blackman, G. O. and J. W. Tukey, The Measurement of Power Spectra, Dover, New York, 1958.

Bracewell, R. N., The Fourier Transform and Its Applications, McGraw-Hill, Inc., New York, 1965.

Brice, N., "Fundamental of VLF Emission Generation Mechanism," J. Geophys. Res., 69, 4515, 1964.

Brillouin, L., Wave Propagation and Group Velocity, Academic Press, New York, 1960.

Brinca, A. L., "On the Stability of Obliquely Propagating Whistlers," J. Geophys. Res., 77, 3495, 1972.

Buckley, R., "The Propagation of a Pulse in a Dispersive Plasma: An Exact Solution Compared with Various Approximations," J. Plasma Phys., 13, Part 3, 1975.

Budden, K. G., Radio Waves in the Ionosphere, Cambridge University Press, 1966.

Burtis, W. J., "Magnetospheric Chorus," Technical Report No. SEL-74-041, Radioscience Lab., Stanford Electronics Labs., Stanford University, Stanford, Calif., August 1974.

Carpenter, D. L., "Electron-Density Variations in the Magnetosphere Deduced from Whistler Data," J. Geophys. Res., 67, 3345, 1962.

Carpenter, D. L., "Whistler Evidence of a 'Knee' in the Magnetospheric Ionization Density Profile," J. Geophys. Res., 68, 1675, 1963.

Carpenter, D. L., "Whistler Studies of the Plasmapause in the Magnetosphere-1; Temporal Variations in the Position of the Knee and Some Evidence on Plasma Motions Near the Knee," J. Geophys. Res., 71, 693, 1966.

Chang, D. C. D. and R. A. Helliwell, "Controlled Nonlinear Wave-Wave Interaction in the Magnetosphere," paper presented at URSI Meeting, Stanford, Calif., August 1977.

Chang, D. C. D. and C. G. Park, "Simulation of Power-Line Radiation Effects in the Magnetosphere Using VLF Transmitter at Siple, Antarctica," paper presented at AGU Meeting, December 1977.

Chapman, R. D., Solar Terrestrial Programs, A Five-Year Plan, Office of Space Science, NASA, January 1977.

Crystal, T. L., "Nonlinear Currents Stimulated by Monochromatic Whistler-Mode (WM) Waves in the Magnetosphere," Technical Report No. SEL-75-015, Radioscience Lab., Stanford Electronics Labs., Stanford University, Stanford, Calif., May 1975.

Crystal, T. L., "Simplified Computer Simulation of Magnetospheric VLF Triggered Emissions," paper presented at URSI Meeting, Stanford, Calif., June 1977.

Dingle, B., "Burst Precipitation of Energetic Electrons from the Magnetosphere," Technical Report No. 3477-1, Radioscience Lab., Stanford Electronics Labs., Stanford University, Stanford, Calif., 1978.

Dysthe, K. B., "Some Studies of Triggered Whistler Emissions," J. Geophys. Res., 76, 6915, 1971.

Gendrin, R., "Phase-Bunching and Other Nonlinear Processes Occurring in Gyroresonant Wave-Particle Interaction," Astrophys. and Space Sci., 28, 244, 1974.

Haskell, R. E. and C. T. Case, "Transient Signal Propagation in Lossless, Isotropic Plasmas," IEEE Trans. Antennas and Propagation, AP-15, 458, May 1967.

Helliwell, R. A., Whistlers and Related Ionospheric Phenomena, Stanford University Press, Stanford, Calif., 1965.

Helliwell, R. A., "A Theory of Discrete VLF Emissions from the Magnetosphere," J. Geophys. Res., 72, 4773, 1967.

Helliwell, R. A., "VLF Wave-Wave Interactions in the Magnetosphere (in preparation), 1978.

Helliwell, R. A. and T. L. Crystal, "A Feedback Model of Cyclotron Interaction between Whistler-Mode Waves and Energetic Electrons in the Magnetosphere," J. Geophys. Res., 78, 7357, 1973.

Helliwell, R. A. and J. P. Katsufrakis, "VLF Wave Injection into the Magnetosphere from Siple Station, Antarctica," J. Geophys. Res., 79, 2511, 1974.

Helliwell, R. A., J. P. Katsufrakis, and M. L. Trimpi, "Whistler-Induced Amplitude Perturbations in VLF Propagation," J. Geophys. Res., 78, 4679, 1973.

Helliwell, R. A., J. P. Katsufrakis, T. F. Bell, and R. Roghuram, "VLF Line Radiation in the Earth's Magnetosphere and Its Association with Power Line Radiation," J. Geophys. Res., 80, 4247, 1975.

Hess, W. N., The Radiation Belt and Magnetosphere, Blaisdell Publishing Co., Mass., 1968.

Heyborne, R. L., "Observations of Whistler Mode Signals in the OGD Satellites from VLF Ground Station Transmitters," Technical Report No. SEL-66-094, Radioscience Lab., Stanford Electronics Labs., Stanford University, Stanford, Calif., 1966.

Ho, D., "Interaction between Whistlers and Quasi-Periodic VLF Emissions," J. Geophys. Res., 78, 7347, 1973.

Ho, D., "Quasi-Periodic (QP) VLF Emissions in the Magnetosphere," Technical Report No. SEL-74-054, Radioscience Lab., Stanford Electronics Labs., Stanford University, Stanford, Calif., December 1974.

Inan, U. S., "Nonlinear Gyroresonant Interactions of Energetic Particles and Coherent VLF Waves in the Magnetosphere," Technical Report No. SEL-77-026, Radioscience Lab., Stanford Electronics Labs., Stanford University, Stanford, Calif., August 1977.

Inan, U. S., T. F. Bell, D. L. Carpenter, and R. R. Anderson, "Explorer 45 and Imp-6 Observations in the Magnetosphere of Injected Waves from the Siple Station VLF Transmitter," J. Geophys. Res., 82, 1177, 1977.

Kennel, C. F. and H. E. Petschek, "Limit on Stably Trapped Particle Fluxes," J. Geophys. Res., 71, 1, 1966.

Koons, H. C., M. H. Dazey, R. L. Dowden, and L. E. S. Amon, "A Controlled VLF Phase-Reversal Experiment in the Magnetosphere," Technical Report No. SAMSO-TR-76-218, The Aerospace Corporation, El Segundo, Calif., November 1976.

Kozaki, S. and Y. Mushiake, "Propagation of Electromagnetic Pulse Having a Gaussian Envelope in Longitudinally Inhomogeneous Anisotropic Ionized Media," IEEE Trans. Antenna and Propagation, AP-18, 259, March 1970.

Liemohn, H. B., "Cyclotron-Resonance Amplification of VLF and ULF Whistlers," J. Geophys. Res., 72, 39, 1967.

Liemohn, H. B. and B. H. Duane, "Particle Motion in Ion Cyclotron Wave Fields," Amer. J. of Phys., 44, No. 1, January 1976.

Matsumoto, H., "Theoretical Studies on Whistler Mode Wave Particle Interactions in the Magnetospheric Plasma," Kyoto University, Kyoto, Japan, 1972.

McIlwain, C. E., "Coordinates for Mapping the Distribution of Magnetically Trapped Particles," J. Geophys. Res., 66, 3681, 1961.

Mcpherson, D. A., H. C. Koons, M. H. Dazey, R. L. Dowden, L. E. S. Amon, and N. R. Thomson, "Conjugate Magnetospheric Transmissions at VLF from Alaska to New Zealand," J. Geophys. Res., 79, 1555, 1974.

Newman, C. E., Jr., "Theoretical Study of Amplitude Pulsations of 'Key-Down' Whistler Mode Signals in the Geomagnetosphere," J. Geophys. Res., 82, No. 1, 105, 1977.

Nunn, D., "A Theory of VLF Emissions," Planet. Space Sci., 19, 1141, 1971.

Nunn, D., "A Self-Consistent Theory of Triggered VLF Emissions," Planet. Space Sci., 22, 349, 1974.

Palmadesso, G. and G. Schmidt, "Collisionless Damping of a Large Amplitude Whistler Wave," Phys. Fluids, 14, 1411, 1971.

Park, C. G., "Whistler Observation of Interchange of Ionization between the Ionosphere and Protonosphere," J. Geophys. Res., 75, 4249, 1970.

Park, C. G., "Methods of Determining Electron Concentrations in the Magnetosphere from Nose Whistlers," Technical Report No. SEL-71-058, Radioscience Lab., Stanford Electronics Labs., Stanford University, Stanford, Calif., 1971.

Ratcliff, J. A., An Introduction to the Ionosphere and Magnetosphere, Cambridge University Press, 1972.

Raghuram, R., "Suppression Effects Associated with VLF Transmitter Signals Injected into the Magnetosphere," Technical Report No. SEL-77-007, Radioscience Lab., Stanford Electronics Labs., Stanford University, Stanford, Calif., March 1977.

Raghuram, R., T. F. Bell, R. A. Helliwell, and J. P. Katsufrakis, "Echo-Induced Suppression of Coherent VLF Transmitter Signals in the Magnetosphere," J. Geophys. Res., 82, 2787, 1977.

Raghuram, R., T. F. Bell, R. A. Helliwell, and J. P. Katsufrakis, "A Quiet Band Produced by VLF Transmitter Signals in the Magnetosphere," Geophys. Res. Letts., 4(5), 199, 1977.

Robert, C. S., "Pitch-Angle Diffusion of Electrons in the Magnetosphere," Rev. of Geophys., 7, 305, 1969.

Roederer, J. G., Dynamics of Geomagnetically Trapped Radiation, Springer-Verlag, Berlin, Heidelberg, 1970.

Rönnäng, B. O., "Distortion of an Electromagnetic Pulse Carrier Propagating in an Anisotropic Homogeneous Plasma," IEEE Trans. Antennas and Propagation, AP-16, 146, January 1968.

Rosenburg, T. J., R. A. Helliwell, and J. P. Katsufrakis, "Electron Precipitation Associated with Discrete VLF Emissions," J. Geophys. Res., 76, 8445, 1971.

Seyler, C. E., Jr., S. C. Bloch, and R. W. Flynn, "Pulse Propagation in a Magnetoplasma. 1. Longitudinal Propagation," J. Geophys. Res., 77, 4237, August 1972.

Smith, R. L., "Propagation Characteristics of Whistlers Trapped in Field-Aligned Columns of Enhanced Ionization," J. Geophys. Res., 66, 3699, 1961.

Smith, R. L. and D. L. Carpenter, "Extension of Nose Whistler Analysis," J. Geophys. Res., 66(8), 2582, August 1961.

Stiles, G. S., "Digital Spectra of Artificially Stimulated VLF Emissions," Technical Report No. SEL-74-049, Radioscience Lab., Stanford Electronics Labs., Stanford University, Stanford, Calif., December 1974.

Stiles, G. S. and R. A. Helliwell, "Frequency Time Behavior of Artificially Stimulated VLF Emissions," J. Geophys. Res., 80, 608, 1975.

Stiles, G. S. and R. A. Helliwell, "Stimulated Growth of Coherent VLF Waves in the Magnetosphere," J. Geophys. Res., 82, 523, February 1977.

Suden, R. N. and E. Ott, "Theory of Triggered VLF Emissions," J. Geophys. Res., 76, 4463, 1971.

Tverskoy, B. A., "Main Mechanisms in the Formation of Earth's Radiation Belts," Rev. of Geophys., 7, 219, 1969.

Vidmar, R. J. and F. W. Crawford, "Delta-Function Excitation of Whistlers in a Cold Magnetoplasma," paper presented at Proc. XIIth International Conf. on Phenomena in Ionized Gases, Eindhoven, The Netherlands, August 1975.